Charles University in Prague

Faculty of Mathematics and Physics

DOCTORAL THESIS

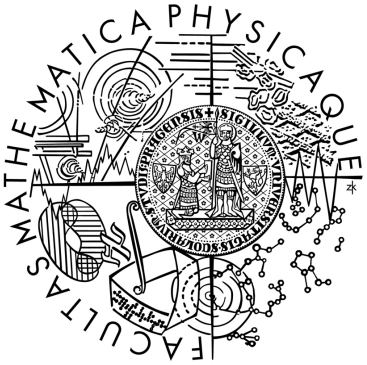

Daria Drozdenko

Study of novel magnesium alloys with controlled microstructure and texture

Department of Physics of Materials

Supervisor of the doctoral thesis: Ing. Patrik Dobroň, Ph.D.

Study programme: Physics
Specialization: Physics of Condensed Matter and Materials Research

Prague 2016

I declare that I carried out this doctoral thesis independently, and only with the cited sources, literature and other professional sources.

I understand that my work relates to the rights and obligations under the Act No. 121/2000 Coll., the Copyright Act, as amended, in particular the fact that the Charles University in Prague has the right to conclude a license agreement on the use of this work as a school work pursuant to Section 60 paragraph 1 of the Copyright Act.

In Prague, 21. 07. 2016

Acknowledgments

First of all, I wish to thank my supervisor Dr. Patrik Dobroň for inspiring and active guidance during my study, without which completing this thesis would not have been possible.

My sincere thanks go to Doc. František Chmelík for advising and explanation for me interesting world of acoustic emission in materials. I also thank Prof. Pavel Lukač for fruitful discussions about physics of deformation processes in metals. I also thank Doc. Ladislav Havela for tremendous support, advices and interesting discussions about different topics in physics.

The work presented in this thesis has been done in a fruitful collaboration with the Magnesium Innovation Centre (MagIC). I wish to thank Dr. Jan Bohlen, Dr. Sangbong Yi, Dr. Dietmar Letzig for kind hospitality and interesting discussions during my visits the Helmholtz-Zentrum Geesthacht. There is no magic without you.

I am grateful to all my colleagues and laboratory assistance at the Department of Physics of Materials, Charles University in Prague, for interesting conversations and good atmosphere during work time and not only. Thank you all for opportunity to become a part of a great team.

The last but not the least, I am heartily thankful to my family and persons close to my heart for their never-ending support and encouragement, I love you to the moon and back.

Title: Study of novel magnesium alloys with controlled microstructure and texture
Author: Daria Drozdenko

Department / Institute: Department of Physics of Materials, Faculty of Mathematics and Physics, Charles University in Prague

Supervisor of the doctoral thesis: Ing. Patrik Dobroň, Ph.D., Department of Physics of Materials.

Abstract:

The work elucidates the role of dislocation slip and twinning during plastic deformation in selected magnesium (Mg) alloys with controlled microstructure and texture. The acoustic emission (AE) technique was concurrently applied during deformation to determine the activity of particular deformation mechanisms. A detailed insight into microstructure was provided by electron microscopy.

In order to obtain a comprehensive set of AE data for particular deformation mechanisms, Mg single crystals with various crystallographic orientations were channel-die and uniaxially compressed. The obtained results were applied on deformation mechanisms in polycrystalline textured Mg alloys. Particularly, the twinning - detwinning processes, in the sense of twin boundary mobility, during one cycle loading (pre-compression followed by tension) were described. Clear correlations between changes in the AE response and the inflection points on the deformation curve were found. An analysis of twin activity with respect to different types of microstructure (bimodal or homogeneous) showed a grain size effect on twin nucleation. The influence of texture on the deformation behavior was also identified for conventionally rolled slabs and rolled twin-roll cast Mg alloy strips in the form of sheets. An anisotropy of mechanical properties may be easily associated with the texture asymmetry around the normal direction, which is formed during the particular rolling process.

Keywords: wrought Mg alloys, texture, deformation mechanisms, acoustic emission, mechanical properties.

Téma: Studium nových slitin na bázi Mg s řízenou mikrostrukturou a texturou
Autor: Daria Drozdenko

Školící pracoviště: Katedra fyziky materiálů, Univerzita Karlova v Praze, Matematicko-fyzikální fakulta

Školitel: Ing. Patrik Dobroň, Ph.D., Katedra fyziky materiálů MFF UK.

Abstrakt:

Práce objasňuje role skluzu dislokací a dvojčatění v průběhu plastické deformace vybraných hořčíkových (Mg) slitin s řízenou mikrostrukturou a texturou. Metoda akustické emise (AE) byla použita pro určení jednotlivých deformačních mechanismů. Elektronová mikroskopie poskytla informaci ohledně vývoje mikrostruktury studovaných materiálů.

Pro získání referenčních dat AE pro jednotlivé deformační mechanismy, monokrystaly hořčíku byly deformovány v různých krystalografických orientacích. Získané výsledky byly použity pro studium deformačních mechanismů polykrystalických texturovaných Mg slitin. Proces růstu a redukce dvojčat (z pohledu pohybu hranic dvojčat) byl podrobně zkoumán během jednoho cyklu namáhání (tlak následován tahem). Byly odhaleny výrazné korelace mezi změnami v odezvě AE a inflexními body deformační křivky. Analýza aktivity dvojčatění v materiálech s různou mikrostrukturou (bimodální nebo homogenní) ukázala výrazný vliv velikosti zrn na nukleaci dvojčat. Vliv textury na deformační chování byl určen pro plechy válcované různým způsobem. Anizotropie mechanických vlastností je určena asymetrií textury, která je výsledkem procesu válcování.

Klíčová slova: hořčíkové slitiny, textura, deformační mechanismy, akustická emise, mechanické vlastnosti.

"Everything should be made as simple as possible, but not simpler"

Albert Einstein

Contents

List of symbols and abbreviations

a – lattice parameter in a hexagonal close packed structure

A/D converter – analog to digital converter

AE – acoustic emission

A_{max} – maximum amplitude of the AE event

b – Burger's vector

bcc – body centered cubic structure

c – lattice parameter in a hexagonal close packed structure

CRSS (τ_{CRSS}) – critical resolved shear stress

CYS – compressive yield strength

d – average grain diameter

$\Delta N_C/\Delta t$ – Count rate – number of counts per time unit

EBSD – electron backscattered diffraction

ED – extrusion direction

fcc – face centered cubic structure

F – applied force or load

hcp – hexagonal close packed structure

HDT – hit definition time

HLT – hit lockout time

IQ map – image quality map

k – strengthening coefficient of grain boundaries

KAM map – kernel average misorientation map

LM – light microscopy

m – Schmid factor

N_C – number of counts per unit time

ND – normal direction

$\vec{o}$ – slip plane

PDT – peak definition time

RD – rolling direction

RE elements – rare earth elements

RT – room temperature

S_0 – initial diameter of a single crystalline cylinder

SEM – scanning electron microscopy

STEM – scanning transmission electron microscopy

t – time

TB – twin boundary

TD – transversal direction

TEM – transmission electron microscopy

TYS – tensile yield strength

TRC – twin roll casting

UTS – ultimate tensile strength

VPSC – visco-plastic self-consistent scheme

YS – yield strength

ε – strain rate

η_1, η_2 – direction of twinning or slip

κ – angle between direction of slip and axis of slip plane

κ_1, κ_2 – plane of twinning or slip

λ_A – angle between load axis and the glide direction

σ – applied stress to the material

σ_0 – materials constant for the starting stress for dislocation movement

σ_{YS} – yield stress

φ – angle between load axis and normal to slip plane

χ – angle between loading axis and slip plane

Chapter 1

Preface

The increased demand for high performance and environmentally friendly materials requires a permanent development of materials and processing technologies. A scientific research is an integral part of designing of novel materials. Magnesium and its alloys have been intensively studied during last two decades and they are still in the focus of interest due to their low density and high damping capacity. Wrought Mg alloys can fulfil requirements of many applications in the automotive and aerospace industry. However, their use is often limited due to inherent anisotropy of mechanical properties caused by a hexagonal close-packed (hcp) lattice, texture and homogeneity of produced materials. Specific crystallographic textures are developed during formation processes, as for example extrusion, rolling, and forging. A distinct in-plane anisotropy in rolled materials and tension-compression asymmetry at the yield strength in extruded materials are linked with the formation of twins. Twinning is therefore a key mechanism of plastic deformation in Mg alloys. Moreover, the twinning – detwinning mechanism is a characteristic process during cyclic loading of wrought Mg alloys.

At the present level of understanding, it is essential to get more insight into individual mechanisms of deformation (dislocation slip, twinning, twinning - detwinning) with respect to given texture and homogeneity of the material.

A wide range of advanced experimental techniques will be applied to extend our knowledge about deformation mechanisms in wrought Mg alloys. The deformation mechanisms will be investigated using *in-situ* and *post-mortem*

methods in order to get information about the relation of the deformation behavior and microstructure. The obtained results could be implemented to physical models describing deformation behavior of materials.

The acoustic emission (AE) technique belongs to *in-situ* methods and based on a detection of transient elastic waves produced by a sudden release of energy due to a local dynamic change within a material. The AE technique offers integral information from the entire volume of the material about dynamic processes during loading of the material. Therefore, it can be used for a study of dislocation motion and twinning in wrought Mg alloys.

The AE features can be related to individual deformation mechanisms which occur during mechanical loading. In this regard, plane strain compression and uniaxial compression tests will be performed to provide information on dislocation slip and twinning, all as a function of sample orientation. Obtained results will be used for the interpretation of the AE response during deformation of wrought Mg alloys with respect to their texture and microstructure. Particularly, the twinning-detwinning mechanism in extruded Mg alloys will be studied in detail.

In the frame of a cooperation with one of the top rated institutes in research and development of Mg alloys, MagIC, Helmholtz-Zentrum Geesthacht, the achieved knowledge of the present research significantly contributes to a development and production of novel Mg alloys with a high potential for technical applications.

The thesis is organized as follows:

- The current understanding of deformation mechanisms in Mg and its alloys is presented in Chapter 2. The basic information about Mg, possible deformation mechanisms and a review of the influence of texture on mechanical properties of polycrystalline Mg alloys is given. Moreover, a brief introduction to the AE technique containing a basic characterization of the AE signal and the AE terminology can be found.
- Aims of the thesis are given in Chapter 3
- Chapter 4 covers the experimental procedure and methods used in the work: deformation tests, AE technique, X-ray diffraction, light and scanning electron microscopy.

- Obtained results and discussions are presented in Chapter 5. Paragraph 5.1 is focused on revealing AE signatures for specific deformation mechanisms activated in Mg. Based on these results, investigation of deformation mechanisms in Mg alloys with strong texture is addressed in paragraph 5.2 and 5.3. Particularly, paragraph 5.2 gives explanation of twinning-detwinning process in extruded Mg alloys with a respect to their microstructure. Paragraph 5.3 provides explanation of the influence of rolling process, represented by the initial texture, on the deformation behavior of the sheets.
- General conclusions and perspectives for further work are summarized in Chapter 6.

Chapter 2

Theoretical background

2.1. Deformation systems of magnesium: dislocation slip and twinning

The basic plasticity mechanisms in metallic materials are slip and twinning. ***Slip*** is a displacement of one part of a crystal relative to the other part. On atomic scale, the slip involves sliding of one plane of atoms over another. The plane on which the slip occurs is called ***slip plane*** and the direction in which this occurs is called ***slip direction***. Slip occurs when applied shear stress exceeds a critical value for its activation, critical resolved shear stress (CRSS). During the slip each atom usually moves the same integral number of atomic distances along the slip plane producing a step, while the orientation of the crystal remains the same. Slip occurs on close-packed planes (those containing the greatest number of atoms per area), and in close-packed directions (most atoms per length). Slip could be also interpreted as motion of dislocations from one place to another. There are two basic types of dislocations movements called as glide and climb. In ***glide***, the dislocation moves in a plane defined by its line and Burger's vector: glide is the conservative motion of dislocations. In ***climb***, the dislocation moves out of the glide surface and therefore, climb becomes a non-conservative motion of dislocation.

In materials with hexagonal lattice, plastic deformation depends on ***the ratio of lattice parameters c/a***. In case of crystal structure consisting of close-packed planes, the c/a ratio is $\sqrt{8/3}$, so-called ideal value. When the c/a ratio is higher than the ideal value (Zn, Cd), higher atomic density is in the basal plane and dislocation slip proceeds favorably in this plane. If the c/a ratio is lower than the ideal value (Ti, Zr, Be), then prismatic and pyramidal planes will be favorable for the slip.

Finally, close to the ideal value (Mg, Co, Cr, La, Ca), the basal slip could be partly substituted by the prismatic or pyramidal one. Activation of different slip systems strongly depends on the loading direction with respect to a slip plane and slip direction, temperature, or solute atoms.

Relation between the resolved shear stress and applied stress was first established by Schmid [1]. The Schmid law states that the CRSS (τ_{CRSS}) for activation of a slip system is equal to the stress applied to the material ($\sigma = \frac{F}{S_0}$, where F – applied load; S_0 – initial diameter of single crystalline cylinder) multiplied by the cosine of the angle between loading axis and normal to slip plane (φ) and the cosine of the angle between loading axis and the glide direction (λ_A) (Fig.2.1.1.):

$$\tau_{CRSS} = \frac{F}{S_0} \cdot \cos\varphi \cdot \cos\lambda_A = \sigma \cdot \cos\varphi \cdot \cos\lambda_A .$$

Then a ratio of shear to applied stress, which is also known as the Schmid factor (m) can be derived:

$$m = \frac{\tau_{CRSS}}{\sigma} = \cos\varphi \cdot \cos\lambda_A .$$

The shear stress has a maximum in the case, when $\kappa = 0$ – angle between direction of slip and axis of slip plane; $\varphi = \lambda_A = 45°$:

$$\tau_{\max} = \frac{1}{2} \cdot \frac{F}{S_0} .$$

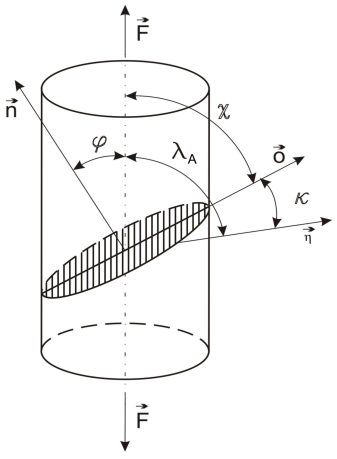

Fig. 2.1.1 Plastic deformation in single crystalline Mg. F – applied load; S_0 – initial diameter of a single crystalline cylinder; φ - angle between loading axis and normal to slip plane; λ_A - angle between loading axis and the glide direction; κ – angle between direction of slip and axis of slip plane; χ – angle between loading axis and slip plane; $\vec{o}$– slip plane, η – glide direction.

It is therefore obvious that deformation in a single crystalline material can initiate at different applied stresses, as CRSS for each dislocation slip system depends on the orientation of the crystal [2, 3]. Hence, m plays a moderation role and depends on both an orientation of the crystal and a direction of applied stress with

respect to the slip system. A detailed explanation of deformation in cylindrical single crystalline Mg is given in [4]. Deformation curve can be divided in three parts, which are characterized by different value of hardening coefficient. This coefficient is low at first part (the easiest slip is active), much higher at second part (activation of other dislocation slip systems) and decreasing at third part.

Plastic deformation of a material depends on the number of dislocations, or more precisely, on the dislocation density. The rate of generation and motion of dislocations remains constant (perfect plasticity), when they are not inhibited. However, this is an ideal assumption when no barriers are in the material. In reality, all polycrystalline materials have several types of dislocation barriers: dislocation locks, jogs, precipitated particles, twins, grain boundaries etc. Their presence is one of the major sources for dislocation ***pile-ups***. The direct result of dislocation pile-ups is a reduction of the generation rate at the dislocation source. The compression stress field of dislocation pile-ups reduces the effective applied force on the new-born dislocation at the source position, what results in an increase in slope of the stress vs. strain curve, so-called ***dislocation hardening*** effect. In fact, the input energy is stored in the dislocation microstructure and can be seen by different experimental observation methods. There are a lot of comprehensive studies of the interaction of dislocation stress field and barriers [5, 6].

Magnesium having the hexagonal close packed (*hcp*) lattice and the c/a ratio close to the ideal value (1.624) exhibits different deformation behavior in comparison to materials with *bcc* and *fcc* lattice. The main reason is a limited number of slip systems available at room temperature (RT). It is generally accepted that during plastic deformation in Mg four slip systems can be activated: basal, prismatic, pyramidal $\pi 1$ and pyramidal $\pi 2$ [7, 8], Fig. 2.1.2, Table 2.1.1.

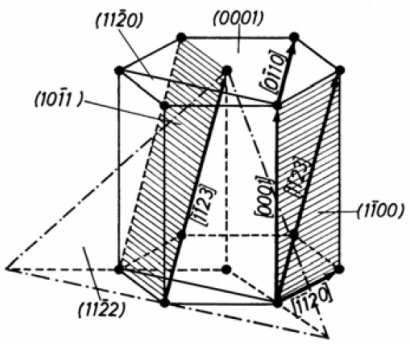

Fig. 2.1.2 Crystallographic slip planes and directions in Mg. Note that the Miller-Bravais indexing system is adopted.

It is well-known [9-14] that CRSS for the basal slip at RT is significantly lower than that for the other slip systems, and therefore, the basal slip is taken as the first activated mechanism in Mg and its alloys. On the contrary, the pyramidal $\pi 2$ $(11\bar{2}2)$ <a+c> slip requires either higher applied stress and/or elevated temperatures to be activated.

TABLE 2.1.1

Independent slip systems in *hcp* metals, cf. [15].

Direction	***Plane***	***Notation***	***Number of independent modes***
<a>	*Basal*	$\{0002\}\langle 11\bar{2}0\rangle$	2
<a>	*Prismatic*	$\{1\bar{1}00\}\langle 11\bar{2}0\rangle$	2
<a>	*Pyramidal*	$\{1\bar{1}00\}\langle 1120\rangle$	4
<a> + <c>	*Pyramidal*	$\{10\bar{1}1\}\langle 11\bar{2}\bar{3}\rangle$	4
<a> + <c>	*Pyramidal*	$\{2\bar{1}\bar{1}1\}\langle 11\bar{2}\bar{3}\rangle$	4
<a> + <c>	*Pyramidal*	$\{11\bar{2}2\}\langle 11\bar{2}\bar{3}\rangle$	4

However, according to the von Mises criterion for a homogeneous plastic deformation of polycrystalline materials, at least five independent slip systems are required [16]. In this regard, an additional mechanism, ***mechanical twinning***, particularly of the $\{10\bar{1}2\}\langle\bar{1}01\bar{1}\rangle$ type, providing elongation along *c*-axis, is supposed to play an important role to maintain a ductile mechanical behavior of Mg alloys.

The twinning mechanism can be described as follows: the shear stress on a certain crystallographic plane – so-called twin plane – reaches a threshold, atoms at one side of the twin plane move to a new position. The motion is parallel to the twin plane, Fig. 2.1.3. As a result, both sides of the twin plane have the same crystal structure but bear different orientations.

In other words, twinning in a crystalline material results in the formation of domain crystals inside their parent crystals (grains). They share the same crystal lattice in a symmetrical manner and are separated by twin plane – twin boundary (TB) [17]. While twinning may or may not contribute to plastic deformation

depending on the specific twinning mechanisms, it influences a substantial evolution of the microstructure and results in the formation of TB [17]. Generally, twins can be classified into grown twins (formed during crystal growth), annealing twins (induced by heat treatment, recrystallization), and deformation twins (generated by mechanical loading). It is obvious that only the last type of twins contributes to plastic deformation. TB similar to grain boundaries can effectively strengthen materials by impeding dislocation motion due to the slip discontinuity caused by the mirror symmetry. As a result of twinning, ductility and work hardening capability can increase.

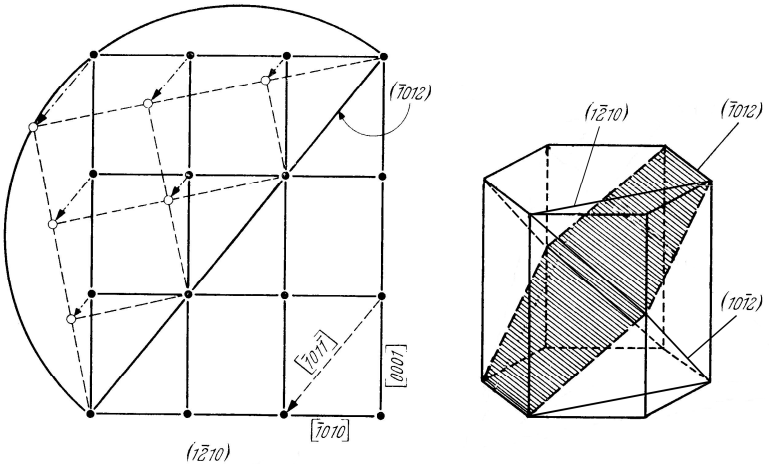

$K_1 \rightarrow (\bar{1}012)$

$K_2 \rightarrow (10\bar{1}2)$

Fig. 2.1.3 Classical illustration of the motion of a twinning interface under the action of shear stress. Illustration is presented for $\{10\bar{1}2\}\langle\bar{1}01\bar{1}\rangle$ extension twinning system.

Twin nucleation – beginning of the twinning process – is driven by local stress states and local atomic configurations at grain boundaries [18, 19]. Twin growth is driven by long-range stress states across grains through the motion of twin boundaries. It is realized either by gliding of twin dislocation on the twin plane along the twin direction – ***propagation*** – or migration of TB normal to the twin plane via nucleation and gliding of twin dislocation on the twin plane – ***twin thickening***.

Correspondingly to the crystallography of hexagonal structures, twin variants on different twin planes nucleate and grow during deformation with respect to a grain orientation (texture) and direction of applied load. These twin variants can interact with each other, form twin-twin junctions, which influence twin propagation and

thickening during loading, as well as detwinning, nucleation of new and/or secondary twins during reverse loading [20, 21]. Recently, the twin-twin interaction has been investigated experimentally in [22].

Twinning-detwinning is a key macroscopic mechanism observed in textured materials: rolled plates [23], extruded bars [24], and the extruded plates [21] during reverse loading. The twinning-detwinning model assumed that a grain has four potential operations associated with twinning-detwinning, Fig. 2.1.4:

- ***twin nucleation*** – introduction of the twinning process;
- ***twin growth*** corresponding to twin propagation and together with the twin nucleation increase the twin volume fraction;
- ***twin shrinkage*** corresponding to detwinning and decreases the twin volume fraction;
- ***re-twinning*** splits the twin band through detwinning or secondary twinning, decreasing the volume fraction of the original twin variant while increasing the volume fraction of the other twin variant.

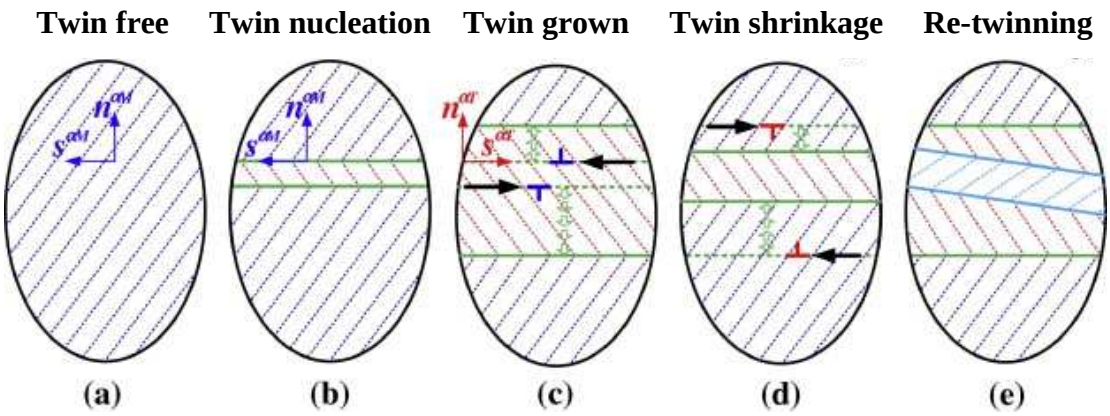

Fig. 2.1.4 Schematic representation of twinning-detwinning in a grain: (a) twin-free parent grain (matrix), (b) twin nucleation, (c) twin growth. (d) twin shrinkage, (e) re-twinning. Solid green lines represent twin boundaries. Lattices in the matrix and twin are represented by dotted blue lines and dotted red lines, respectively [25].

Table 2.1.2 summarizes the commonly observed twinning systems in *hcp* metals. The most common twinning system in Mg alloys is the $\{10\bar{1}2\}\langle 10\bar{1}1\rangle$ extension twinning [26], which results in a tensile strain parallel to the *c*-axis (hence sometimes the pseudonym: ”Extension twins” is used [27]) or a compression strain perpendicular to the *c*-axis [27-29]. This type of twin provides strain along the *c*-axis,

while basal and prismatic <a> glide cannot contribute to straining in this direction and for an activation of <c+a> pyramidal slip system a higher stress is typically required [30]. The extension twins are characterized by 86^o misorientation with respect to the original lattice. Twinning itself can accommodate strain up to 6.4%. In addition, the twins make orientations of the lattice more favorable for the activation of the dislocation slip (basal and prismatic), thus providing additional strain. Due to the 86° lattice reorientation caused by extension twins, detwinning could be easily activated in the twinned volumes during subsequent reverse loading [23, 31]. This process is characterized by a thickness reduction or disappearance of existing twin lamellae; that is, the twin lamellae are rotated back to the parent matrix orientation [32].

TABLE 2.1.2

Commonly observed twinning invariants in *hcp* metals, cf. [15]

κ_1	κ_2	η_1	η_2
$\{10\bar{1}2\}$	$\{10\bar{1}\bar{2}\}$	$\pm<10\bar{1}\bar{1}>$	$\pm<10\bar{1}1>$
$\{10\bar{1}1\}$	$\{10\bar{1}\bar{3}\}$	$<10\bar{1}\bar{2}>$	$<30\bar{3}2>$
$\{11\bar{2}2\}$	$\{11\bar{2}\bar{4}\}$	$1/3<11\bar{2}\bar{3}>$	$1/3<22\bar{4}3>$
$\{11\bar{2}1\}$	$\{0002\}$	$1/3<\bar{1}\bar{1}26>$	$1/3<11\bar{2}0>$

Various “compression” twinning modes (either of the $\{10\bar{1}1\}$ or $\{10\bar{1}3\}$ planes) could become active when applying compression strain parallel to the *c*-axis [33, 34] and results in 57^o misorientation with respect to the original lattice.

Earlier studies [29, 35] showed that plastic deformation of Mg and its alloys at RT, besides $\{10\bar{1}2\}$ extension twins, could proceed by $\{10\bar{1}1\}$ banding, which consists of $\{10\bar{1}1\}$ twinning followed by $\{10\bar{1}2\}$ twinning in the formed twin – so-called double twins or secondary twins. The new twin is characterized by 37^o misorientation with respect to basal planes in the initial crystal. A basal slip may be subsequently activated in the twinned material and, therefore, can enhance the ability of the material to accommodate plastic strain.

The currents emphasis for advancing applications of hexagonal materials is to improve deformability while preserving high flow strength. The fundamental principle is to adjust the relative activity among slip and twinning systems.

Therefore, the investigation of conditions for changing CRSS for specific deformation systems attracts a significant attention. An in-depth understanding of mechanisms and mechanics of deformation twinning in hcp metals is essential for designing novel Mg alloys with required properties.

2.2. Mechanical properties of magnesium alloys

Mechanical properties of polycrystalline materials are highly influenced, besides the crystal lattice, by a grain size and grain orientation. Deformation proceeds in each grain and is affected by deformation in neighboring grains. Hence, plastic deformation transfers from grain to grain.

Grain boundaries impede dislocation movement and the number of dislocations within a grain has an effect on their mobility. Existing dislocations and dislocations generated by Frank-Read sources move through a crystalline lattice (grain) until encountering a grain boundary. Large atomic mismatch between different grains creates a repulsive stress field to oppose continued dislocation motion. Dislocation pile-up occurs as a cluster of dislocations, which are unable to move across the boundary. Repulsive forces from dislocations act as a driving force to reduce the energetic barrier for diffusion across the boundary, allowing further deformation in the material. Decreasing grain size decreases the amount of possible pile-ups at the boundary, increasing the amount of applied stress necessary to move a dislocation across a grain boundary. The higher the applied stress needed to move the dislocation, the higher the yield strength (YS). Thus, there is then an inverse relationship between grain size and YS, as demonstrated by the Hall–Petch equation [36, 37]:

$$\sigma_{YS} = \sigma_0 + k \cdot d^{-1/2},$$

where σ_{YS} is the yield stress, σ_0 is a materials constant for the starting stress for dislocation movement (or the resistance of the lattice to dislocation motion), k is the strengthening coefficient (a constant specific to each material), and d is the average grain diameter.

However, when there is a large misorientation of the two adjacent grains, the dislocation may not necessarily move from one grain to the other and therefore a new source of dislocation in the adjacent grain is created.

The method of strengthening materials by changing their average crystallite (grain) size is also called grain-boundary strengthening. The stress-grain size relations are useful for describing the complete stress-strain behavior for polycrystalline materials and, therefore, these relations provide a reference for understanding the dependences of other properties on the grain size. In some cases, the grain size dependence of a particular property follows directly from this connection [38].

However, the Hall-Petch relation is limited to a grain size range ($d > 1\text{-}20\ \mu m$) for different materials. Plastic deformation is eventually a complex process based on different mechanisms (twinning, diffusion, slip along grain boundaries etc.).

The mobility of dislocations depends on solute atoms and precipitates in the material, as well. Precipitates can in particular increase CRSS for the basal slip and decrease CRSS for the non-basal slip. It should be noted that specifically the pinning effect of solute atoms on TB has recently attracted considerable attention. Periodic segregation of solute atoms at TB has been identified using scanning transmission electron microscopy (STEM) [39]. Theoretical calculations provide further insights for understanding the solute solubility along TB. Density functional theory calculations show e.g. that the solute solubility has a little dependence on the radius of solute atoms along TB, but varies considerably with stresses on TB [40].

As deformation depends on the orientation of the adjusted grains, the crystallographic texture – the distribution of crystallographic orientation of the grains in the polycrystalline material – significantly affects the deformation behavior.

In wrought Mg alloys, a texture is usually developed during the manufacturing processes (extrusion, rolling, forging, etc.) [41, 42]. For instance, rolled sheets of the Mg-based alloys exhibit a specific basal texture, where the orientation of basal planes is almost parallel to the sheet plane [43-45]. For AZ31 magnesium alloy [46], the orientation distribution of basal planes around the normal direction (ND) is wider in the rolling direction (RD) than in the transversal direction (TD). Deformation tests of this sheet show a distinct orientation dependence, ***planar anisotropy***, of YS and ultimate tensile strength (UTS), being lower in RD than in TD. The final texture of rolled magnesium alloy sheets can be in addition influenced by annealing and/or recrystallization [47-49].

Other wrought Mg alloys - extruded profiles - usually exhibit a strong basal texture, where the c-axes of the hcp unit cells in the majority of grains are perpendicular to the extrusion direction (ED). Consequently, a distinct ***tension–compression asymmetry*** at YS is linked mainly with twinning activity during loading along the ED is observed [50, 51]. It is noteworthy that extension twinning develops during the in-plane compression along the ED in an extruded Mg bar, and detwinning occurs in the twinned volumes at subsequent tensile loading along ED. It can be deduced that twinning–detwinning is a key deformation mechanism in Mg alloys during cyclic loading, which significantly influences the deformation behavior. Extensive experimental research has also focused on the role of twinning and detwinning in fatigue behavior [52-54]. Occurrence of detwinning during reverse loading was reported before, for example, in [12, 20, 23, 25, 31, 32, 55-58]. Despite intensive research, there are many open questions in this field regarding the twinning–detwinning process, the coexistence of detwinning and the formation of new twins, etc.

In additional to experimental studies, a lot of modeling of slip and twinning activities, which are responsible for deformation anisotropy, *asymmetry*, and damage mechanisms, were performed. Perhaps the most remarkable polycrystal plasticity models are those developed by the Tomé's group within the visco-plastic self-consistent (VPSC) scheme, which is a mesoscale mean-field model [59-63]. However, these methods still need improvement to capture the strain localization represented by twinning. The problem is the computational cost of re-meshing as well as lack of criteria for both twin nucleation and twin propagation.

In spite of the diverse grain orientations and the grain-size effect ***in polycrystalline wrought materials, the plastic deformation is controlled by the same mechanisms as in single crystals***. For example, the anisotropy should be similar in strongly textured polycrystals and in single crystals, and the degree of anisotropy depends on the strength of the texture [8, 29]. An analogy between deformation curves for single-crystalline and polycrystalline Mg with a strong texture, with orientation similar to that of the single crystal, was indeed observed by Kelley and Hosford [29]. Their study was followed by the work of Graff et al. [64], where mechanical tests and numerical modeling were collated for understanding the mechanisms of dislocation gliding and deformation twinning in single- and polycrystalline Mg. They attempted to describe links between micro- and mesoscale

processes. The influence of slip plane orientation and temperature on the deformation processes in Mg single crystals was discussed in Refs. [9-11, 29]. Therefore, the deformation behavior of textured Mg and its alloys can be interpreted in terms of deformation modes observed in single crystals.

The activation of basal and non-basal slip and twinning in Mg single crystals with different orientations was studied recently [65, 66]. Another experimental approach to the plasticity in Mg single crystals is based on spherical nanoindentation (i.e. a localized contact) [67-69]. Finite element simulation [67] indicates different spatial locations of the $\{10\bar{1}2\}$ extension twins for different indentation modes. Crystal plasticity analysis [69] suggests that indentation morphology results from the basal and <a+c> pyramidal slip systems in the case of (0001) indentation and from basal and twin systems in the case of $(1\bar{1}00)$ and $(11\bar{2}0)$ indentation. Multiple twinning and dynamic recrystallization processes during channel-die compression along the $<11\bar{2}0>$ direction in the *c*-axis extension were studied by Molodov et al. [70] using X-ray diffraction, electron backscattered diffraction (EBSD), and theoretical calculations.

2.3. Acoustic emission: definition and basic principles

Since the present thesis is aiming at investigation of active deformation mechanisms in Mg and its alloys using advanced *in-situ* method – acoustic emission (AE) technique – a short review of this technique is given in this section.

The ***AE technique*** is based on the detection of transient elastic waves, which are generated by a rapid release of energy due to sudden localized structure changes within a material [71]. Local processes producing the AE (e.g. dislocation motion, twinning, martensitic transformation, cracking etc.) are called ***sources of AE***. In the present thesis, the AE technique is used to follow a collective dislocation motion and twinning.

The output of the transducer (electrical voltage) is called ***AE signal***. Every AE signal could be ***parametrized***, and besides the raw AE signal the following AE parameters (Fig.4.3.1) could be determined and used for explanation of deformation mechanisms in metals:

- AE count rate ($\Delta NC/\Delta t$) – is the count number per unit time [72] at a given threshold voltage level.

- AE event – AE event starts by crossing a defined threshold voltage level and the end of the event is detected when the signal remains below the threshold voltage for a period exceeding a hit definition time (HDT). Afterwards, during a hit lockout time (HLT), the AE signal is not parametrized in order to filter out sound reflections.
- Peak amplitude of the AE event – A_{max} – the maximum of the AE signal voltage within an individual AE event. Time from the first crossing of the threshold voltage until peak amplitude of the AE event is called peak definition time – PDT.

The AE events and their peak amplitudes are usually determined in order to discriminate low and high amplitude sources of the AE signal.

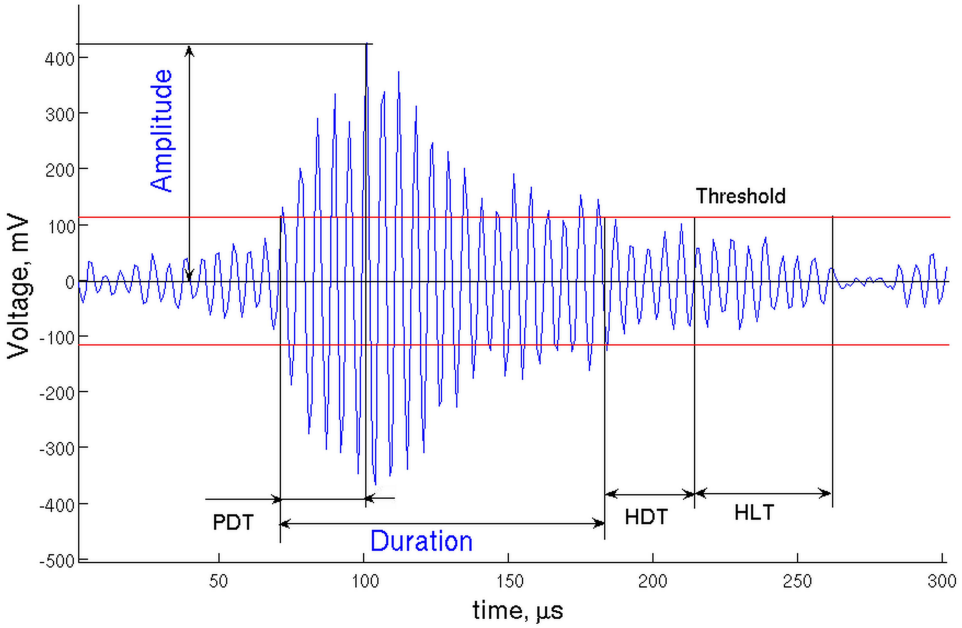

Fig. 4.3.1. Parametrization of AE signal [73].

AE signals have been conventionally separated into burst and continuous type emission. If the signal consists of pulses detectable from background noise and well enough separated in time so that there is not a lot overlap, then the emission is called ***burst emission***. If separation of individual pulses is not possible, then the emission is called ***continuous emission***.

Therefore, deformation processes of the material can be analyzed by the differences in the AE signal characteristics. For example, during plastic deformation of conventional polycrystalline materials the AE response is

characterized by a distinct peak close to the YS, which is followed by a rapid decay of the AE activity [13, 74]. The onset of the AE peak is explained in terms of rapid dislocation multiplication and movement at the beginning of plastic deformation. The subsequent decay of the AE activity is linked with shortening of moving dislocation lines and reduction of their flight distance, both due to increasing density of immobile dislocations [75-77].

In general, the AE response can be significantly affected by various factors: crystal structure, precipitates and solute atoms, grain size, deformation speed and temperature.

The AE can be produced by a dislocation motion only if many dislocations move nearly simultaneously within a small volume of material. Furthermore, the packet of dislocations must move far enough and fast enough, otherwise its motion will remain undetected. The crystal structure providing a defined amount of possible dislocation slip systems affects consequently the AE response. Variations of deformation rate and temperature affect the activity of specific dislocation slip systems and subsequently their AE response. Grain boundaries as well as precipitates are obstacles for dislocation movement, and therefore the AE signal becomes weaker. The velocity of dislocations movement plays rather important role in their interaction with solute atoms. For instance, if the velocity of the solute atoms and dislocations are nearly the same, then inhomogeneous deformation takes place and a serrated flow is observed on the deformation curve. This process, so-called Portevin-Le Chatelier effect, was also investigated using the AE technique in [78].

Results of investigations of twinning and dislocation processes in polycrystalline Mg alloys by the AE technique with respect to their chemical composition, producing way preparation and deformation conditions were presented in [71, 79-81].

The AE signatures (i.e. the differences in AE signal characteristics) belonging to various slip systems and twinning can be effectively studied during plastic deformation of single crystals, where specific conditions can be controlled by proper orientation of compressive or tensile axis with respect to the single-crystal orientation. The results can be subsequently applicable for the interpretation of complex deformation behavior in wrought Mg alloys. Results of AE measurements during mechanical testing on single crystals of various metals (Al, Zn, Fe, Cd, Ti, etc.) can be found e.g. in [71, 82-84]. However, except [84], I am not aware of

any AE study on Mg single crystals. The performance of existing AE instrumentation and improved processing of large amount of AE data open nowadays opportunities for detailed studies of the dynamics of deformation mechanisms in Mg single crystals. Therefore, in the present work, AE measurements in combination with other techniques for microstructural analysis are used to investigate strain path dependences of the deformation mechanisms during loading both Mg single crystals and textured Mg alloys.

Key points of Chapter 2

1. Deformation mechanisms in Mg and its alloys:
   - dislocation slip: basal, prismatic, pyramidal π1 and pyramidal π2
   - twinning: the $\{10\bar{1}2\}<10\bar{1}1>$ extension twinning (86^o misorientation angle); the $\{10\bar{1}1\}$ or $\{10\bar{1}3\}$ compression twinning (57^o misorientation angle).
2. Deformation twinning plays a crucial role in determining mechanical properties and texture evolution.
3. Twinning-detwinning is a key deformation mechanism observed in materials with a strong texture during reverse loading. Grain has four potential operations associated with twinning-detwinning: twin nucleation, twin growth, twin shrinkage and re-twinning.
4. The initial texture is responsible for the planar anisotropy and asymmetry of mechanical properties in wrought Mg alloys
5. An in-depth understanding of deformation mechanisms (particularly twinning and twinning-detwinning) in textured Mg alloys is essential.
6. Plastic deformation in polycrystalline wrought materials is controlled by the same mechanisms as in single crystals.
7. Acoustic emission technique is a powerful method to study the activities of deformation mechanisms.

Chapter 3

Aims of the thesis

The main goal of this work is a thorough description of the slip- and twinning activity in novel Mg alloys with controlled microstructure and texture. A genuine understanding will be achieved by means of advanced experimental methods. The following particular tasks have to be accomplished:

- obtaining a comprehensive set of AE data for specific deformation mechanisms, which were activated during compression loading of Mg single crystals. These data will be used as a reference for analysis of twinning and dislocation processes in polycrystalline Mg alloys with a strong texture.
- investigation of active deformation mechanisms in extruded Mg alloys during a one-cyclic test consisting of pre-compression and following reverse tensile loading. Particularly, the twinning-detwinning process will be investigated in detail with respect to the initial microstructure of Mg extrusions.
- analysis the influence of rolling processes (conventionally rolling of cast slab and twin roll cast strips), represented by different initial textures, on the deformation behavior of the sheets.

Chapter 4

Experimental materials and methods

4.1. Experimental materials

In the present work, Mg single crystals and polycrystalline wrought Mg alloys in the form of extruded profiles and hot rolled sheets were used.

Mg single crystals of commercial purity (99.95%) were grown by a modified vertical Bridgman technique using specially oriented single crystalline seeds (*c*-axis parallel to the growth direction or 45 degree tilted).

Magnesium alloys used in experiments were designated according to the ASTM Alloy Designation B275 - Codification of Certain Nonferrous Metals & Alloys. Nomenclature describes the major alloying elements and their nominal percentage content. For instance, AZ31 Mg alloy contains – 3 wt.% Al and 1wt.% Zn or ZE10 contains 1 wt.% Zn and less than 1 wt.% E – RE elements (mainly Ce, Y, Nd). Extruded and rolled materials used in this work were received from the Magnesium Innovation Centre, Helmholtz-Zentrum Geesthacht (MagIC, HZG, Germany). Materials were prepared from gravity cast ingot with selected chemical compositions, which were homogenized at 350 ^{o}C for 24 h.

For investigation of deformation mechanisms in extruded profile, the following magnesium alloys were chosen as model material: AZ31 (*Mg + 3 wt.%Al + 1 wt.%Zn + 0.3 wt.%Mn*) and ZE10 (*Mg + 1.3 wt.% Zn + 0.1 wt.% Ce*). Alloys were fabricated using indirect extrusion at 300 °C with an extrusion rate of 5 m/min and 10 m/min, respectively. The extrusion ratio was 1:30, which resulted in round bars with a diameter of 17 mm. A scheme of the indirect extrusion process is presented in

Fig. 4.1.1. In this case the material flows opposite to the pressing direction. The resulting properties of materials, especially grain size, are significantly influenced by extrusion speed, temperature and extrusion rati. For the present study, the following extruded Mg alloys with a various microstructure were selected:

- the extruded profile of AZ31, which exhibits a bimodal microstructure with an average grain size of 20 ± 1 μm. There are larger grains elongated in ED, along with a distinct fraction of grains with smaller sizes.
- the extruded profile of the ZE10 magnesium alloy, which has a fully recrystallized microstructure with an average grain size of 26 ± 1 μm and a more homogeneous grain structure comparing to AZ31.

Their microstructure and grain size distribution are presented in Fig. 4.1.2 and 4.1.3, respectively.

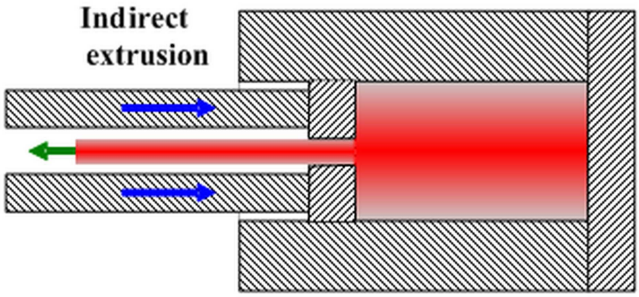

Fig. 4.1.1. Scheme of the indirect extrusion process [85].

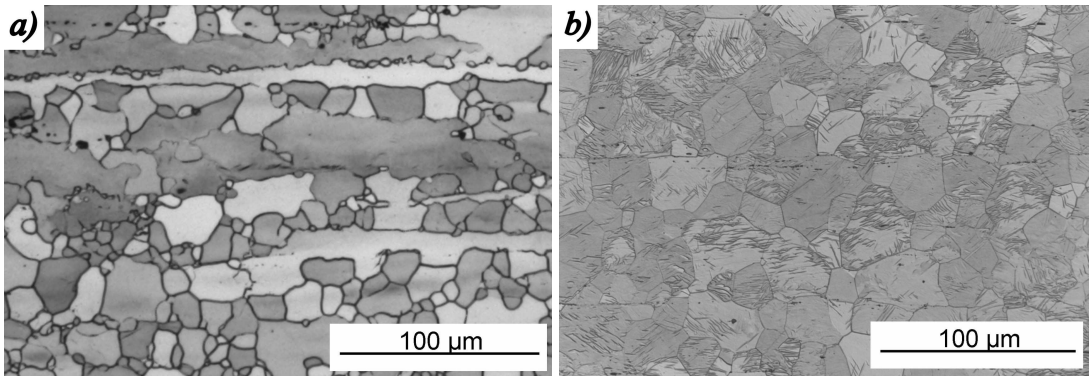

Fig. 4.1.2. Microstructure of extruded Mg alloys: (a) AZ31, (b) ZE10.

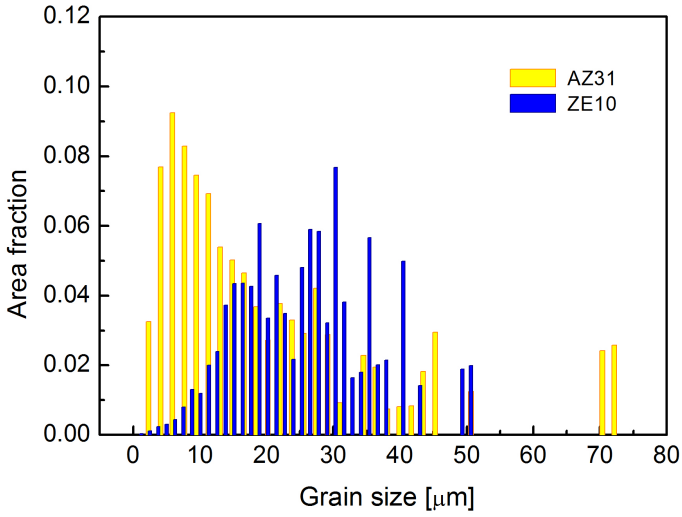

Fig. 4.1.3. Grain size distribution of extruded AZ31 and ZE10.

In order to study the anisotropy of the rolled materials, AZ31 *(Mg + 3wt.%Al + 1wt.% Zn)* and ZE10 *(Mg + 1.3wt.% Zn + 0.2wt.% Ce + 0.1 wt.% La)* magnesium alloys were prepared in a form of cast slabs and twin roll cast (TRC) strips. Both alloys were subsequently subjected to conventional rolling into sheets of the thickness of 1.5 mm. Hereafter experimental materials are denoted as the rolled AZ31 (ZE10) and the rolled AZ31 (ZE10) TRC strips. Schemes of the TRC process and conventionally rolling are presented in Fig. 4.1.4.

In the TRC process, Mg alloy strips are produced directly from liquid Mg alloys. Molten Mg metal is heated over the melting point and then dragged onto the surface of the lower roll through a nozzle. Solidification starts immediately after the melt leaves the nozzle, just between the two rolls. Hence, the tip sustains the melt at a constant level thereby distributing the melt to the required strip width.

In the conventional rolling process, Mg-based alloy sheets are fabricated by hot-rolling from the slabs prepared by direct chill casting. In the present work, conventional rolling was applied for cast slabs as well as for TRC strips to achieve the same thickness.

All sheets are characterized by a homogeneous microstructure, presented in Fig. 4.1.5.

a) b)

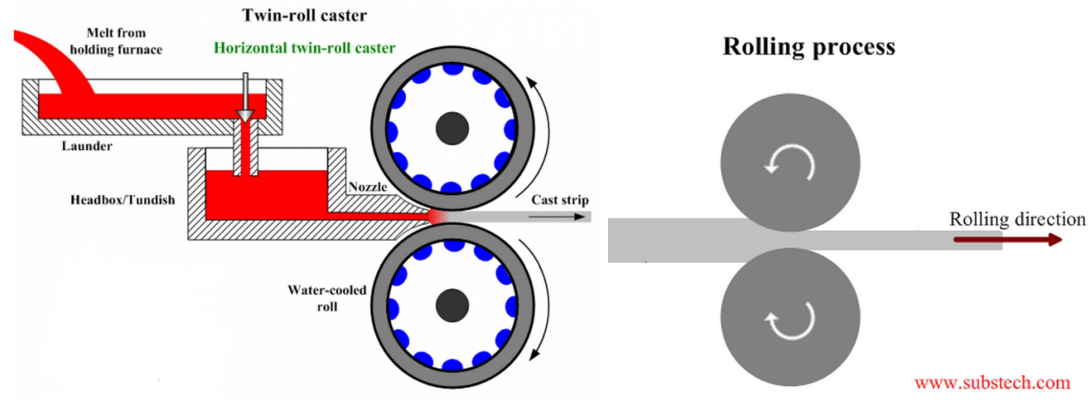

Fig. 4.1.4. Scheme of (a) the twin roll casting (TRC) process and (b) the conventionally rolling process [85].

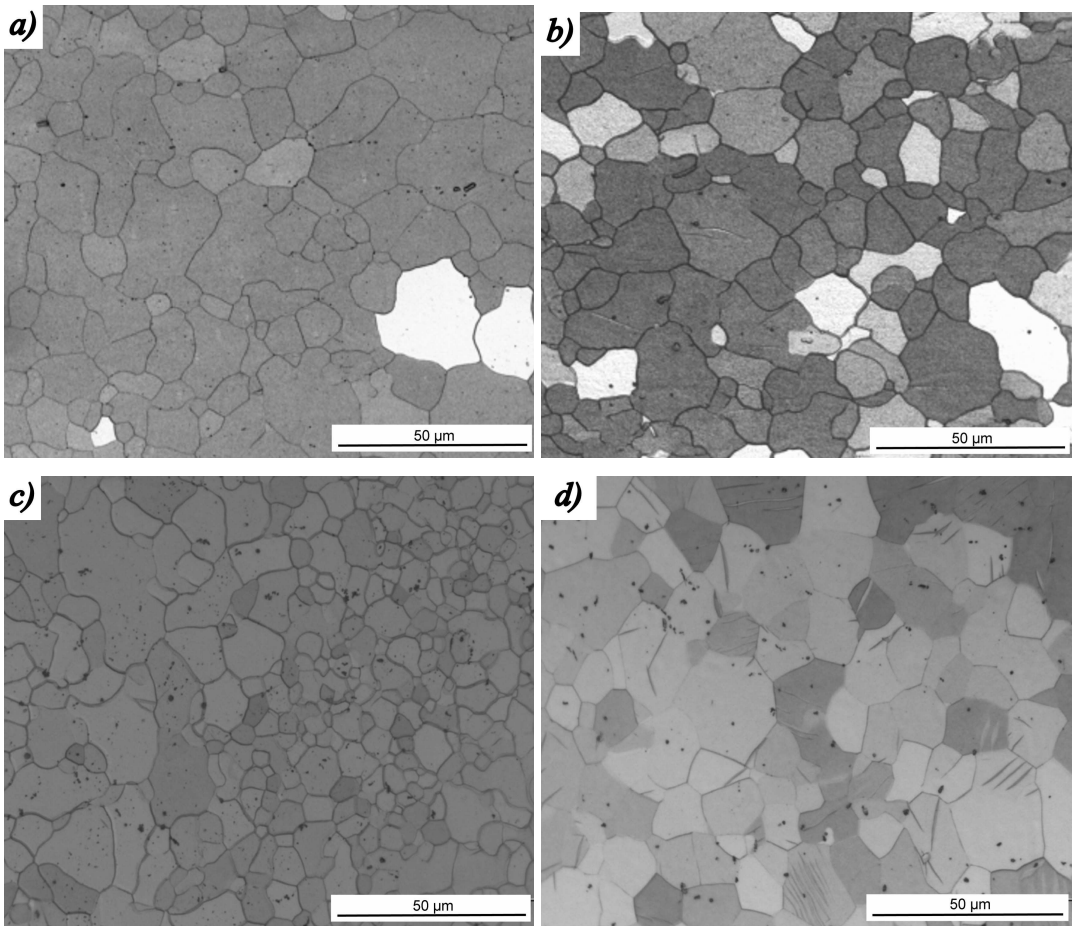

Fig. 4.1.5. Microstructure of rolled AZ31 (a), ZE10 (b) and of the rolled TRC strips of AZ31 (c), ZE10 (d).

4.2. Deformation tests

All deformation tests were performed at RT in universal testing machines Instron 5882 and Zwick Z50 at a constant strain rate of 10^{-3} s^{-1}. The data were stored with a sampling frequency of 10 Hz.

Mg single crystals were subjected to uniaxial and channel-die compression tests. The cutting of the specimens (5 x 6 x 10 mm^3) for deformation tests was performed by spark erosion. Mg single-crystalline specimens were uniaxially compressed in four different directions, see Fig. 4.2.1: along the $<11\bar{2}2>$, *c*-, $<10\bar{1}0>$, and $<11\bar{2}0>$ axis.

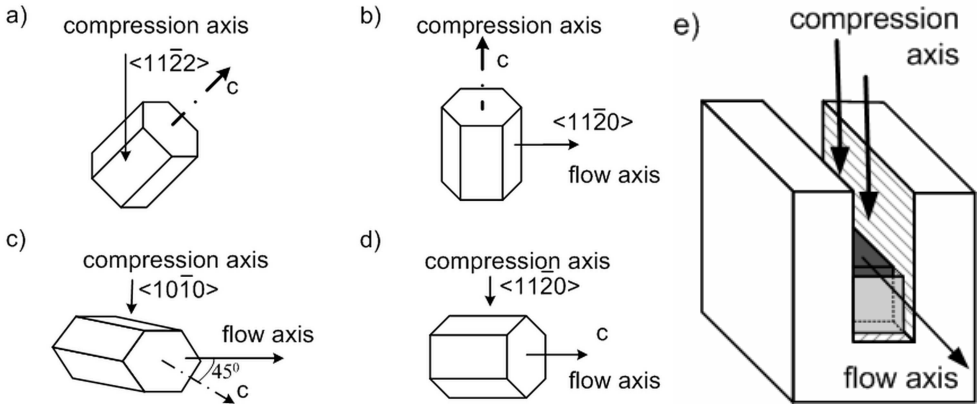

Fig. 4.2.1. Orientations of Mg single crystals for channel-die and uniaxial compression tests: along the (a) $<11\bar{2}2>$, (b) *c*-, (c) $<10\bar{1}0>$, and (d) $<11\bar{2}0>$ axis; the flow axis is given for channel-die experiment; (e) scheme of channel-die compression experiment.

The channel-die compression tests (Fig. 4.2.1e) were performed on Mg single crystals in three different crystallographic directions with a suppression of the material flow in the specific direction (Fig. 4.2.1b-d). This test was not performed for the first orientation (compression along the $<11\bar{2}2>$ axis), because constraining to one flow direction in this case does not mean any change for the dominant deformation mechanism (basal slip). For the next orientation (Fig. 4.2.1 b), the stress was applied perpendicular to the basal planes with the flow possible in the $<11\bar{2}0>$ direction, i.e. the material flow in the $<10\bar{1}0>$ direction was impossible. During compression perpendicular to the prismatic $(10\bar{1}0)$ and $(11\bar{2}0)$

planes (Fig. 4.2.1 c,d), the constraint directions were chosen in order to allow material flow in the $< 0001 >$ direction.

Extruded Mg alloys were subjected to one-cycle tests, i.e. pre-compression followed by a tension tests (Fig. 4.2.2). Samples with a gauge length of 15 mm, a diameter of 8 mm, and screw heads on both ends were machined from the round extruded bar parallel to the ED.

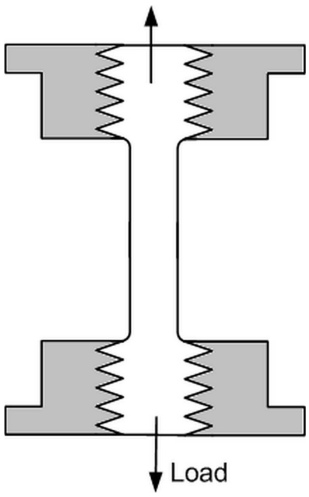

Fig. 4.2.2. Scheme of pre-compression followed by tension — that is, one-cycle test — of extruded Mg alloys.

For tensile tests of rolled Mg alloys, samples with a gauge length of 35 mm and width of 6 mm were machined. The specimens were deformed along RD, TD and direction tilted by 45° from RD to TD.

All obtained experimental data were analyzed by the Origin software package from Origin Lab.

4.3. Acoustic emission technique

To monitor the AE activity, a computer controlled PCI-2 (***Physical Acoustic Corporation***) device was used. Continuous storage of AE signals was performed with 2 MHz sampling frequency. A miniaturized MST8S piezoelectric transducer (Dakel-ZD Rpety, Czech Republic) with a diameter of 3 mm and flat response in a frequency band from 100 to 600 kHz was used. In case of deformation tests of Mg single crystals, i.e. with a small size of the specimens, the sensor was glued to the holder as close to the specimen as possible. In case of one-cycle tests of extruded profiles and tensile tests of rolled sheets, the sensor was clamped directly on the specimen surface. A preamplifier with a gain of 40 dB was used. The full scale of the A/D converter was ±10 V giving the total gain of 100 dB. The background noise

during the performed tests did not exceed 1 mV (≈ 20 dB). With respect to this value, the threshold level of detection was set to 26 dB to evaluate a comprehensive set of AE parameters. To separate individual AE events, HDT and HLT were set to 800 and 1000 μs, respectively.

4.4. X-ray diffraction

To determine the initial orientation of Mg single crystals and their texture after channel-die test as well as the texture of polycrystalline (extruded and rolled) Mg alloys, the X-ray PANalytical XPert diffractometer using CuKα radiation was used. Measurements were performed at MagIC HZG Geesthacht. The texture measurements were performed on polished samples (perpendicular to the ED and ND for extruded and rolled materials, respectively). A computer code MTEX [86] was applied to calculate the orientation distribution function and to recalculate full pole figures in a defined plane.

4.5. Light and scanning electron microscopy

The microstructure of the polycrystalline Mg alloys was investigated by an OLYMPUS GX51 light microscope (LM) equipped with the PIXELINE® camera and by field emission gun scanning electron microscopes (SEM) Zeiss Ultra 55 and FEI Quanta 200 equipped with EDAX/TSL EBSD systems.

For both types of microscopic observations, the specimens were grinded on SiC papers and subsequently polished by diamond pastes down to 0.25 μm particle size. For investigation by LM, the polished surfaces along extrusion and rolling directions were then etched in the solution of 50 ml ethanol, 9 ml water, 4 ml acetic acid, and 6 g picric acid for 6-10 s.

For detailed microstructure observation by SEM, particularly for obtaining orientation maps by the EBSD technique, the sample surface after grinding and polishing was subsequently electropolished in an AC-2 solution (Struers) at -26°C, 33 V for 90 s. To improve the quality of the surface prior to measurements, the samples were rinsed in 0.5% nital (nitric acid in methanol) and ethanol, and dried with pressurized air.

Electron backscatter diffraction (EBSD) is a useful technique for investigating the crystal orientation with high spatial resolution. This is particularly important for

the work carried out herein, where the twinning activity in textured Mg alloys is to be investigated.

The EBSD system is installed inside SEM. To perform the EBSD mapping, the polished specimen should be mounted to the holder with a tilting angle of 70°. The emitted electrons from an electron gun collide with the material and as a result, the backscattered electrons, which satisfy the Bragg‘s condition for many different planes, form Kikuchi pattern (Fig. 4.5.1). Each pattern corresponds to a specific crystallographic orientation and the Miller indices can be indexed by Hough transformation for each obtained Kikuchi pattern.

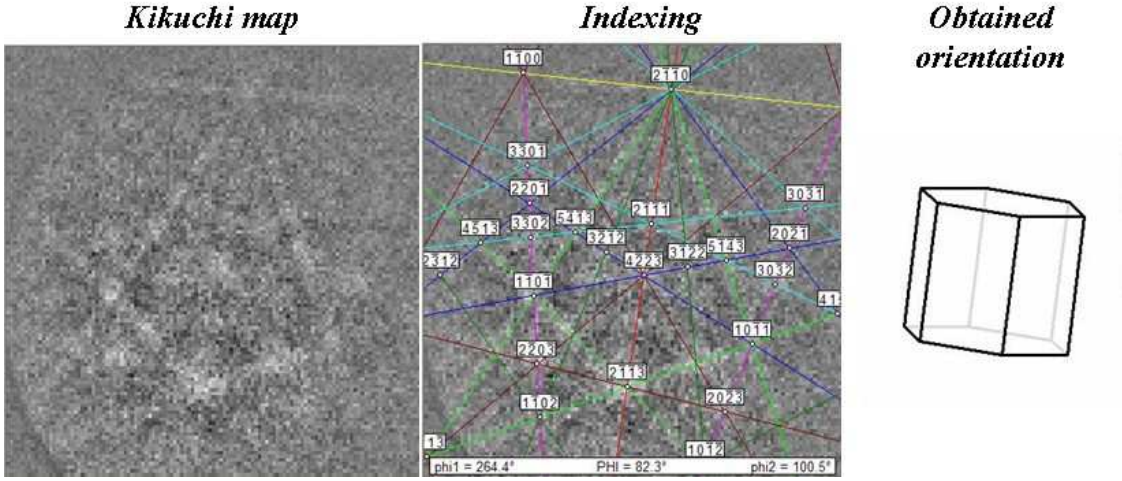

Fig. 4.5.1. A typical Kikuchi pattern obtained by EBSD. Each band corresponds to reflection atom plane.

The EBSD mapping for investigated Mg alloys in present work was carried out with a step size of 0.4 µm and an acceleration voltage of 15 kV. The data acquisition software program TSL-OIM Analysis 7.0 was used to process the EBSD data.

Key points of Chapter 4

1. To investigate the deformation mechanisms in Mg alloys with controlled microstructure (texture), indirectly extruded and rolled AZ31 and ZE10 alloys were chosen.
2. Acoustic emission measurements can be performed concurrently with the deformation tests, allowing real-time monitoring of active deformation mechanisms.
3. To obtain AE data for specific deformation mechanisms, Mg single crystals, were deformed in specific crystallographic orientations:
   - uniaxially compressed along $<11\bar{2}2>$, *c*-, $<10\bar{1}0>$, and $<11\bar{2}0>$ axis;
   - plane strain compressed along *c*-, $<10\bar{1}0>$, and $<11\bar{2}0>$ axis.
4. To investigate twinning – detwinning process in extruded Mg alloys, specimens were first subjected to pre-compression with following tension — that is, one-cycle tests.
5. To reveal the influence of twinning on plastic deformation in the rolled materials, rolled slab and rolled TRC strip of AZ31 and ZE10 were tensile loaded along RD, TD and direction tilted by 45° from RD to TD.
6. SEM (including EBSD) was employed for precise microstructure observation to investigate the twin/slip activity in polycrystalline Mg alloys.

Chapter 5

Results and discussion

5.1. Mg single crystals: AE response of basic deformation mechanisms

5.1.1. Experimental results: uniaxial and channel-die compression

Mg single crystals were subjected to uniaxial and channel-die compression tests to obtain the AE response for a specific deformation mechanism. The AE signal was recorded during compression of Mg single crystals in defined orientations (Fig. 4.2.1). For relating the AE signal to a particular stage of the deformation curve, the most convenient representation is to plot the AE signal together with the actual stress in the same plot as a function of time. The proportionality between time and strain is given by the constant strain rate of $10^{-3}s^{-1}$.

Deformation curves and AE response for ***uniaxially compressed*** Mg single crystals are presented in Fig. 5.1.1. For the specimen with a favorable orientation for basal slip (compression along the $<11\bar{2}2>$ axis, Fig. 5.1.1a), the stress is accumulated very slowly and the stress-time curve exhibits a very long stage I (easy glide). On the contrary, a strong hardening behavior (stage II) occurs already at the very beginning of the test during uniaxial compression along the *c*-axis, Fig. 5.1.1b.

The deformation curves for compression along the $<10\bar{1}0>$ and $<11\bar{2}0>$ axis (Fig. 5.1.1c,d) exhibit a relative long stage I, and a more distinct increase of the stress was observed in the last case.

More information was obtained from such AE parameters as the AE count rate and the peak amplitudes of the AE events. Their correlation with the deformation curves is presented in Fig. 5.1.2. Compression of Mg single crystal along the $<11\bar{2}2>$ axis is accompanied by a relatively weak AE signal at the beginning of plastic deformation, which then slightly increases and stays stabilized till the end of the test. The AE count rate is relatively constant during the test (Fig. 5.1.2a), as well. During compressing along the *c*-axis, a low AE activity is observed during the whole test (Figs. 5.1.1b, 5.1.2b).

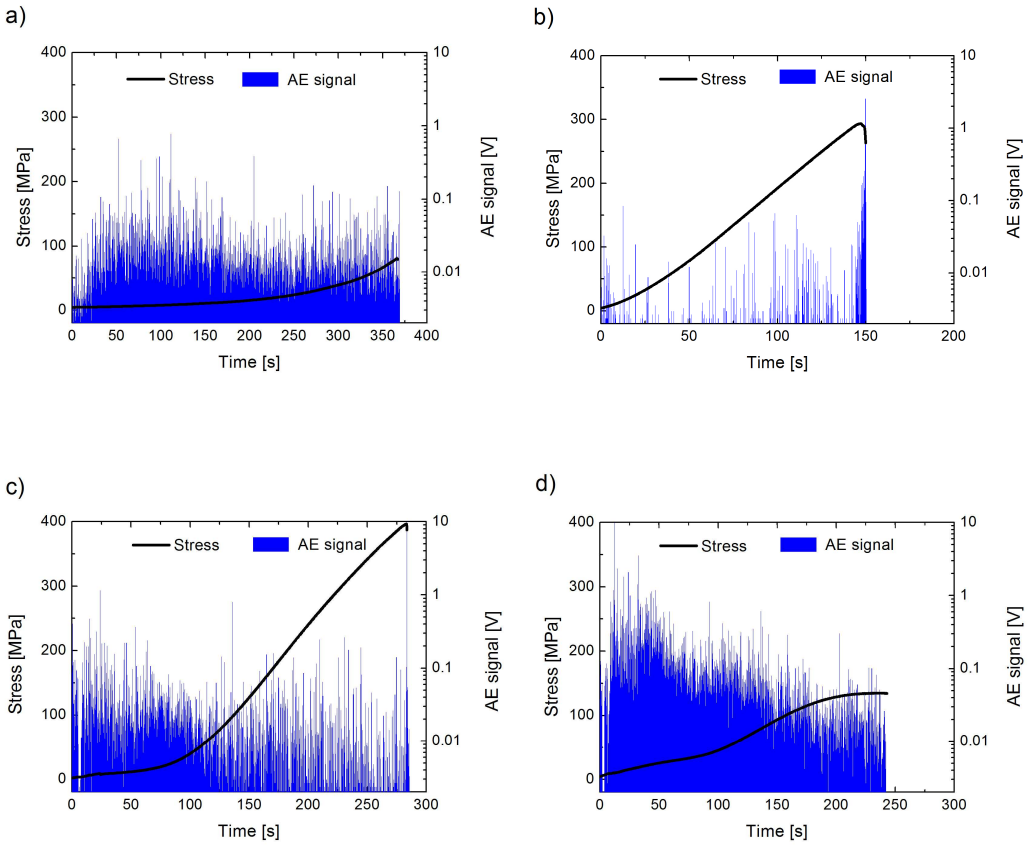

Fig. 5.1.1. Time dependence of the stress and the AE signal voltage for deformed Mg single crystals with respect to various loading axis during uniaxial compression: (a) $<11\bar{2}2>$, (b) *c*-, (c) $<10\bar{1}0>$, (d) $<11\bar{2}0>$.

The AE count rate and the peak amplitudes of the AE events exhibit their maxima at the beginning of plastic deformation during uniaxial compressing along the $<10\bar{1}0>$ and $<11\bar{2}0>$ axis. The AE signal voltage (Fig. 5.1.1c,d), as well as the AE count rate (Fig. 5.1.2c,d), are higher by a factor of approx. 6, during

the compression along the $<11\bar{2}0>$ axis, comparing to the compression along $<10\bar{1}0>$. Moreover, smaller amount of AE events with higher peak amplitudes can be seen in last case in comparison with compression along the $<11\bar{2}0>$ axis (Fig. 5.1.2d-c).

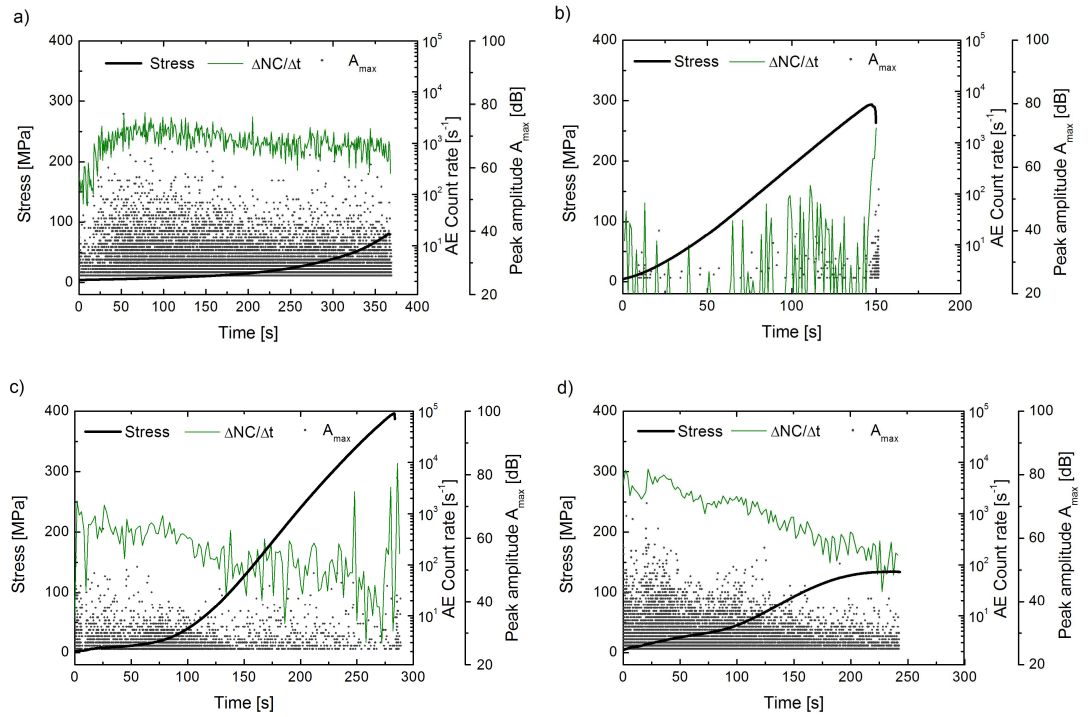

Fig. 5.1.2. Time dependences of the stress, the AE count rate, and the peak amplitudes of the AE events for deformed Mg single crystals with respect to various loading axis during uniaxial compression: (a) $<11\bar{2}2>$, (b) *c*-, (c) $<10\bar{1}0>$, (d) $<11\bar{2}0>$.

During ***channel-die compression*** along the *c*-axis, plastic deformation proceeds in a similar way as during uniaxial compression. The rapid increase in stress is evident from the very beginning of the test. A small amount of AE events was observed at the beginning of the test. Shortly before fracture, the AE signal was emitted by a crack propagation. As experimental results showed similarity in AE response for both types of compression along the *c*-axis, the deformation curve with a concurrent AE measurement for channel-die compression is not plotted here.

Deformation curves with the AE response (AE signal and its parameters) for channel-die compressed Mg single crystals along the $<10\bar{1}0>$ and $<11\bar{2}0>$ axis are presented in Fig. 5.1.3 and Fig. 5.1.4. The deformation curves exhibit a relative

long stage I with a low work hardening. The work hardening rate for loading along the $<11\bar{2}0>$ axis is slightly higher than that along the $<10\bar{1}0>$ axis.

The AE signal is weaker for the compression along the $<11\bar{2}0>$ axis, but for both orientations the AE signal shows a burst character with high amplitudes (Fig. 5.1.3).

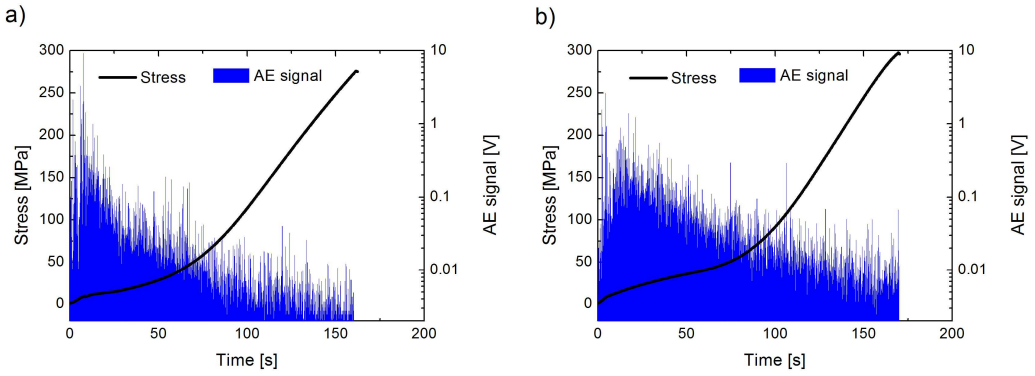

Fig. 5.1.3. Time dependences of the stress and AE signal voltage for deformed Mg single crystals with respect to various loading axis during channel-die compression: (a) $<10\bar{1}0>$, (b) $<11\bar{2}0>$.

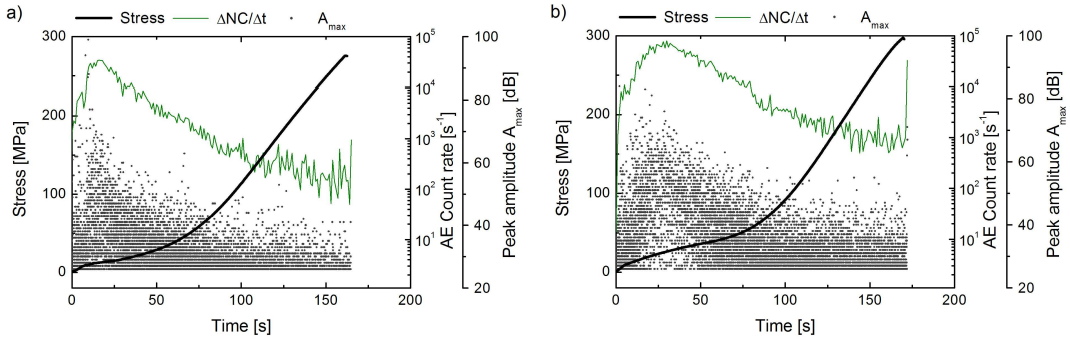

Fig. 5.1.4. Time dependences of the stress, the AE count rate, and the peak amplitudes of the AE events for deformed Mg single crystals with respect to various loading axis during channel-die compression: (a) $<10\bar{1}0>$, (b) $<11\bar{2}0>$.

The AE count rates in both cases exhibit a maximum at the beginning of plastic deformation, which is followed by a slow decrease (Fig. 5.1.4). It should be noted that higher values of the AE count rate are observed during the whole test for the compression along the $<11\bar{2}0>$ axis in comparison to the $<10\bar{1}0>$ axis compression.

To reveal the possible difference in twinning activity during channel-die compression along the $<10\bar{1}0>$ and $<11\bar{2}0>$ axis, ***texture measurements*** before and after loading were performed and the results are presented in Fig. 5.1.5. The texture of the single crystal prior to deformation (Fig. 5.1.5a,c) was characterized by very high intensity peaks corresponding to the orientation ($\varphi1$, Φ, $\varphi2$) = (90°, 45°, 30°) and (90°, 90°, 30°) in Euler space (Bunge notation).

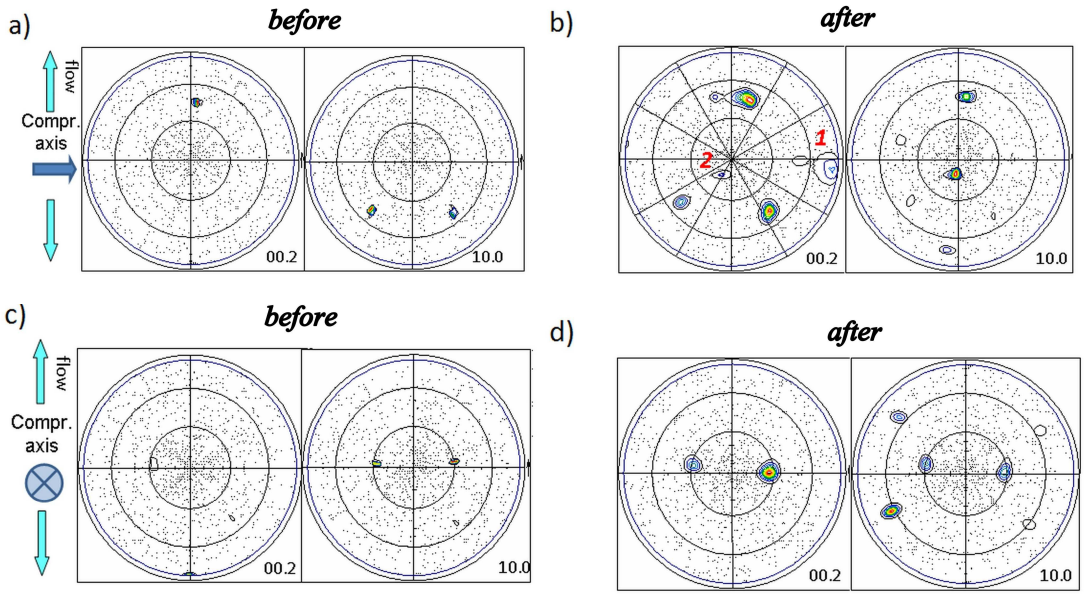

Fig. 5.1.5. Texture development in the single crystals during channel-die compression along the $<10\bar{1}0>$ and $<11\bar{2}0>$ axis: prior to (a, c) and after (b, d, respectively) loading.

The texture of the specimen, compressed along the $<10\bar{1}0>$ axis, consists of an initial component (90, 45, 30), two symmetrical components (225, 45, 30) and (300, 45, 30) (which duplicate the intensity peaks in the $(10\bar{1}0)$ pole figure of the initial texture) and further two weak components (marked in the Fig. 5.1.5b as zone 1 and 2, respectively). It is worth noting that the weak intensity peaks which correspond to the initial orientation (90, 45, 30) were slightly rotated, and therefore did not match the exact orientation (90, 45, 30) as for the initial state (Fig. 5.1.5a).

The texture of the specimen after compression along the $<11\bar{2}0>$ axis consists of an initial component and two new symmetrical texture components (0, 30, 30) and (180, 30, 30) with an angle of 30° between the direction of their respective *c*-axes and the compression axis (Fig. 5.1.5d). The weak intensity peaks, which correspond

to the initial orientation, were slightly rotated around the compression axis, and as in the previous case they did not match the exact orientation. Moreover, the textures after compression became asymmetrical in terms of their relative intensity in the (0002) and $(10\bar{1}0)$ pole figures.

5.1.2. Discussion: AE signatures for basal, pyramidal slip and twin nucleation

The main difference between the uniaxial and the channel-die compression tests is in the direction of plastic flow of the material. Basically, in the case of uniaxial compression along defined loading axis, the material flow is perpendicular to the loading direction without constraints. In case of the channel-die test (Fig. 4.2.2), the plastic deformation is realized in one direction only and the material flow is restricted in one direction (in our case constraining is applied for the $(11\bar{2}0)$ and $(10\bar{1}0)$ planes). Such configuration can eliminate specific deformation mechanisms.

The analysis of the Schmid factor *m* [8] reveals that the ***compression of a single crystal along the*** $<11\bar{2}2>$ ***axis*** (45° tilted *c*-axis from the loading direction) is the ideal condition for the activation of ***basal slip***. Other types of dislocation slip are less engaged in the stage I of the deformation due to higher CRSS [2, 3, 16, 29, 35, 87]. Therefore, the AE activity during uniaxial compression along the $<11\bar{2}2>$ axis can be related to basal slip. From our experimental results, it can be clearly seen that the collective movement of basal dislocations in single slip mode produces a low amplitude AE signal.

The deformation behavior during both uniaxial (Fig. 4.2.1b) and channel-die compression (not presented here) along the *c*-axis is similar. In [8] it was shown that in the case of ***compression along the c-axis***, the *m*-values for the basal, prismatic and pyramidal $\pi 1$ $\{10\bar{1}1\}$ slip systems are zero. Furthermore, it was shown that the $\{10\bar{1}2\}$ twinning system is not active in such orientation [8, 28, 80]. In this case, the 6 equivalent ***pyramidal π2 slip*** systems are active. Considering the cross-slip of <c+a> dislocations onto $\{2\bar{1}\bar{1}2\}$ and $\{10\bar{1}1\}$ planes, 12 slip systems are available to accommodate plastic deformation. Very strong hardening is observed, which can be explained by dislocation forest [8]. The very low AE activity (Fig. 5.1.2b) during the whole test is consistent with a rapid immobilization of dislocations due to

the creation of strong obstacles. This type of dislocation slip was also identified experimentally by the TEM observations in earlier works [88, 89]. Theoretical studies of the evolution of the relative activities of various slip systems with increasing strain [64] show the prevailing pyramidal <c+a> slip, as well. As deformation curves and the AE response for both uniaxial and channel-die compression are similar, it can be summarized that constraining of the $(10\bar{1}0)$ planes has practically no influence on plastic deformation during the compression along the *c*-axis.

Hereafter, the deformation behavior in Mg single crystals during loading along the $<10\bar{1}0>$ and $<11\bar{2}0>$ axis will be discussed, first in general for uniaxial compression and then with restriction of plastic flow in the case of channel-die compression.

During ***compression along the*** $<10\bar{1}0>$ ***and*** $<11\bar{2}0>$ ***axis***, plastic deformation in the *hcp* crystal with c/a equal 1.624 (Mg) is accommodated mainly by the ***prismatic slip and twinning***. For compression along the $<10\bar{1}0>$ axis, the *m*-values for prismatic (0.43) and basal (0) slips, and for an extension twinning system (0.5) were calculated in [8]. Analogous calculation of *m* for compression along the $<11\bar{2}0>$ axis for prismatic (0.43) and basal (0) slips, and for extension twinning system (0.37) are presented in [8], as well. The activation of particular deformation mechanisms depends on both the Schmid factor and the CRSS (the best combination is a high Schmid factor and a low CRSS). CRSS for the prismatic slip is higher than the activation stress for twinning. Consequently, the plastic deformation during uniaxial compression along the $<10\bar{1}0>$ and $<11\bar{2}0>$ axis proceeds first of all by twinning, giving a stronger hardening by comparison with the basal slip activated during the compression along the $<11\bar{2}2>$ axis [8, 29, 35, 64].

Twins of the $\{10\bar{1}2\}<\bar{1}01\bar{1}>$ type in Mg can accommodate the extension up to 6.4% along the *c*-axis [90]. Furthermore, reorientation of the basal planes due to the extension twinning (rotation of basal planes by 86.3^{o} with respect to their original orientation [9]) promotes additional plastic deformation realized by easier basal slip in the reoriented grains. It was shown by EBSD mapping [11, 69, 70] and TEM investigation [67, 68] that twins mainly nucleate at the beginning of the compression along the $<10\bar{1}0>$ and $<11\bar{2}0>$ axis.

The calculation of m for extension twinning [80] with respect to loading direction shows that during ***compression along the*** $<10\bar{1}0>$ ***axis six variants of twinning*** can be active at the beginning of plastic deformation. Two of them have m = 0.5 and four variants have m = 0.15. In the case of ***compression along the*** $<11\bar{2}0>$ ***axis***, only ***four variants*** of twinning having m = 0.35 can be active with the same probability. Then the higher flow stress (more pronounced hardening) and extended stage I during compression along the $<11\bar{2}0>$ axis comparing to the $<10\bar{1}0>$ axis could be ascribed to a higher twinning activity of the four variants with the same m.

Hence, it can be concluded that AE originates from extension twins during compression along the $<10\bar{1}0>$ and $<11\bar{2}0>$ axis. In earlier works [83, 91] it has been found that the twin nucleation produces a detectable AE in contrary to the twin growth. The high amplitude AE signal can be therefore clearly associated with the twin nucleation.

The difference of the cases with loading along the $<10\bar{1}0>$ and $<11\bar{2}0>$ axis, i.e. the rotation of crystal along the c-axis by 30 degrees, is clearly reflected in the AE response. The higher twinning activity during compression along the $<11\bar{2}0>$ axis is consistent with the higher AE response (Fig. 5.1.2) for this orientation. This confirms that in this orientation the four variants of extension twins with m of 0.35 are more likely to be activated than the two variants with the higher m-value in the case of compression along the $<10\bar{1}0>$ axis. It should be noted that a minor part of the AE response could be also produced by additional basal slip in reoriented crystal planes similar to compression along the $<11\bar{2}2>$ axis.

The activation of additional (non-basal) slip systems with higher CRSS is clearly manifest as a strong increase in the engineering stress (stage II on deformation curve) for both orientations (Fig. 5.1.1c,d and Fig.5.1.2c,d). The dislocation density increases with increasing plastic deformation, what leads to a decrease in the free path of moving dislocations, and thus it explains the reduction of the AE activity (similar situation as in the stage II during compression along the c-axis).

During the ***channel-die compression along the*** $<10\bar{1}0>$ ***and*** $<11\bar{2}0>$ ***axis, active twin variants are influenced by constraining of the*** $(11\bar{2}0)$ ***and*** $(10\bar{1}0)$

planes, respectively, leading to the modified deformation behavior when comparing to the uniaxial compression test. The deformation curves for channel-die compression tests are similar to those presented by Kelley and Hosford [35]. As for the uniaxial compression, the strain hardening rate in the stage I is higher during compression along the $<11\bar{2}0>$ axis than along the $<10\bar{1}0>$ axis. It was shown in [69, 70] that the early stage of deformation during channel-die compression along the $<10\bar{1}0>$ and $<11\bar{2}0>$ axis was characterized by large scale $\{10\bar{1}2\}$ extension twinning converting the whole specimen into softer orientation for slip.

The texture intensity peak, which corresponds to the initial orientation, was slightly rotated around the compression axis during loading along the $<10\bar{1}0>$ axis (Fig. 5.1.5a,b). This behavior could be explained by dislocation slip in single crystals regions, which were not twinned till the end of the test [70].

The texture components formed during loading in both orientations are a result of extension twinning. The asymmetrical character of texture components originated from twins could be related to dislocation gliding in reoriented material [70].

An illustration of active twinning systems, which is based on the results of texture measurements after channel-die compression of the Mg single crystal, is presented in Fig. 5.1.6.

For the specimen compressed along the $<10\bar{1}0>$ axis, twin variants with *m* of 0.15 are depicted as the twin A and B and the twin variant with *m* of 0.5 is shown as the twin C. The small component in the texture, marked as zone 1 in Fig. 5.1.5b, results from the activation of the twin C, which, however, is not preferred due to the configuration of the test. It can be therefore assumed that twins have a tendency to re-twin into orientation for easy material flow (detail in the Fig. 5.1.6a). Consequently, a small texture component, marked as zone 2 in Fig. 5.1.5b, could be associated with a double twin (tw. C-C in Fig. 5.1.6a) from the twin C. The situation is more transparent for the specimen compressed along the $<11\bar{2}0>$ axis and extension twin variants with *m* of 0.35 are schematically depicted in Fig. 5.1.6b as the twins A and B, respectively. Their texture components result in two symmetrical texture components (0, 30, 30) and (180, 30, 30) (Fig. 5.1.5d), as was written above.

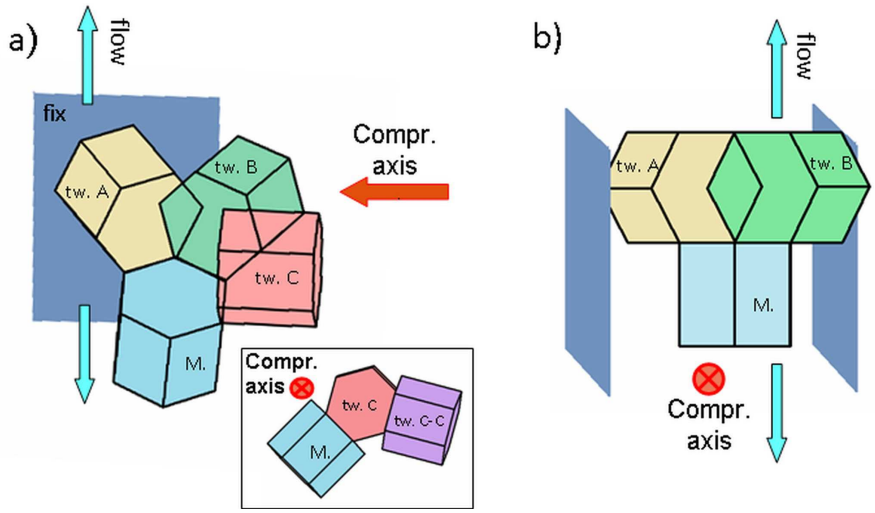

Fig. 5.1.6. Illustration of active twinning system in the Mg single crystal during channel-die compression along the $<10\bar{1}0>$ (a) and $<11\bar{2}0>$ (b) axis. In the detail of (a), double twinning of the original lattice (Matrix=M.) is presented.

The AE response during compression along the $<11\bar{2}0>$ axis is higher than along the $<10\bar{1}0>$ axis. It is ascribed to a higher twinning activity (Fig. 5.1.4), similarly to the uniaxial compression test. This shows that the four variants of extension twins with *m* of 0.35 have higher influence on plastic deformation during channel-die test than the two variants with higher *m* (0.5). These conclusions are corroborated by numerical simulations done in conjunction with studies of mechanical properties of Mg crystals [8, 64].

During compression along the $<10\bar{1}0>$ axis the peak amplitudes of AE events at the stage I of the deformation curve are higher for the channel-die compression than for the uniaxial test (Figs. 5.1.2a and 5.1.4a). According to [91], this fact could be attributed to a high rate of the twin nucleation in the former case. Therefore, it can be concluded that the constraining of the $(11\bar{2}0)$ planes restricts the growth of extension twins and the extension along the *c*-axis is accommodated mainly by increasing number of nucleated twins rather than by their growth.

Similar to the uniaxial compression, the activation of non-basal slip systems during the channel-die compression is associated with a strong decrease in the AE activity due to a fast immobilization of dislocations.

5.2. Extruded Al-Zn- and Zn-Rare earth-based Mg alloys

This part of the thesis is aiming at understanding of the twining-detwinning mechanism in Mg extrusions with respect to the type of microstructure, particularly an average grain size and homogeneity. Therefore, pre-compression followed by tensile loading — that is, one-cycle test — was performed on two extruded materials with different microstructure: AZ31 with bimodal microstructure and ZE10 with homogenous microstructure, Fig. 4.1.2. Both extruded profiles exhibit a prismatic fiber texture (Fig. 5.2.1) with the highest intensity at the $<10\bar{1}0>$ pole in the case of AZ31 and a distribution of intensities along the arc between the $<10\bar{1}0>$- and $<11\bar{2}0>$-poles in the case of ZE10.

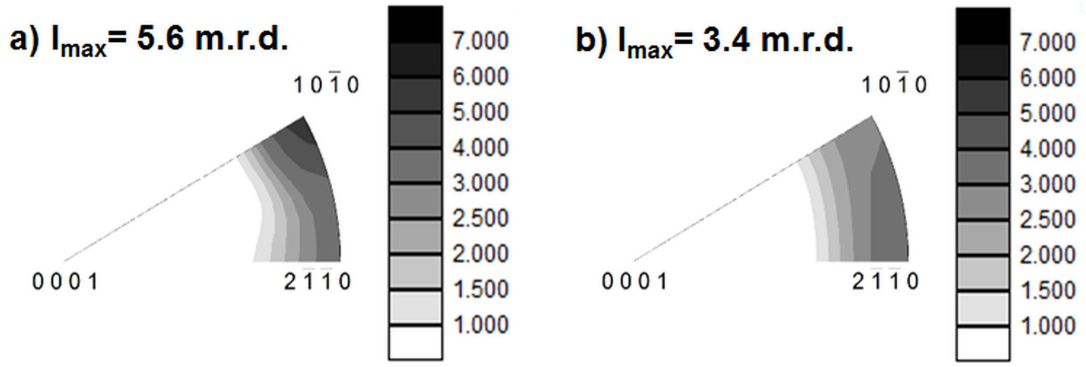

Fig. 5.2.1. Inverse pole figures of AZ31 (a) and ZE10 (b) in the as-received condition. (ED is perpendicular to the inverse pole figures)

A characteristic feature of these textures is a distinct alignment of basal planes parallel to the ED — that is, the *c*-axis is perpendicular to the ED. As was mentioned in Chapter 2 such texture is favorable for the activation of $\{10\bar{1}2\}<10\bar{1}1>$ extension twinning during compression along ED. Consequently, such materials are a good choice for investigation twinning – detwinning mechanism during cyclic loading of textured materials.

5.2.1. Experimental results: effect of pre-compression on subsequent tensile deformation

In general, twins induced by pre-deformation play an important role in the further deformation behavior of the investigated material. To study an influence of the pre-loading level on subsequent tensile test, the samples of AZ31 were firstly pre-compressed up to the stress of 130 MPa, 150 MPa, and 200 MPa, respectively, and then subjected to tensile loading up to fracture. Results of these tensile parts of the tests are shown in Fig. 5.2.2. It can be seen that the higher is the compressive stress the more pronounced is the sigmoidal shape (S-shape) of the tensile curve.

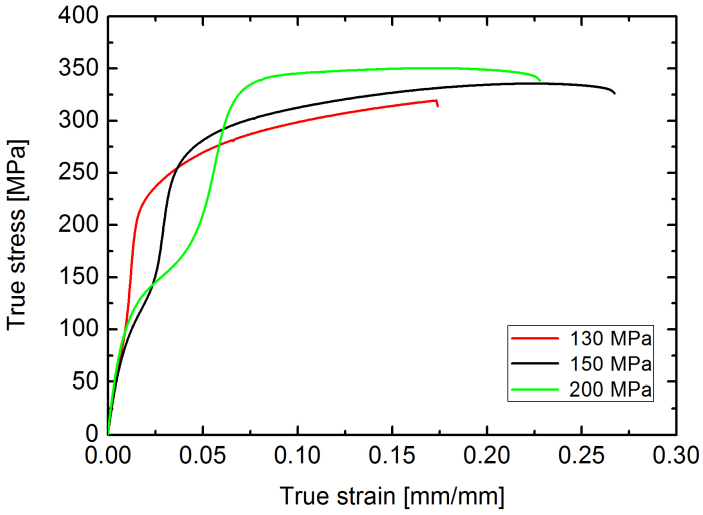

Fig. 5.2.2. True stress *vs.* true strain (a) curves for the tensile loading of pre-compressed AZ31 Mg alloy.

In order to investigate the twinning-detwinning mechanism, mobile twin boundaries are desired and therefore a microstructure with partially twinned grains is preferred. From the characteristic S-shape of the deformation curve for tested AZ31 it could be suggested that the pre-compression up to 150 MPa can provide a microstructure partly induced by twins. Moreover, it was shown in [55] that the microstructure of AZ31 after pre-compression up to 150 MPa is characterized by existence of extension twins. That is why samples pre-compressed to 150 MPa for both AZ31 and ZE10 alloys were used for a detailed analysis during subsequent tension test. To find the link between the particular deformation stages and the AE response, the stress, concurrently measured AE signal voltage (Figs. 5.2.3a and 5.2.4a) and AE count rates (Figs. 5.2.3c–d and 5.2.4c–d) are plotted as a function of time.

It can be seen that yielding occurs at a compressive stress of (124 ± 1) MPa for AZ31 and (81 ± 1) MPa for ZE10. The plastic flow continues with an increasing slope of the deformation curve. After the pre-compression and unloading, the tensile curves have a characteristic S-shaped form for both alloys.

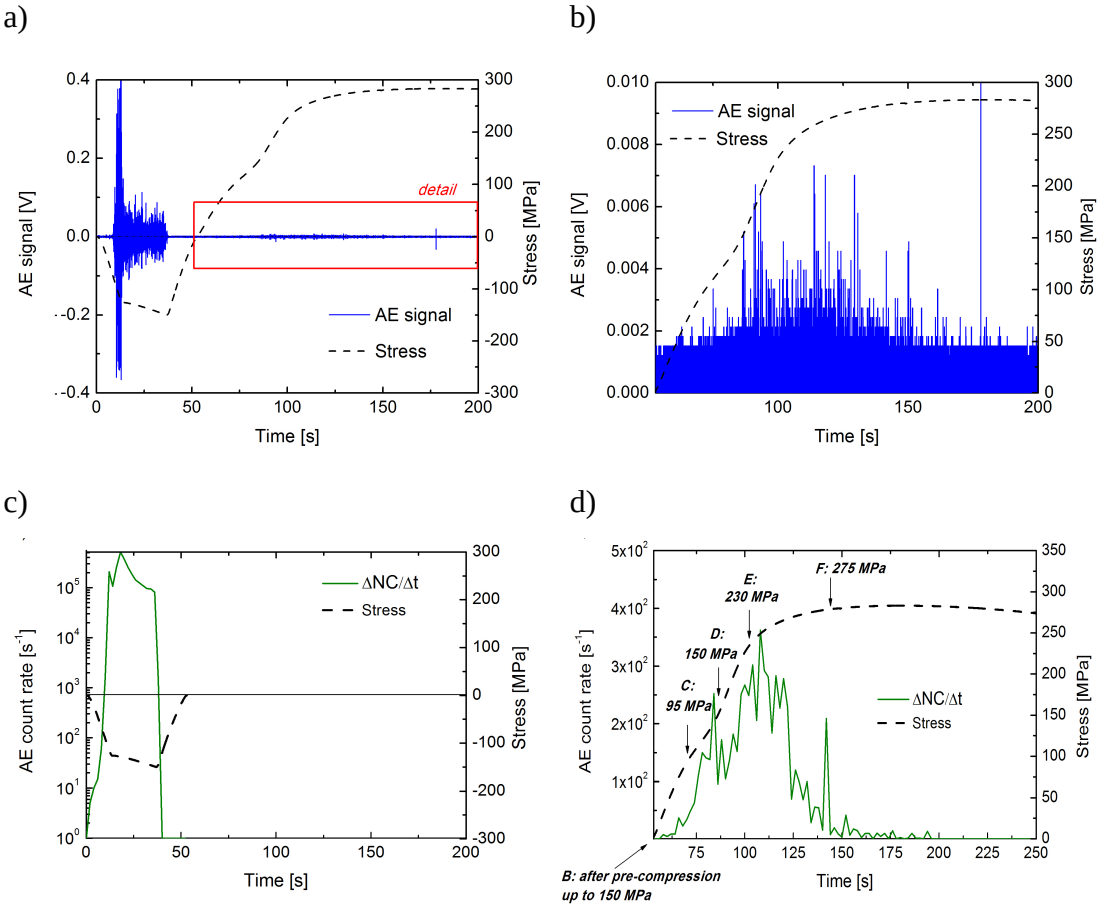

Fig. 5.2.3. AE response during loading of AZ31: stress, AE signal voltage *vs.* time (a) and its detail (b); AE count rate *vs.* time curves during pre-compression (c) and tension (d).

The AE signal (Figs. 5.2.3a and 5.2.4a) is very intensive during pre-compression, especially in the vicinity of the compressive yield strength (CYS). Large amplitude AE events are prominent in this region. In contrast, smaller AE amplitudes were recorded during tensile loading. It is noteworthy that the AE signal amplitudes are significantly higher during the entire test for ZE10 than for AZ31. This is particularly significant during the tensile part; see the details in Figs. 5.2.3b and 5.2.4b.

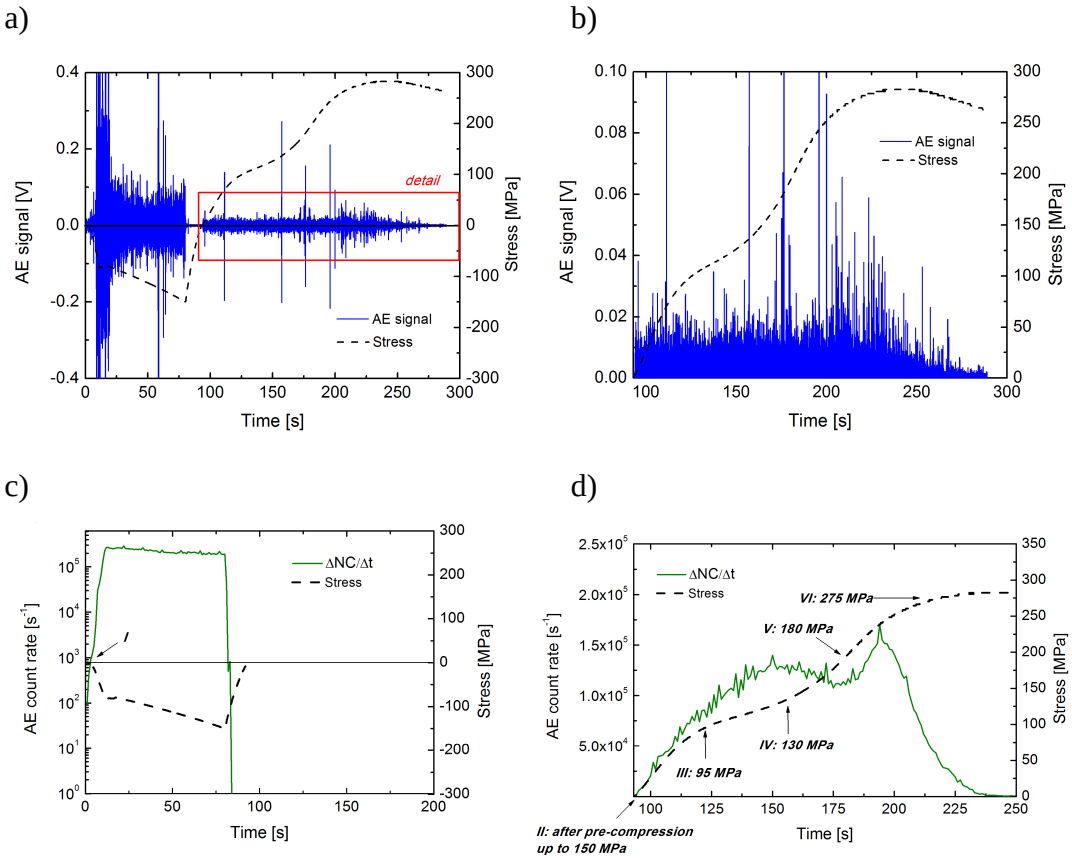

Fig. 5.2.4. AE response during loading of ZE10: stress, AE signal voltage *vs.* time (a) and its detail (b); AE count rate *vs.* time curves during pre-compression (c) and tension (d). Note that the scale of the AE signal is 10 times higher in Fig. 5.2.4b than in Fig. 5.2.3b to reveal the shape of the AE response clearly.

The AE count rate *vs.* the time curve for the compression part of the test (Figs. 5.2.3c and 5.2.4c) exhibits a maximum at the CYS. The subsequent unloading from 150 MPa to zero stress does not produce any detectable AE.

During the reverse (tensile) loading of AZ31, the AE count rate exhibits distinct changes, revealing three maxima with increasing strain (Fig. 5.2.3b). In the case of ZE10, two significant maxima in the AE count rate are observed (Fig. 5.2.4b). Both alloys are characterized by a strong decrease in the AE count rate at the terminal stage of the deformation test. Changes in the AE activity could be related to the inflection points on the deformation curve for both Mg alloys.

5.2.2. Experimental results: microstructure evolution

Characterization of AZ31 with bimodal microstructure

To study the twinning-detwinning activity using EBSD analysis, samples were pre-compressed up to 150 MPa and subsequently loaded in tension up to specific stress levels; these stresses were chosen according to the changes in the shape of the deformation curve and the AE activity (Fig. 5.2.3d). The microstructure of samples in the initial state, after only pre-compression, after pre-compression and tension up to 95 MPa, 150 MPa, 230 MPa, and 275 MPa, denoted in Fig. 5.2.3c-d as A, B, C, D, E and F, respectively, is presented in Fig. 5.2.5.

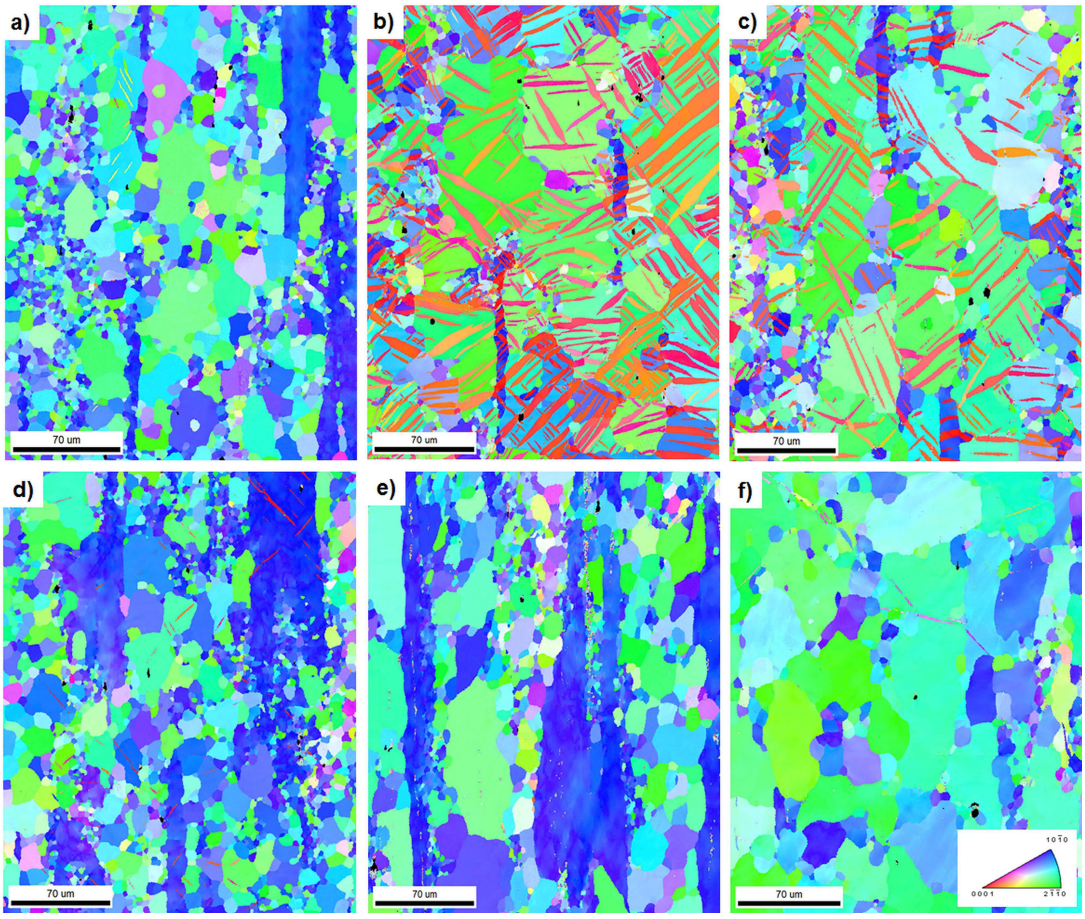

Fig. 5.2.5. Orientation map of AZ31 (ED is vertical): initial state (a), after pre-compression up to 150 MPa (b) and subsequent tension up to 95 MPa (c), 150 MPa (d), 230 MPa (e), and 275 MPa (f) (samples A–F in Fig. 5.2.3c-d, respectively).

The analysis of the misorientation angle distribution of the EBSD map of the sample after pre-compression (Fig. 5.2.5b) confirms the presence of $\{10\bar{1}2\}<10\bar{1}1>$ extension twins with a misorientation angle of 86.3° around

the $<11\bar{2}0>$ axis. During reverse tensile loading, the extension twins become thinner. The microstructure development can be tracked in Fig. 5.2.5c–e, taken from samples C through E. Sample E (Fig. 5.2.5e) shows a twin-free microstructure; therefore, reverse tensile loading up to 230 MPa seems to be sufficient to complete the detwinning process. Microstructure of sample F subjected to higher reverse tensile loading (275 MPa) exhibits existence of compression twins with a misorientation angle of 56° around the $<11\bar{2}0>$ axis (Fig.5.2.5f).

The evolution of the crystallographic texture during the test evaluated from EBSD measurements is illustrated in Fig. 5.2.6. After pre-compression along ED, the main intensity of the basal planes is observed in ED, Fig. 5.2.6b. During the subsequent tension along ED, its intensity decreases, as is obvious in Fig. 5.2.6b–d. At the terminal stage of tensile loading, a strong, prismatic fiber texture similar to that of the initial state of the material is observed (Figs. 5.2.6a and f).

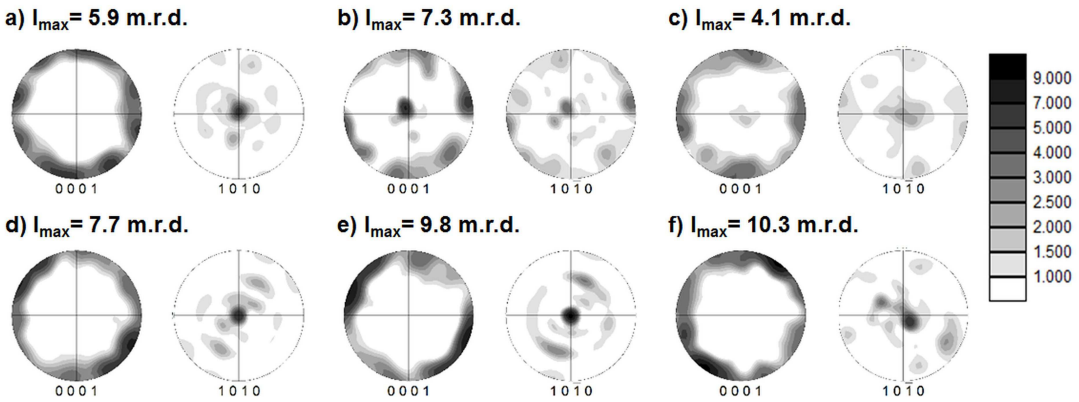

Fig. 5.2.6. Crystallographic texture of AZ31 round bar (ED is perpendicular to pole figures) in the initial state (a) and at various deformation stages: after compression up to 150 MPa (b) and subsequent tension up to 95 MPa (c), 150 MPa (d), 230 MPa (e), and 275 MPa (f).

Fig. 5.2.7 shows the microstructure of the pre-compressed AZ31. The grains without twin boundaries are marked in green, and the boundaries of the $\{10\bar{1}2\}<10\bar{1}1>$ extension twins are marked in red. It can be observed that smaller grains are mostly free of twins, whereas larger grains contain twins.

The textures of these two fractions of the microstructure are plotted in Fig. 5.2.7b for small grains without twins and Fig. 5.2.7c for larger grains containing twins. The latter fraction exhibits a texture with two distinct components — one

around the $<0001>$ pole, related to the orientation of twins, and the other clearly concentrated around the prismatic poles, related to the orientation of parent grains. In the case of the smaller grains, the texture is comparable with the initial texture, perhaps with a slightly more distinct component in the $<10\bar{1}0>$ pole. Nevertheless, both fractions of grains have orientations similar to the basal planes parallel to ED; hence, a relatively larger effect of grain size than effect of texture on the activity of twins is expected.

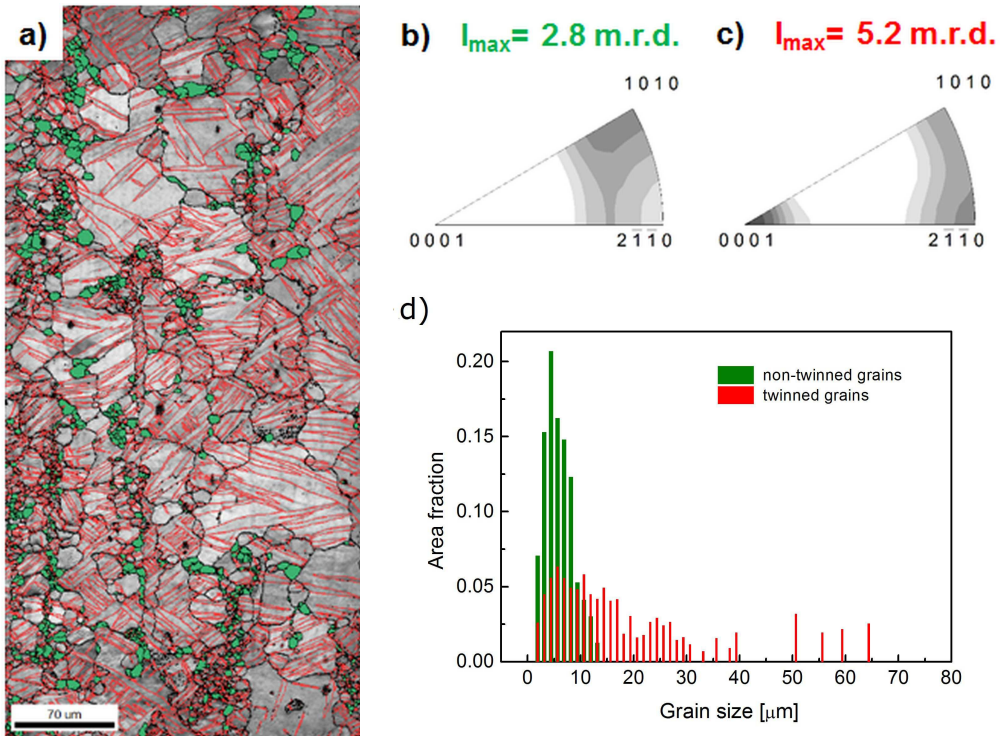

Fig. 5.2.7. Image quality map (a) of AZ31 (ED is vertical) after pre-compression up to 150 MPa; texture of grains without twins (green) (b) and grains with $\{10\bar{1}2\}<10\bar{1}1>$ extension twins (boundaries are marked in red) (c) and their grain size distributions (d).

The detail inspection of twinned grains reveals:

- the activation of different variants of extension twins.
- in some grains, there are two groups of twins with a misorientation angle of 6° between them. As an example, a detailed view of the orientation map of the microstructure of sample C is presented in Fig. 5.2.8.

- pre-existing twins can provoke twin nucleation in the neighboring grains, and, consequently, twins become connected at the grain boundaries, Fig. 5.2.8.
- no compression twins are found at the early stages of tensile loading. Only after the shrinkage of extension twins do new twins (Fig. 5.2.5f), particularly compression twins, begin to nucleate and grow. A better overview of compression twins is given in Fig. 5.2.9.

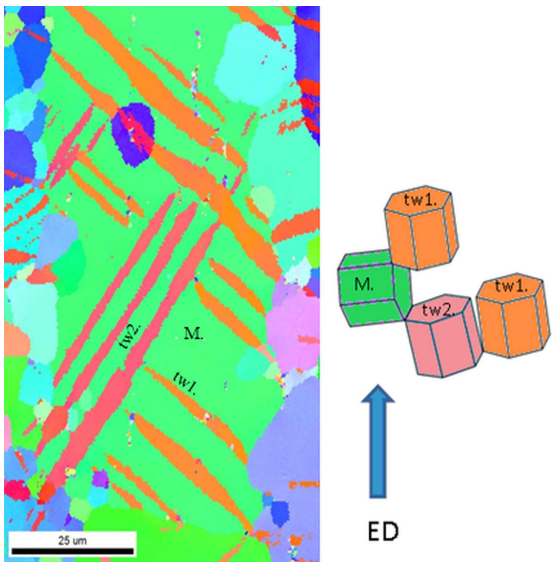

Fig. 5.2.8. Detailed orientation map for AZ31 sample C and illustration of the activated extension twin variants. The parent orientation is marked as "M." = "Matrix"; extension twin variants are denoted as "tw1(2)" (misorientation angle of 86.3°).

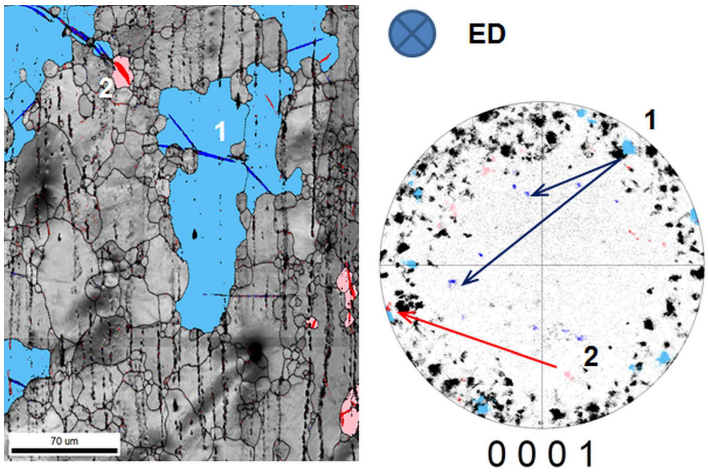

Fig. 5.2.9. Image quality map and pole figure for sample F shows the presence of compression twins (blue) and their orientation relative to orientation of parent grains (light blue).

The same test concept was applied to the ZE10 Mg alloy with a homogeneous microstructure. Fig. 5.2.10 shows the area fractions of twins for both alloys. After pre-compression, the twin area fraction for ZE10 is larger than that for AZ31, and during reverse loading, it is reduced similarly in both alloys.

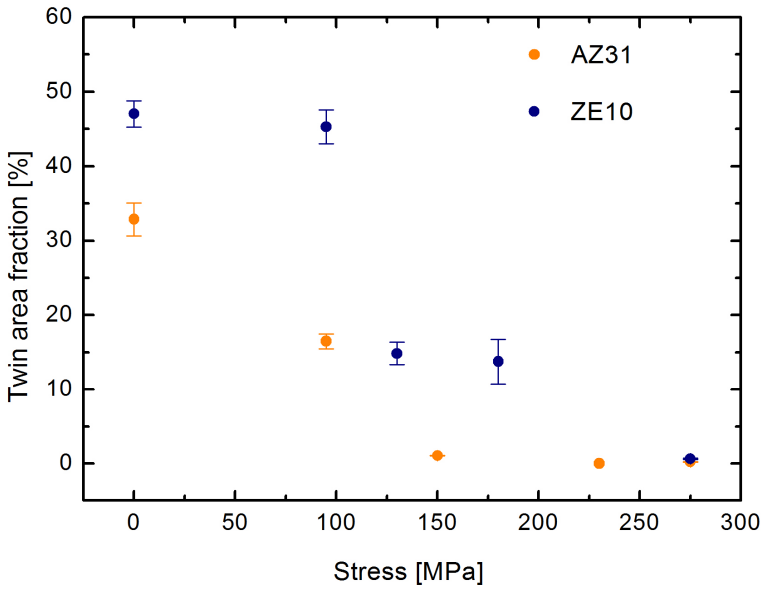

Fig. 5.2.10. Dependences of the twin area fractions on applied reverse loading stress (tensile part).

Characterization of ZE10 with homogeneous microstructure

The orientation maps of the microstructure of ZE10 in the initial state and after pre-compression (sample I and II in Fig. 5.2.4c-d) are depicted in Fig. 5.2.11a and b, respectively. The microstructure of sample II contains many $\{10\bar{1}2\}<10\bar{1}1>$ extension twins giving a high twin area fraction (47%) of the analyzed area. A small number of grains is completely twinned as shown in Fig. 5.2.12, and contrary to AZ31, no grains are twin-free. The orientation maps for the samples that were subsequently loaded in tension up to 95 MPa, 130 MPa, 180 MPa, and 275 MPa (denoted as samples III, IV, V and VI in Fig. 5.2.4d, respectively) are presented in Fig. 5.2.11c–f.

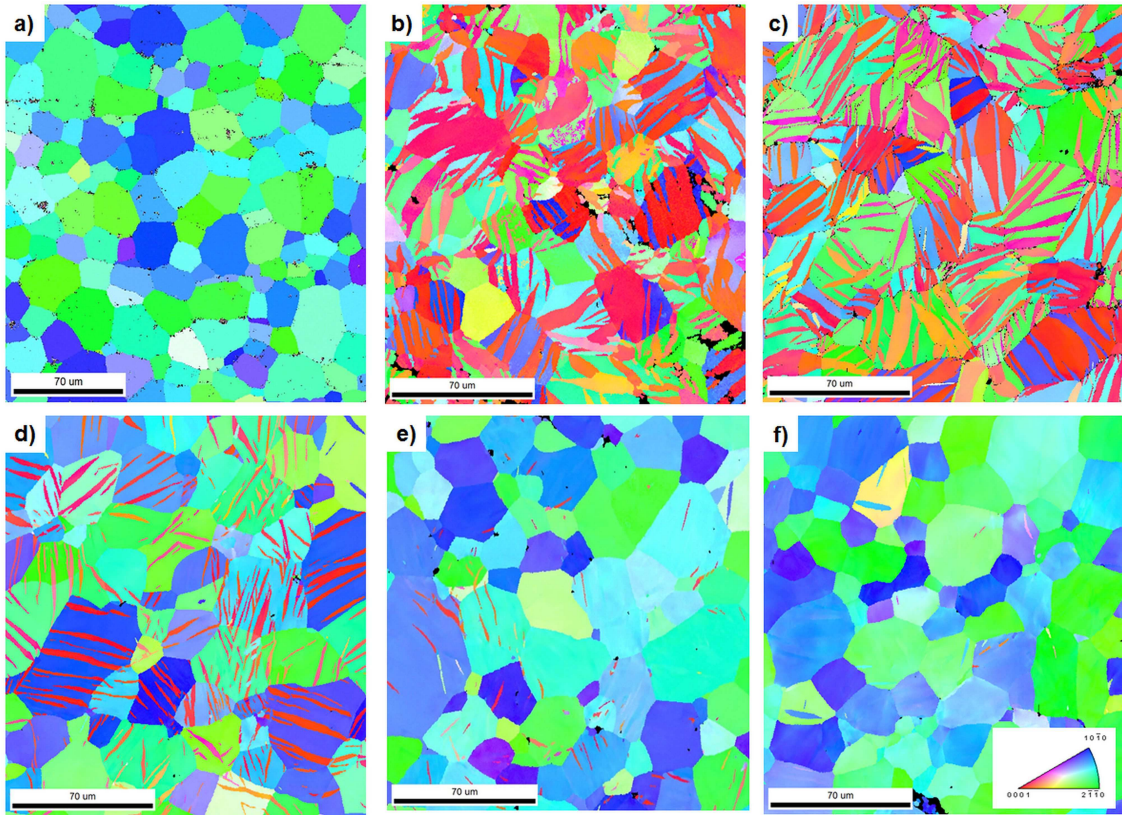

Fig. 5.2.11. Orientation map of ZE10 (ED is perpendicular to the map) in the initial state (a) and after pre-compression up to 150 MPa (b) followed by tension up to 95 MPa (c), 130 MPa (d), 180 MPa (e), and 275 MPa (f) (samples I–VI in Fig. 5.2.4c-d, respectively).

The twins become thinner than those in sample II during tensile loading up to 95 MPa, cf. Fig. 5.2.11b-c. The detwinning process continues with increasing tensile stress (Figs. 5.2.10 and 5.2.11c-e). A small number of extension twins is still observed in sample V. After increasing the tensile stress to 275 MPa (sample VI), the detwinning process seems to be complete, and new twins are nucleated. Similar to AZ31, the nucleation of compression twins takes place only after the complete detwinning of extension twins. The orientation map and corresponding illustration of parent grains and compression twins are shown in Fig. 5.2.13b–c. For sample VI, some twins are of the $\{10\bar{1}2\}<10\bar{1}1>$ extension type. Nevertheless, different colors indicate that different twin variants operate from those observed during pre-compression (Fig. 5.2.13a and b).

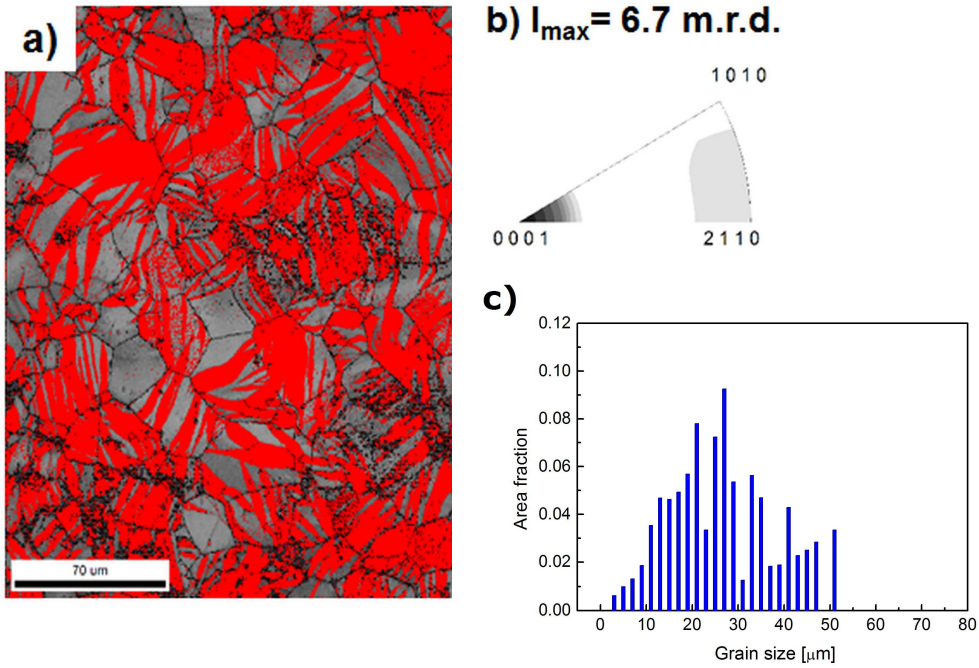

Fig. 5.2.12. Image quality map (a) of ZE10 (ED is perpendicular to the map) after pre-compression up to 150 MPa; texture (b) and grain size distribution (c).

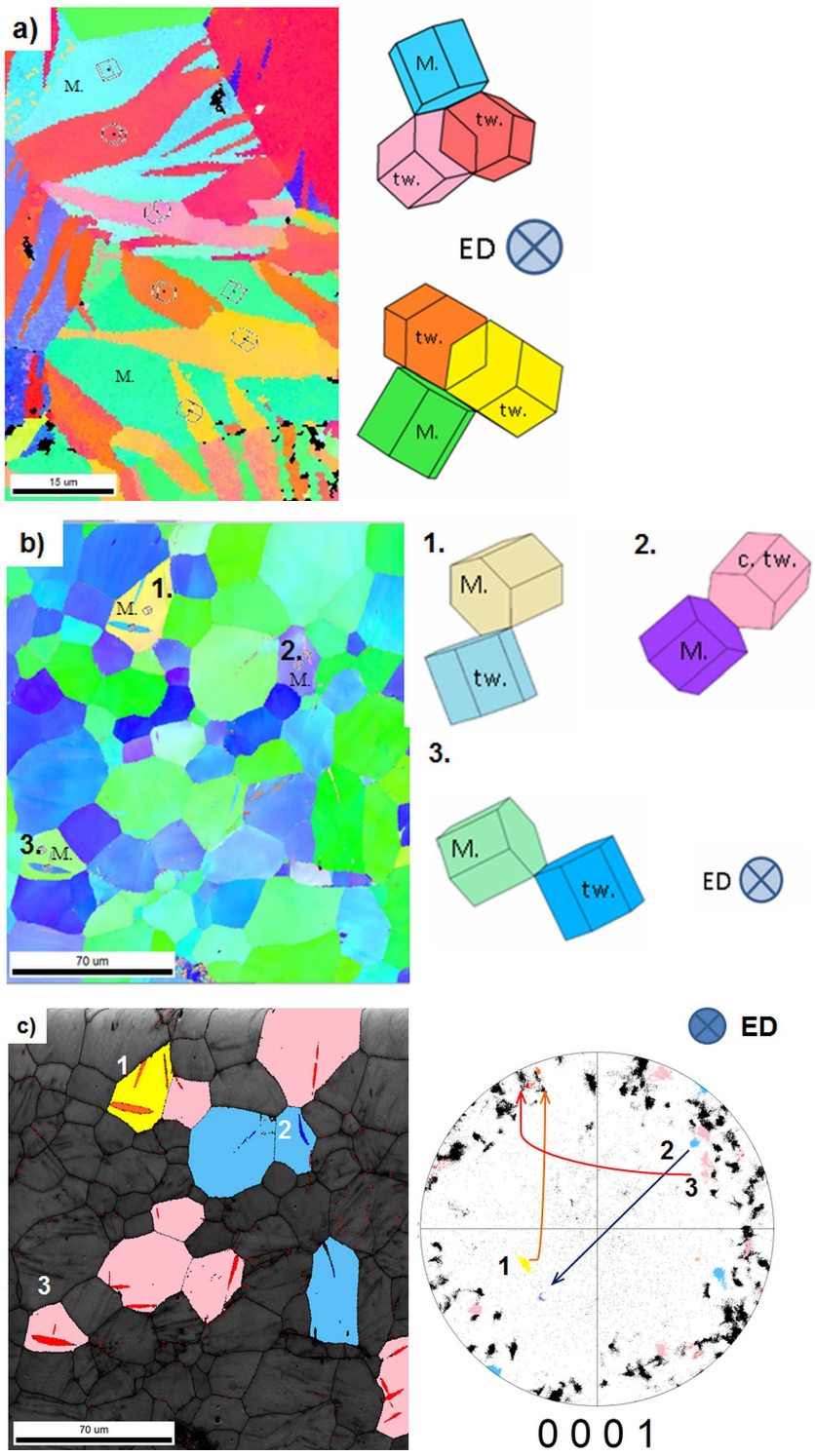

Fig. 5.2.13. ZE10: orientation map and illustration of activated twin variants for samples II (a) and VI (b). The parent orientation is marked as “M.” = matrix; extension twins are denoted as “tw.” (misorientation angle of 86.3°), and compression twins are denoted as “c.tw.” (misorientation angle of 56°). (c) Image quality map and pole figure for the sample VI (ZE10). Extension twins are marked in red; compression twins are marked in blue.

The evolution of the crystallographic texture of ZE10 during pre-compression and the subsequent tension is shown in Fig. 5.2.14. During pre-compression along ED, basal planes change orientation to ED due to extension twinning. Thus, a strong texture component appears in ED (Fig. 5.2.14b). During subsequent tensile loading, the intensity of this main peak decreases, as shown in Fig. 5.2.14c–e. At the terminal stage of tensile loading, the texture has a prismatic fiber character and is similar to that of the initial state of the material (Fig. 5.2.14a and f).

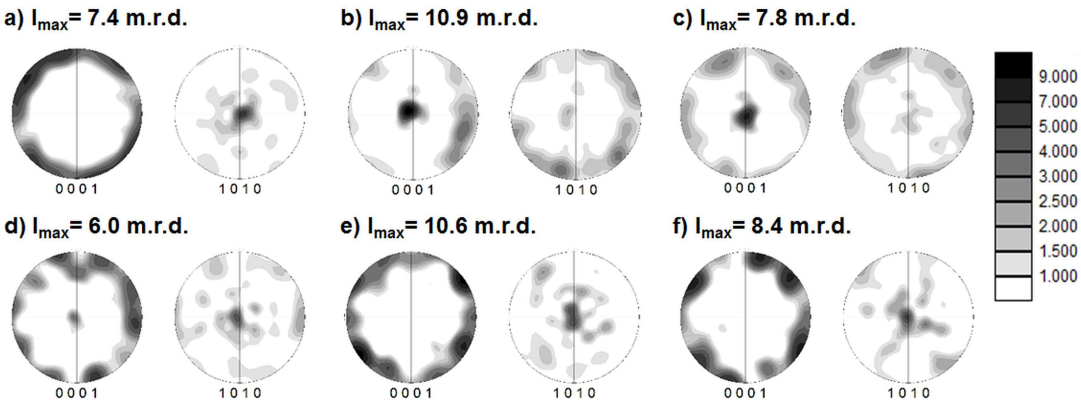

Fig. 5.2.14. Crystallographic texture of ZE10 (ED is perpendicular to the pole figures) in the initial state (a) and at various deformation stages: after compression up to 150 MPa (b) and subsequent tension up to 95 MPa (c), 130 MPa (d), 180 MPa (e), and 275 MPa (f).

As mentioned above, during pre-compression, extension twins reorient basal planes from the initial orientation, parallel to ED, into an orientation perpendicular to ED. At the terminal stage of tensile deformation (275 MPa, sample VI), the newly nucleated extension twins reorient the original lattice (marked in yellow in Fig. 5.2.13c) by 86.3° around ED; that is, basal planes of the twinned fraction (marked in red) remain oriented mainly parallel to ED. A schematic illustration of twin variants in specific grains is presented in Fig. 5.2.13b.

It should be noted that the orientations of the c-axes of some grains are close to ED (such as grain 1 in Fig. 5.2.13b–c). This is inconsistent with the original texture of ZE10 before pre-compression; in the original texture, the *c*-axis orientations of the grains are perpendicular to ED. Therefore, these grains are assumed to be already fully reoriented as a result of twinning during pre-compression.

5.2.3. Discussion: twinning – detwinning mechanism in extruded Mg alloys

General findings for AZ31 and ZE10 alloys during one-cyclic test

The AE signals appear even before reaching YS (Figs. 5.2.3a and 5.2.4a), suggesting the beginning of dislocation glide before yielding. This was also observed in previous works [80, 92]. The twin nucleation was found as the main deformation mechanism at the macroscopic yield, and it significantly influences the yield strength. Thus, the observed low CYS and a strong AE signal are unequivocal signs of the activity of this mechanism.

Investigations conducted in [83, 91, 93] demonstrated that the twin nucleation is an excellent source of AE, contrary to the twin growth, which does not contribute to the AE response. Other combined studies, provided by the EBSD technique and light microscopy [94], AE with digital image correlation [95], and AE with neutron diffraction [74], have also shown that $\{10\bar{1}2\}<10\bar{1}1>$ twins nucleate at the beginning of plastic deformation.

The misorientation analysis of the EBSD maps reveals the activation of $\{10\bar{1}2\}<10\bar{1}1>$ extension twins in both alloys during pre-compression (Figs. 5.2.5b, 5.2.11b). The extension twin activity can be also observed in the texture development, during which a strong peak appears in the ED of the (0001) pole figure; this can be seen for pre-compressed samples B and II for AZ31 and ZE10, respectively, and is not visible in the as-received condition (Figs. 5.2.6 and 5.2.14).

The AE signal, observed shortly after the YS, has significantly lower amplitudes. This decrease in the AE signal amplitudes indicates a change in the dominant deformation mechanism, and it is connected with the transition from the twin nucleation to dislocation glide and twin growth. Nevertheless, a few twins could still nucleate during the increase of the compression load.

Unloading from the compressive stress of 150 MPa (Figs. 5.2.3–5.2.4) to zero stress does not produce any detectable AE signals, which corresponds to the closing of dislocation sources. Furthermore, twin thinning may be an active relaxation mechanism during unloading. Similar to the growth or thickening of twins, detwinning or thinning is basically a movement of twin boundaries, so no detectable AE signal [91, 96] is expected as a result of this mechanism.

According to Christian and Mahajan [17], a higher stress is required for nucleation than for the propagation of twins. Therefore, during reverse loading, detwinning is easily activated owing to the already existing twin boundaries. Based on this, the lower YS for the reverse tension than that for the pre-compression could be explained (Figs. 5.2.3a, 5.2.4a).

Unlike the usual shape of the tensile curve, after pre-compression, the deformation curve for the tensile part is very similar to the compression part of the curve and has a sigmoidal shape, including an inflection point. Twinning and detwinning, owing to their strong polar nature, result in large reorientations of the crystal lattice (86.3°), which macroscopically gives rise to the characteristic "S-type" stress–strain behavior in polycrystalline materials. A similar behavior was observed during cyclic testing in the textured AZ31 sheet [23].

The subsequent tensile loading reopens dislocation sources, and collective dislocation motion produces detectable AE signals. Consistently, with increasing tensile load, the AE count rates also increase until reaching a certain level of stress (Figs. 5.2.3d and 5.2.4d). The upcoming decrease in the AE count rates is connected with a decrease in the free path of the moving dislocation owing to an increase in the dislocation density resulting in the strain hardening of the material [97, 98].

For both alloys, the AE response during the entire tensile loading is significantly lower than during pre-compression. Basically, two opposite processes influence the AE activity during tensile loading. Namely, the increasing number of detwinned grains supports the AE activity through the rise in the flight distance and the free length of moving dislocations. However, the increasing dislocation density implies a stronger barrier for their movement and therefore generally reduces the AE signal voltage and the AE count rate in the tensile part of the test.

Microstructure and texture effects on the deformation behavior

Despite similar general findings for both alloys, certain distinct differences in the deformation behavior of the alloys are observed and are described in the following paragraph.

The significantly higher AE signal in the case of ZE10 compared with that of AZ31 (Figs. 5.2.3a–b and 5.2.4a-b) can be explained by the differences in the microstructures. ZE10 is characterized by homogeneous microstructure and an average grain size of 26 µm, whereas AZ31 has a bimodal microstructure and

an average grain size of 20 µm. Thus ZE10 has a lower number of grain boundaries as potential obstacles for the dislocation movement in comparison to AZ31. Similar results were found by previous studies [99, 100], in which it was reported that a larger grain size results in a stronger AE response.

In the case of pre-compressed AZ31, it was observed that smaller grains do not twin (cf. Fig. 5.2.7). It is mentioned above that there is no distinct difference between the textures of the twin-free grains and the original orientations of twinned grains. In the case of pre-compressed ZE10, all grains contain twins, which is likely a result of a homogeneous microstructure and grains with larger average grain size than in AZ31. In fact, non-twinned grains, which were observed in AZ31, are essentially not found because of the absence of the fraction of small grains in the microstructure of ZE10. In addition, some grains show numerous twins in both alloys, and different extension twin variants are clearly visible. The larger twinned area fraction and higher AE activities around the compressive yield strength in ZE10 indicate higher twinning activity than in AZ31. This is also consistent with lower CYS in ZE10 compared with AZ31. In conclusion, there is a grain size dependence of twin nucleation, indicating that a higher number of twins will nucleate for larger grain sizes. This result is specifically related to the grain size; no texture effect is revealed (Fig. 5.2.7).

The difference in the texture, in the context of the difference in grain orientation, could result in differences in the activation of twin variants during plastic deformation. Despite a similar initial texture of AZ31 and ZE10, the EBSD analysis of both alloys shows that different variants of twins are activated independently of the initial orientation of the grains. In previous works [80, 101, 102] the Schmid factor calculations have been used to study the probability of the activation of specific extension twin variants, with respect to the loading axis.

From the six possible twin variants [80], two activated from different “sides” of the hcp cell form two groups of twins in large grains. This is especially visible in the elongated grains of AZ31; see the illustration in Fig. 5.2.8. A misorientation angle of 6° between two groups of twins is explained by the characteristic angle of 86.3° for extension twins. Such groups are observed in grains with different orientations with the *c*-axis oriented along $<10\bar{1}0>$ and along $<11\bar{2}0>$; hence, no texture effect is revealed for either alloy.

During ***reverse loading after pre-compression,*** the detwinning process proceeds similarly in both alloys and simultaneously in grains with different orientations; thus, no grain size or texture dependencies were revealed. The detwinning progress is observed in both EBSD orientation maps and texture developments. In the case of ZE10, compared with AZ31, a higher level of applied reverse stress is required for detwinning, owing to the large twinned area after pre-compression. In summary, twinning and detwinning processes, in terms of boundary mobility, are not size dependent. In contrast, twin nucleation is size dependent.

The AE count rate peak at the last stage of plastic deformation is related to active dislocation motion and the further nucleation of extension and compression twins. Thin twins are observed in grains with different orientations (Figs. 5.2.5f and 5.2.11f) when the detwinning process seems to be completed. In both alloys, compression and extension twins are observed. Extension twinning in ZE10 occurs in grains with their initial orientation and in grains that were completely twinned during pre-compression. Fully twinned grains become favorably oriented for the nucleation of extension twins during reverse loading, as seen in Fig. 5.2.13b. A detailed analysis of the EBSD maps shows that during reverse loading in grains with the initial orientation extension, twinning rotates the c-axes around ED, whereas during pre-compression, rotation of the c-axes occurs toward ED; see the illustration in Fig. 5.2.13a. This could be explained by the preference in the activation of another twin variant [80] with respect to the loading direction, which can more effectively contribute to strain accommodation of the material.

The activities of compression and extension twins, which occur only after detwinning—that is, at a later stage of deformation—support the idea that the stress required for the nucleation of new twins is higher than the stress required for moving the twin boundaries, [28, 103]. The last AE count rate peak is located specifically in the range of the test with the highest strain hardening rate, i.e. at the inflection point of the stress–strain curve. This AE count rate peak is connected with the nucleation of new twins. In general, compression twins of $\{10\bar{1}1\}$ and $\{30\bar{3}2\}$ types have been observed at large tensile strains in Mg and its alloys [34].

5.3. Rolled Al-Zn- and Zn-Rare earth-based Mg alloys

Various rolling conditions could result in variation of final texture of the sheets. Planar anisotropy of mechanical properties, which is significant for some Mg alloy sheets, is caused by a twinning activity and preferable activation of dislocation slip systems (basal, prismatic, and pyramidal) during loading along a certain direction. To get more information about twinning and reveal its role in mechanical behavior of textured Mg alloys, tensile tests with concurrent AE measurements were performed for rolled Mg alloys. Results and discussion of this study are presented in following paragraph.

The initial textures of the investigated alloys in as rolled state are represented by the distribution of basal (0002) and prismatic $(10\bar{1}0)$ poles (Fig. 5.3.1). The pole figures of AZ31 sheets in both rolling conditions (the conventionally rolled slab and the rolled sheet of TRC strip) display basic basal character of the texture with a significant concentration of basal planes oriented into ND (basal planes are parallel to the sheet plane). The orientation distribution of the basal planes around ND is wider in RD than in TD. The intensity of the basal pole of the rolled AZ31 TRC strip is lower than that of the rolled AZ31.

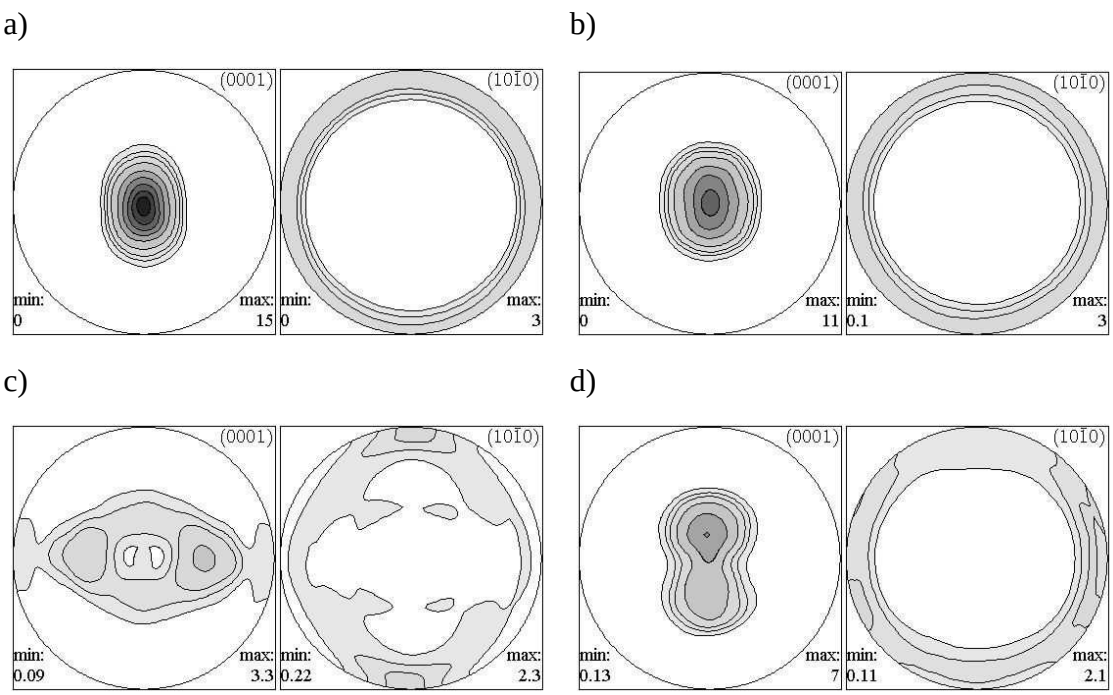

Fig. 5.3.1. Initial texture of Mg alloys (RD↑, TD→, levels: 1.0, 1.5, 2.0, 3.0, 5.0, 7.0, 9.0 m.r.d.): (a) rolled AZ31, (b) rolled AZ31 TRC strip; (c) rolled ZE10; (d) rolled ZE10 TRC strip.

The intensities of the (0002) and $(10\bar{1}0)$ pole figures for Mg alloy with RE alloying elements in both rolling conditions are significantly lower than that for AZ31 Mg alloy. The intensity peak of basal pole figure for the rolled ZE10 is tilted away from the sheet ND toward TD and is split in two peaks (see Fig. 5.3.1c). The pole distribution of the basal planes for rolled ZE10 TRC strip is different from that, which is usually observed in Mg alloys with RE alloying elements [35]. The texture could be defined as a texture with essentially basal character and basal planes are slightly tilted toward RD. The intensity of the basal pole is higher for the rolled ZE10 TRC strip than for the rolled ZE10, and lower than that for the rolled AZ31 TRC strip.

Intensity distribution of $(10\bar{1}0)$ pole figures for both AZ31 sheets is homogeneous in contrast to the ZE10 sheets. In rolled ZE10, the prismatic pole has two peaks toward RD, and in the rolled ZE10 TRC strip the higher intensity of $(10\bar{1}0)$ pole figure is observed toward TD.

5.3.1. Experimental results: mechanical properties

An inspection of the stress-strain curves shows that the rolling conditions have obviously a strong influence on the deformation behavior (Fig. 5.3.2). The shape of the stress-strain curves is typical for the rolled Mg alloys and their characteristic values are presented in Table 5.3.1. It can be seen that for the rolled ZE10 the higher value of YS is observed for the RD sample than that for the TD sample. In case of the rolled ZE10 TRC strip, YS is higher for the TD sample than for the RD sample. In contrast, both rolled AZ31 and rolled AZ31 TRC strip exhibit higher YS for the TD sample than for the RD sample. One should notice that the value of YS for the rolled AZ31 TRC strip is significantly higher than that for the rolled ZE10 TRC strip. For loading along the axis tilted by 45° from RD to TD, the YS values are between the values for RD and TD for all the investigated sheets.

Therefore, all four Mg alloy sheets exhibit a strong planar anisotropy of YS. It is less pronounced for the rolled TRC strips of both Mg alloys than for the conventionally rolled sheets (see Table 5.3.1). For the rolled ZE10 sheet, the planar YS anisotropy is more pronounced than for other sheets and it almost disappears for the rolled AZ31 TRC strip.

a)

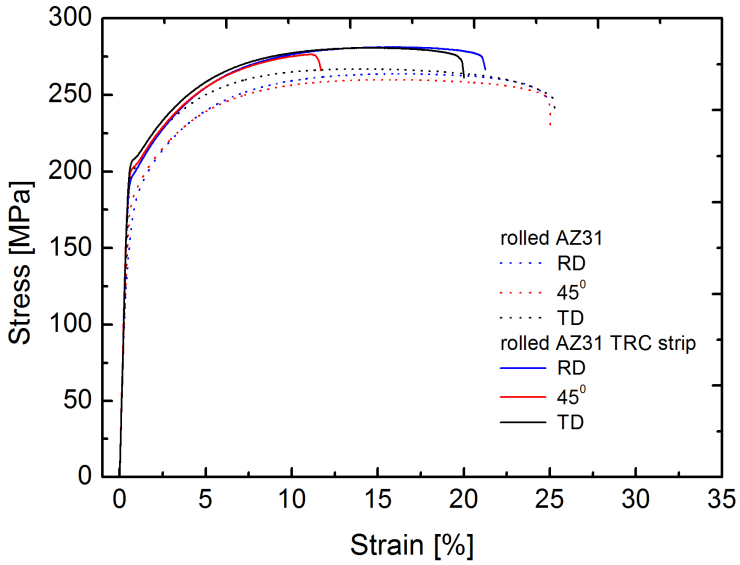

b)

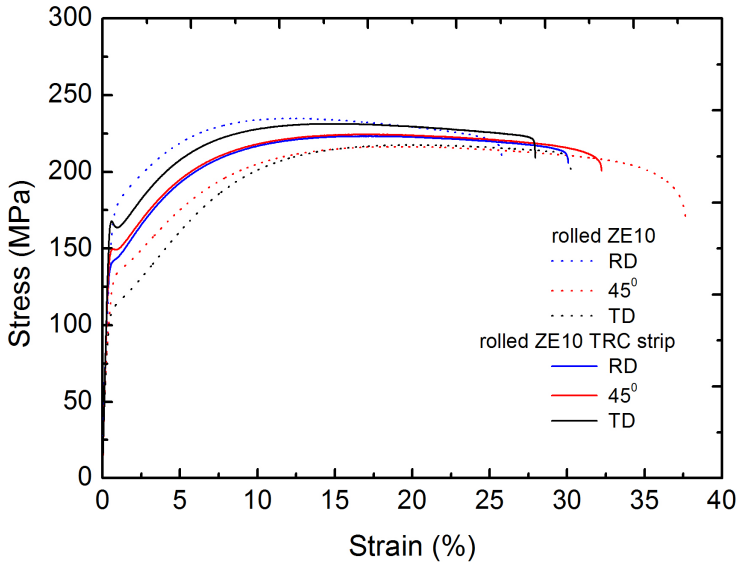

Fig. 5.3.2. Stress *vs.* strain tensile curves for (a) AZ31 and (b) ZE10 sheets.

The significant difference in the AE response is observed during testing the sheets in both rolling conditions. Figs. 5.3.3-5.3.4 show the stress *vs.* time curves with the corresponding AE response for the tensile loading in three directions for the rolled AZ31 and for the rolled AZ31 TRC strip, respectively. The analogous data of tensile tests for ZE10 Mg alloy are presented in Figs. 5.3.5-5.3.6.

The AE count rate exhibits a maximum at the beginning of plastic deformation in all samples, which is followed by a decrease in the AE count rate persisting until the end of the deformation test. Furthermore, in rolled ZE10 during TD loading the AE count rate exhibits two maxima close to macroscopic YS (see Fig. 5.3.5c). In case of loading along the axis tilted by 45° from RD to TD, the second maximum becomes more evident in comparison with the tension along RD.

TABLE 5.3.1

Mechanical properties of rolled Mg alloys: TYS – tensile yield strength, UTS – ultimate tensile strength.

Alloy	Direction of the tensile loading	TYS (MPa)	UTS (MPa)	Uniform elongation (%)	Fracture strain (%)
Rolled AZ31	**RD**	149 (±2)	263 (±1)	15.8 (±0.2)	24.1 (±0.5)
	45°	172 (±1)	260 (±1)	15.2 (±0.1)	24.5 (±0.5)
	TD	196 (±1)	266 (±1)	13.2 (±0.1)	24.6 (±0.5)
Rolled AZ31 TRC strip	**RD**	194 (±1)	281 (±1)	15.3 (±2)	20.5 (±0.5)
	45°	201 (±1)	276 (±1)	10.5 (±1)	11.14 (±0.5)
	TD	205 (±1)	281 (±1)	13.7 (±1)	19.3 (±0.5)
Rolled ZE10	**RD**	172 (±3)	234 (±1)	11.4 (±1)	24.8 (±0.5)
	45°	122 (±3)	217 (±1)	18.4 (±1)	37.1 (±0.5)
	TD	103 (±3)	218 (±1)	19.6 (±2)	29.5 (±1)
Rolled ZE10 TRC strip	**RD**	140 (±1)	223 (±1)	16.8 (±2)	29.5 (±1)
	45°	149 (±3)	225 (±1)	16.8 (±3)	31.7 (±0.5)
	TD	166 (±3)	231 (±1)	14.5 (±3)	27.5 (±1.5)

It is important to note that the difference in the AE activity is observed during straining along various directions of rolled AZ31 (and ZE10) magnesium alloys (see Figs. 5.3.3 – 5.3.4, and 5.3.5 – 5.3.6, respectively). During tensile loading of the AZ31 Mg alloy in RD, the AE activity is higher in conventionally rolled sheets than in the rolled TRC strips. If tensile loading is applied along TD, the AE activity is higher in the rolled AZ31 TRC strip than in rolled AZ31. For Mg alloy with RE alloying elements, the higher AE activity during TD loading is observed in rolled ZE10. For all deformed alloys, the AE activity during loading along the axis tilted by 45° from RD to TD reflects an intermediate behavior between the AE activity during loading along RD and TD.

Moreover, the decrease of the AE count rate after the macroscopic yield strength during RD loading of the rolled ZE10 is rapid, while it is more gradual for the rolled ZE10 TRC strip (Fig. 5.3.5a and 5.3.6a).

a)

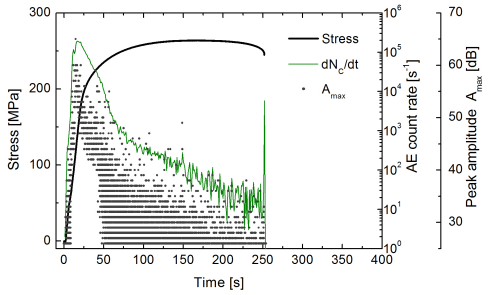

b)

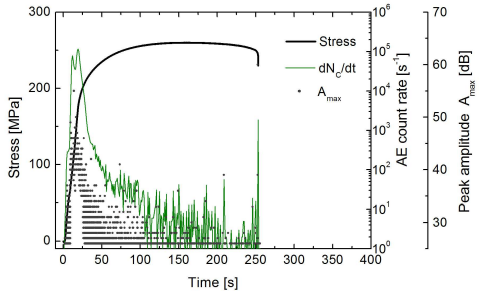

c)

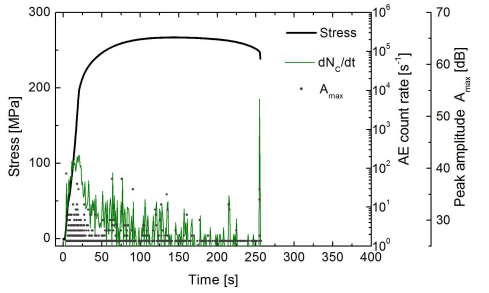

Fig. 5.3.3. Stress *vs.* time curves with the corresponding AE response (AE count rate, peak amplitudes of AE events) of tension of the rolled AZ31 along RD (a), 45° (b), TD (c).

a)

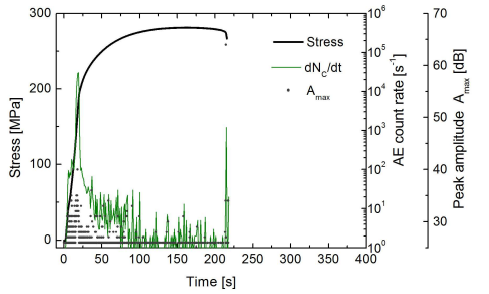

b)

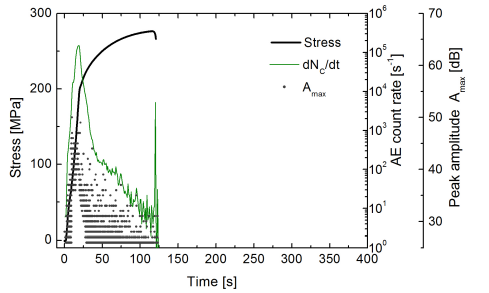

c)

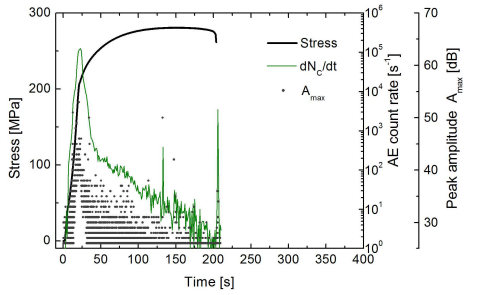

Fig. 5.3.4. Stress *vs.* time curves with the corresponding AE response (AE count rate, peak amplitudes of AE events) of tension of the rolled AZ31 TRC strip along RD (a), 45° (b), TD (c).

a)

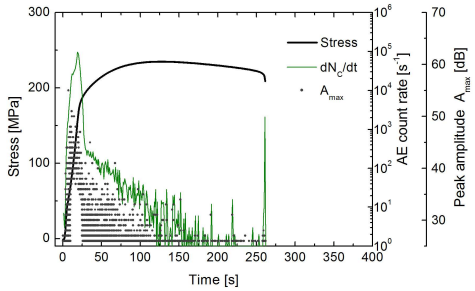

b)

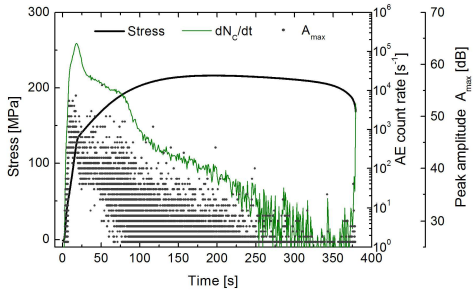

c)

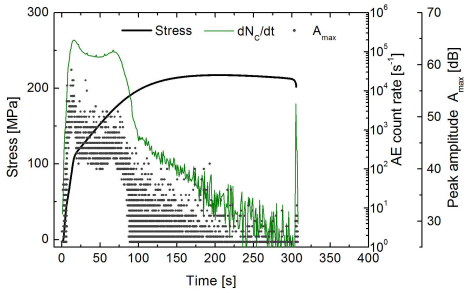

Fig. 5.3.5. Stress *vs.* time curves with the corresponding AE response (AE count rate, peak amplitudes of AE events) of tension of the rolled ZE10 along RD (a), 45° (b), TD (c).

a)

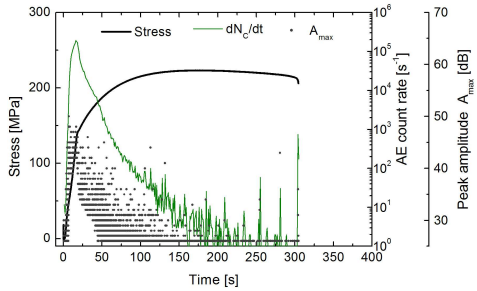

b)

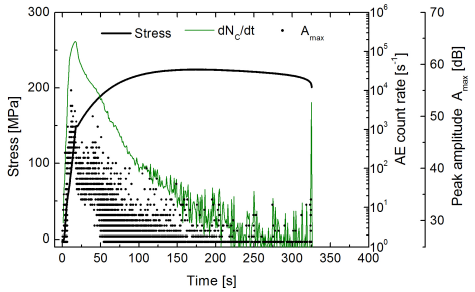

c)

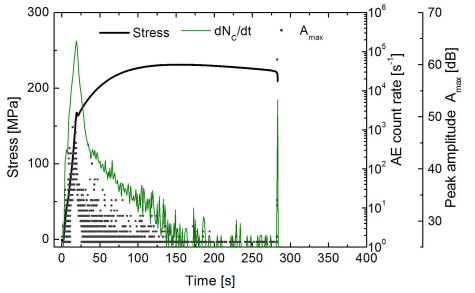

Fig. 5.3.6. Stress *vs.* time curves with the corresponding AE response (AE count rate, peak amplitudes of AE events) of tension of the rolled ZE10 TRC strip along RD (a), 45° (b), TD (c).

Microstructure and texture evolution during TD loading of the rolled ZE10 sheet

In order to provide more information about active deformation mechanisms during TD loading of the rolled ZE10 sheet, when the AE count rate exhibits two maxima close to the macroscopic YS (Fig. 5.3.5 c), additional X-ray and EBSD measurements were provided. The texture analysis was performed by ***X-ray diffraction*** from large area of the samples loaded up to specific stress levels, see Fig. 5.3.7. Those stresses were chosen with respect to the changes of the deformation curve and the AE count rate (Fig. 5.3.5c):

- 120 MPa – short after achieving YS, Fig. 5.3.7b;
- 145 MPa – after the first AE count rate maximum, Fig. 5.3.7c;
- 183 MPa – after the second AE count rate maximum, Fig. 5.3.7d;
- 215 MPa – *close to ultimate tensile strength, 15% of elongation*, Fig. 5.3.7e.

The investigated ZE10 magnesium alloy in as-rolled condition exhibits a texture with basal planes tilted away from the sheet ND toward TD, and the two peaks tilted by 45° toward TD are significant (Fig. 5.3.7a). The prismatic $(10\bar{1}0)$ pole has two peaks toward the RD.

During loading up to 120 MPa, i.e. the YS value, no significant changes in the crystallographic texture are observed comparing to the initial state (Fig. 5.3.7a-b). With increasing tensile stress up to 145 MPa (which corresponds to a state after the first AE count rate maximum), the two texture components in the (0001) pole figure towards TD disappear. The two texture components corresponding to basal planes tilted by 45° toward TD remain without significant changes with increasing loading applied.

After tension up to 183 MPa (Fig. 5.3.7d), the texture measurement shows that basal planes are tilted by 45° from ND to the sheet plane homogeneously from RD to TD. Intensity distribution of the $(10\bar{1}0)$ pole figure becomes also more homogeneous in the sheet plane from RD to TD. The texture of the sample loaded up to 215 MPa has two texture components corresponding to basal plains tilted by 45° from ND to RD and two texture components formed by grains with basal plains oriented perpendicular to RD. The higher intensity of the $(10\bar{1}0)$ pole figure is observed toward the TD.

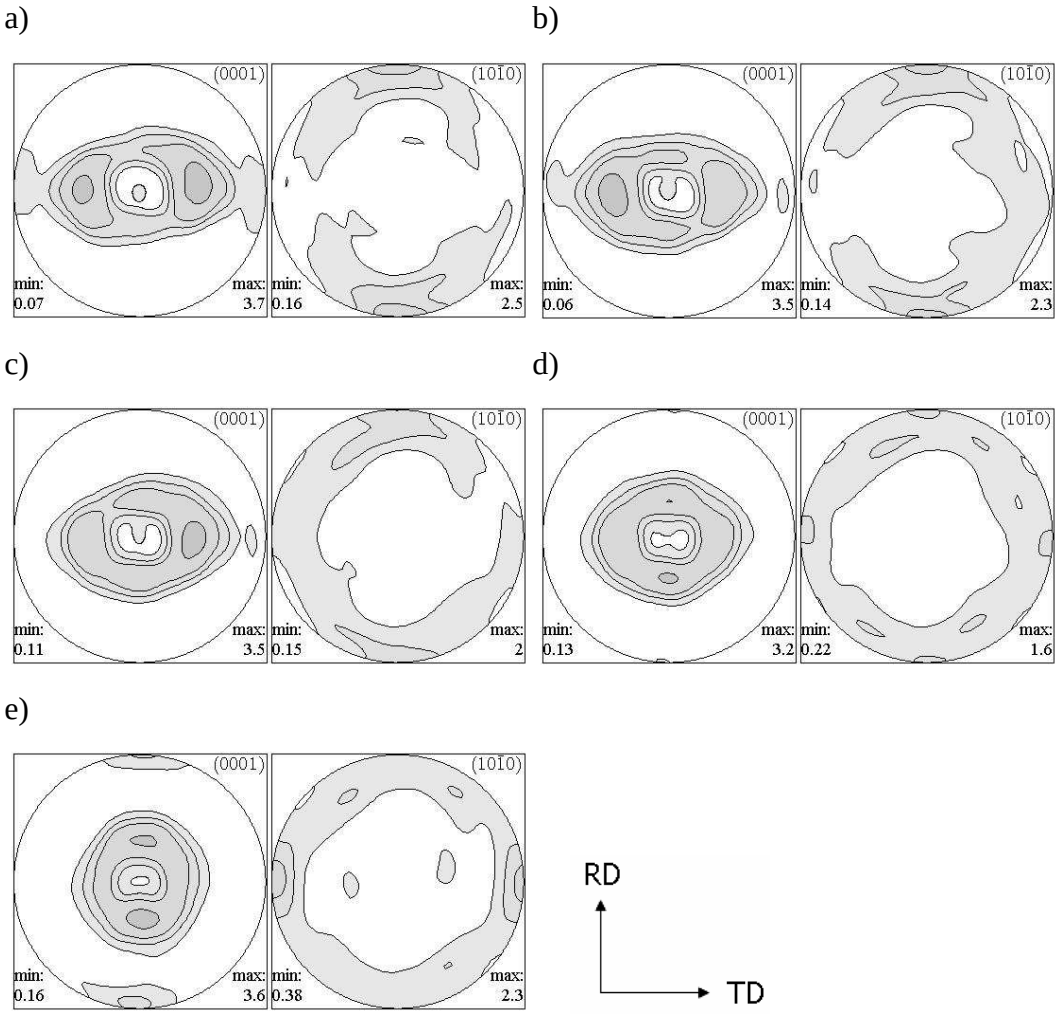

Fig. 5.3.7. The evolution of crystallographic texture evaluated form X-ray diffraction in the rolled ZE10 alloy (levels: 1.0, 1.5, 2.0, 3.0, 5.0, 7.0, 9.0 m.r.d.) in as rolled state (a) and after tension along TD up to 120 MPa (b), 145 MPa (c), 183 MPa (d), and 215 MPa (e).

To analyze the microstructure evolution in detail (especially nucleation and growth of twins), ***EBSD measurements*** on the same area of the sample in the initial state, after tension along TD up to 145 MPa and 183 MPa, were performed. These stresses were chosen according to the results of texture measurements by X-ray diffraction. The evolution of the crystallographic texture evaluated from EBSD measurements is illustrated in Fig. 5.3.8. Results are consistent with results of the X-ray studies (Figs. 5.3.7a,c,d): the basal planes are tilted away from the sheet ND toward TD in the initial state and toward RD after tensile loading along TD.

The microstructure of samples in the initial state, after tension up to 145 MPa and 183 MPa, is presented in the form of orientation map, image quality (IQ) map, and kernel average misorientation (KAM) map in Figs. 5.3.9 – 5.3.11, respectively.

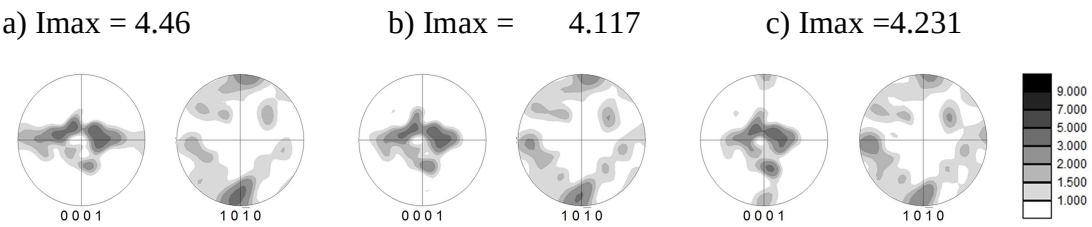

Fig. 5.3.8. The evolution of crystallographic texture evaluated from EBSD measurements in the rolled ZE10 alloy (RD↑, TD→): as rolled state (a), after tension along TD up to 145 MPa (b), and 183 MPa (c).

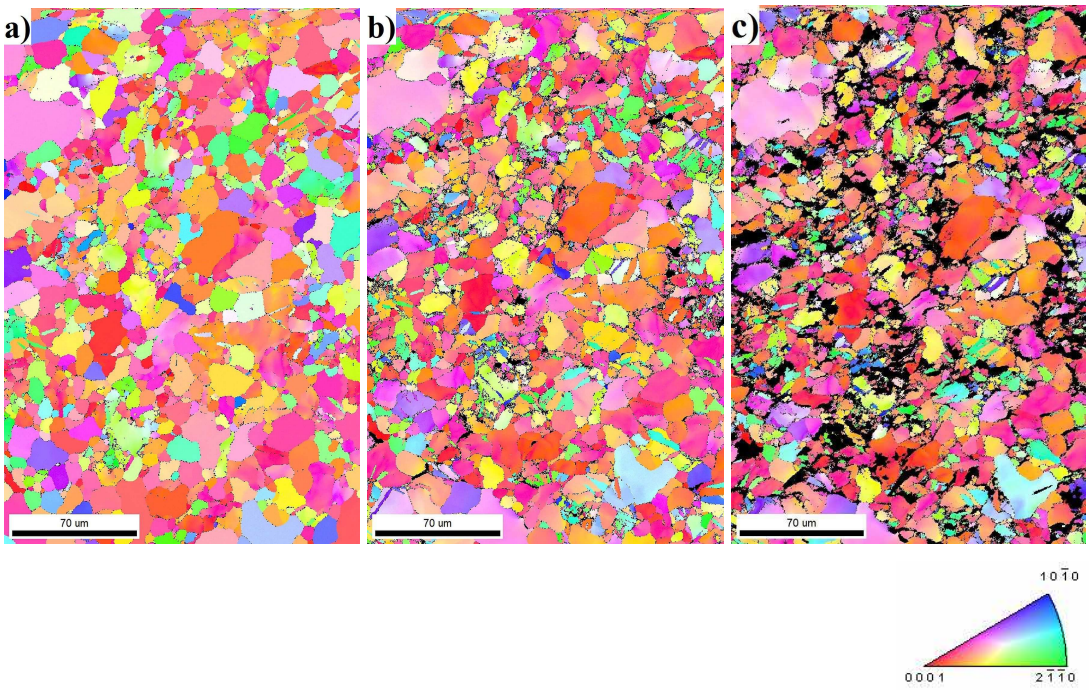

Fig. 5.3.9. Orientation map of rolled ZE10 alloy (RD↑, TD→) in as rolled state (a), after tension along the TD up to 145 MPa (b) and 183 MPa (c).

The analysis of the misorientation angle distribution of the EBSD map confirms the presence of $\{10\bar{1}2\}<10\bar{1}1>$ extension twins with a misorientation angle of 86.3° around the $<11\bar{2}0>$ axis after tension up to 120 MPa. In the image quality map, Fig. 5.3.10, boundaries of the $\{10\bar{1}2\}<10\bar{1}1>$ extension twins are marked in red. Their amount increases with increasing plastic deformation

(183 MPa). Small amount of twins in the initial state can be explained by a rolling process and mechanical polishing during sample preparation.

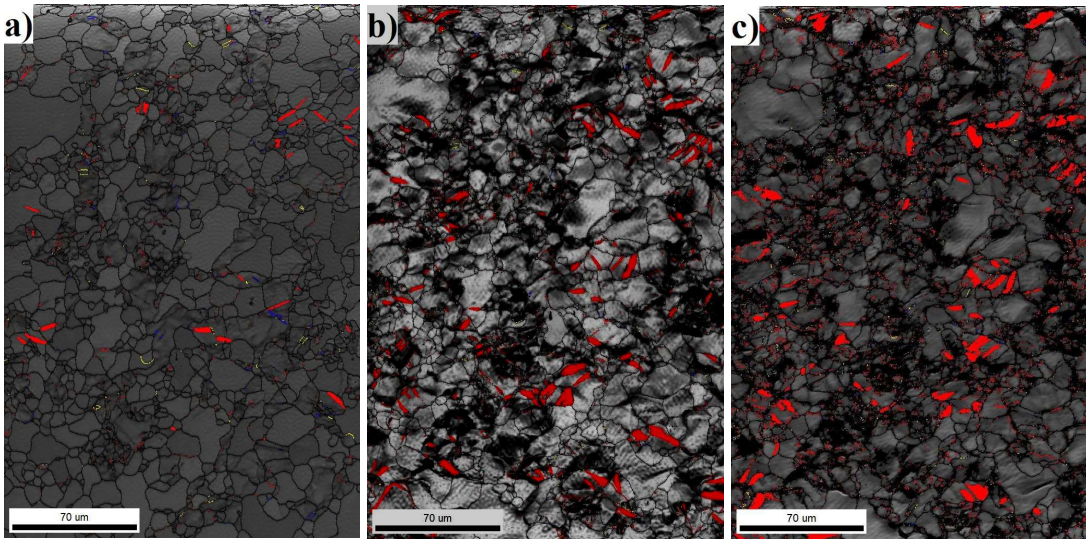

Fig. 5.3.10. Image quality map of rolled ZE10 alloy (RD↑, TD→) in as rolled state (a), after tension along the TD up to 145 MPa (b) and 183 MPa (c).

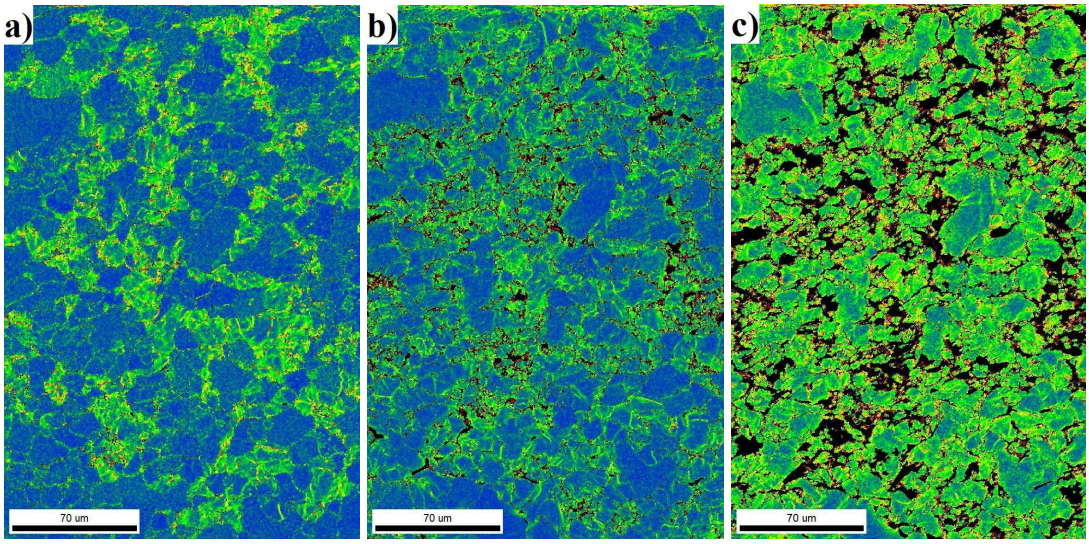

Fig. 5.3.11. Kernel Average Misorientation map of rolled ZE10 alloy (RD↑, TD→) in as rolled state (a), after tension along the TD up to 145 MPa (b) and 183 MPa (c).

The KAM analysis (Fig. 5.3.11) shows the distribution of local misorientation within individual grains and indicates an internal stress. In the initial state, the internal stress is concentrated mainly in small grains, which can be a result of the rolling process. Internal stress in small grains and along grain (and twin) boundaries increases with increasing tensile loading, Figs. 5.3.11b-c. The internal

stress in larger grains, even after loading up to 183 MPa, is significantly lower than in smaller grains and is smoothly distributed within the grain and gradually decreases from boundaries of the grains to their center.

5.3.2. Discussion: anisotropy of mechanical properties in rolled Mg alloys – effect of twinning

The significant difference in the texture of Mg alloys after applying different rolling conditions can be seen in Fig. 5.3.1. The strong texture with basal planes oriented parallel to RD is well-known feature of conventionally rolled Mg alloys, as observed in [42]. Bohlen et al. [81, 104] recently reported that the angular distribution of the basal planes in the magnesium – zinc – rare earth (RE) alloy sheets is significantly wider in TD than in RD. Therefore, the analysis of the texture development in Mg-based alloys sheets shows that RE alloying elements significantly influences the final rolling texture and consequently affects the deformation behavior and mechanical properties [45, 104-107]. Weakening of the texture due to RE alloying observed for both rolled ZE10 and rolled ZE10 TRC strip. Similar weak non-basal texture, with the angular spread of basal planes towards TD was for the rolled and annealed Mg-1Zn-0.3Ce alloy presented by Mackenzie and Pekguleryuz [43]. The different orientation of the basal pole peak for rolled ZE10 TRC strip comparing to rolled ZE10 slab is caused by the conventional rolling after the TRC process.

The difference in the texture of materials is responsible for the anisotropy of mechanical properties. It is clearly seen that the higher the angular distribution of the basal planes in the sheet plane the more pronounced anisotropy of YS is observed (Fig. 5.3.1, Table 5.3.1).

The strengthening of the AZ31 Mg alloy is higher in TD than in RD and along the axis tilted by 45^0 from RD for both rolling conditions. This behavior was also observed by Agnew and Duygulu [108] and could be explained by the influence of the initial texture of materials. The prismatic plane poles in AZ31 Mg alloys have no orientation preference in the sheet plane and therefore the difference in the orientation of the basal planes significantly influences deformation behavior. An angular spread of basal planes toward RD gives opportunity for activation of non-basal slip and/or twinning system during RD loading at lower stress [10]. During tension along TD, basal planes are oriented parallel to the loading axis. In this case,

activation of non-basal slip and twinning system requests higher stress, and therefore, work hardening is stronger. During tension along the axis tilted by 45^0 from RD, a combination of grains with basal planes oriented into ND and grains with angular spread of basal planes toward RD results in activation of non-basal slip and twinning system at stresses lower than for the TD loading and higher than for the RD loading.

The rolled ZE10 TRC strip with the angular distribution of basal planes similar to AZ31 Mg alloys exhibits a similar anisotropy consisting of a higher level of strength in TD compared to RD. For the rolled ZE10, however, an inverse anisotropy is observed: YS in RD appears to be higher than that in TD, which is caused by characteristic inverse angular spread of basal planes toward TD. The planar anisotropy of YS of the rolled ZE10 sheets was also discussed in [81]. The complex study of deformation curves, concurrent AE measurements were presented together with work hardening analysis (the Kocks-Mecking plots).

The characteristic maximum of the AE count rate, which is observed at the beginning of the plastic deformation, is usually explained by a massive dislocation multiplication, whereby various slip systems can be activated [71]. In Mg alloys, basal slip is known as the easiest activated slip system (the lowest value of CRSS in comparison with other slip systems at RT) [82] and therefore, basal slip is taken as a first activated mechanism in Mg alloys. During this process collective dislocation motion releases some amount of energy in the material, which is detected as a strong AE signal [71]. Then plastic deformation in Mg alloys proceeds by non-basal slip (e.g. prismatic <a>, pyramidal <c+a>) and twinning. The different mechanisms of the plastic deformation produce different waveforms of the AE signal, which consequently could be identified by various AE parameters. The twin nucleation is characterized by a burst type of AE signal with relatively high value of the AE maximum amplitude.

As it can be seen in Figs. 5.3.1 and 5.3.3 – 5.3.6, the difference in the AE response during tension of the sheets along various directions is associated with differences in the texture of materials. During RD loading of the rolled AZ31, which has the basal texture with wider distribution of basal planes toward RD and the high intensity of pole, the AE signal is higher. On the other hand, the rolled AZ31 TRC strip with more symmetric spread of basal pole in sheet plane, and lower intensity, exhibits lower AE activity during the same tensile loading. The difference in the AE response could be explained by various combinations of activity of prismatic <a>

and pyramidal <c+a> slip and twinning system with respect to the angular distribution of basal planes. In the work of Dobron et al. [81] it was concluded that extension twins may occur in a grain only, if the *c*-axis and the tensile axis are sufficiently close to each other. Then it could be supposed that during the RD loading the probability of twin activation in rolled AZ31 is higher than that in rolled AZ31 TRC strip. Likewise, lower AE response in rolled AZ31 during TD loading than during RD loading is explained by lower probability of twin activation (Figs.5.3.1a, 5.3.3a and c). The intermediate intensity of AE response during tension along the axis tilted by 45^0 from RD comparing to loading along other directions – the AE signal is lower than for the RD loading and higher than for the TD loading – can be explained by varying coactivity of twinning and dislocation slip caused by variations of orientation of the *c*-axis with respect to loading direction from grain to grain.

Almost no orientation preference of basal planes in sheet plane in rolled AZ31 TRC strip (Fig.5.3.1b) is responsible for similar passing of plastic deformation during loading along RD, TD, and the axis tilted by 45^0 from RD, therefore, similar AE response is seen in Fig. 5.3.4a-c.

The difference in orientation preferences of crystallographic planes in rolled ZE10 and rolled ZE10 TRC strips, as well as in AZ31, is reflected in the AE response during tension of the sheets especially along TD (Fig. 5.3.1c, d, 5.3.5c and 5.3.6c). The basal planes in rolled ZE10 are tilted by 45^0 along TD (Fig. 5.3.1c), which gives opportunity for higher **twinning activity** during TD loading comparing with RD loading. Therefore, the second maximum of the AE count rate and relatively high values of peak amplitude of events (Fig. 5.3.5 c) could be explained as a twinning activity. This suggestion is supported by the typical S-shape of the deformation curve and by the detailed study by *pseudo in-situ* X-ray and EBSD measurements.

The obtained results showed no significant changes in the crystallographic texture during loading up to 120 MPa (Fig. 5.3.7b), what can be explained by activity of dislocation slip systems and twin nucleation, which is not seen by X-ray measurement. The texture measurements after the first AE count rate maximum, i.e. after tensile loading up to 145 MPa, show disappearance of two texture components in the (0001) pole figure from the grains with basal planes into TD, what is the first sign of twinning activity. The texture changes during further loading up to 183 MPa can be explained by rotation of the original *hcp* lattice due to

$\{10\bar{1}2\}<10\bar{1}1>$ extension twinning by 86°. During loading from 183 MPa to 215 MPa, Fig. 5.3.7d to e, the texture changes result from the massive twin growth. In other words, during tensile loading along TD the basal planes moved from TD towards RD (Fig. 5.3.7). Analysis of EBSD maps (orientation, KAM, IQ maps) shows microstructure development of the investigated sheet during TD loading. The twin nucleation is significant after the first AE count rate maximum. The initial concentration of stress results in increase of the internal stress in small grains as well as along grain (and twin) boundaries during tensile loading. In the micro-structure measured after the second AE count rate, a massive twin growth is observed. The nucleation of new twins is naturally possible till the end of the test.

The subsequent rapid decrease of the AE count rate after YS during RD loading of rolled ZE10 is associated with the activation of non-basal slip systems and increasing number of sessile dislocations. Sessile dislocations reduce the free path of moving dislocations consequently. This suggestion correlates with stronger hardening for rolled ZE10 comparing with rolled ZE10 TRC, see Fig. 5.3.5a and 5.3.6a.

Key points of Chapter 5

1. Active deformation mechanisms in Mg single crystals were correlated to their AE response:

- dominant activity of basal <a> slip during uniaxial compression along the $<11\bar{2}2>$ axis results in low-amplitude AE signal;
- pyramidal π2 slip during both uniaxial and channel-die compression along the *c*-axis results in a very weak AE signal, which is consistent with a rapid immobilization of dislocations caused by the formation of strong obstacles;
- extension $\{10\bar{1}2\}<10\bar{1}1>$ twins and prismatic slip are dominant during compression along the $<10\bar{1}0>$ and $<11\bar{2}0>$ axis. Twinning results in burst type of AE even with high amplitude;
- twinning activity is higher during uniaxial compression along the $<11\bar{2}0>$ axis in comparison with the $<10\bar{1}0>$ axis and it is represented by a more pronounced AE response;
- constraining of the $(11\bar{2}0)$ planes restricts the growth of extension twins and extension along the *c*-axis is accommodated mainly by increasing number of nucleated twins rather than by their growth;
- the four variants of extension twins with *m* of 0.35 have higher influence on plastic deformation during channel-die test than the two variants with higher *m* of 0.5.

2. Twinning – detwinning mechanism was investigated during cyclic loading of extruded AZ31 and ZE10 alloys:

- ✓ higher compressive pre-loading leads to more pronounced S-shape of deformation curve;
- ✓ the differences in the homogeneity and the grain size distribution indicate that twin nucleation is grain size dependent: small grains contain a smaller number or no twins, whereas multiple twins nucleate in larger grains (results of AZ31);
- ✓ the AE signal has higher amplitudes of events in ZE10 than in AZ31. Higher dislocation mobility is a result of higher mean free path of

dislocation motion due to a lower concentration of obstacles such as grain boundaries;

- ✓ detwinning during reverse loading is a significant deformation mechanism and is preferred at the expense of nucleation and growth of new twins;
- ✓ twinning and detwinning, in terms of boundary mobility, are not grain size dependent;
- ✓ the AE response during twin growth and detwinning, shows events with lower amplitudes than during twin nucleation;
- ✓ new compression and extension twins appear after completing the detwinning process at a later stage of plastic deformation in both AZ31 and ZE10 alloys;
- ✓ newly created twins during subsequent tension contribute to strain accommodation in relation to the orientation of the parent grains: another type of extension twins nucleates compared with those that are active during pre-compression.

3. Anisotropy of mechanical properties in rolled AZ31 and ZE10 alloys:

- ➢ both rolled AZ31 Mg alloys exhibit a typically basal texture, whereas two different types of texture with respect to rolling conditions were observed for ZE10 alloy;
- ➢ anisotropy of mechanical properties is connected with the texture asymmetry around the ND formed during rolling process and results in AE response: least pronounced anisotropy of the YS leads to similar AE response.
- ➢ the higher the angular distribution of the basal planes toward loading axis, the higher AE response is observed.
- ➢ activity of extension $\{10\bar{1}2\}<10\bar{1}1>$ twins during loading along the TD of conventionally rolled ZE10 sheet results in double maximum of the AE count rate near the macroscopic yield strength. Results are supported by X-ray and EBSD measurements.

Chapter 6

Conclusions and perspectives

6.1. General comments

The AE signatures for specific deformation mechanisms were obtained from uniaxial and channel-die compression tests of ***Mg single crystals*** with different orientation. Following conclusions can be drawn:

- Dominant activity of basal <a> slip during loading along the $<11\bar{2}2>$ axis is characterized by a low amplitude AE signal.
- Pyramidal $\pi 2$ slip systems were activated during uniaxial and channel-die compression along the *c*-axis. The very low AE activity during the whole test is caused by a rapid immobilization of dislocations due to the creation of strong obstacles.
- The higher twinning activity, represented by a more pronounced AE response, was observed during uniaxial and channel-die compression along the $<11\bar{2}0>$ axis in comparison with the $<10\bar{1}0>$ axis. Constraining of specific planes during channel-die compression led to higher amount of twins. It is reflected in higher AE activity in comparison with the uniaxial compression. Moreover, constraining of the $(11\bar{2}0)$ planes restricts the growth of extension twins and extension along the *c*-axis is accommodated mainly by increasing number of nucleated twins rather than by their growth.

The obtained results were used for further investigations of active deformation mechanisms in wrought Mg alloys with a strong texture. General approach that

the plastic deformation in polycrystalline wrought Mg alloys with a strong texture is controlled by the same mechanisms as in single crystals was adopted. Thus the results for Mg single crystals were used for the interpretation of the AE response during deformation of extruded and rolled Mg alloys.

Moreover, the twinning-detwinning process was investigated in detail with respect to the initial microstructure of Mg ***extrusions*** during one-cyclic test. The transition between different deformation mechanisms, such as dislocation slip, twin nucleation, twin growth and detwinning, at different stages of the deformation test were revealed using a combination of AE and EBSD methods. The investigation of extruded profiles showed that the AE signal in the case of ZE10 has higher amplitudes of events compared to those for AZ31. The differences in the homogeneity and the grain size distribution indicate that the twin nucleation is grain-size dependent. It was shown that particularly small grains in the case of AZ31 contain a smaller number or no twins, whereas multiple extension $\{10\bar{1}2\}<10\bar{1}1>$ twins nucleate in larger grains during compression in extrusion direction.

Detwinning is a significant deformation mechanism during reverse loading and is preferred at the expense of nucleation and growth of new twins. Detwinning has a similar influence on the deformation behavior to twinning (characteristic S-shape of the deformation curve). It was also found that twinning and detwinning, in terms of boundary mobility, are not grain size dependent.

During the twin growth and detwinning, the AE response shows events with lower amplitudes than during twin nucleation. Therefore, neither thickening nor thinning of twins obviously contributes to the AE response. In this part of the deformation test, dislocation slip dominates in the AE response. An increase in the free length of moving dislocations during twin thinning leads to an increase in potential dislocation movement; therefore, an increase in the AE response during reverse loading is observed.

In both AZ31 and ZE10 alloys, new compression and extension twins appear after completing the detwinning process at a later stage of plastic deformation. Newly created twins contribute to strain accommodation in relation to the orientation of the parent grains. Particularly, another type of extension twins nucleates during reverse loading compared with those that are active during pre-compression.

It was shown that the grain size and homogeneity of the microstructure have influence of dislocation and twin activity reflecting in AE response. Particularly, a stronger AE signal for ZE10 compared with AZ31 during the entire test can be explained by the higher mean free path of dislocation motion due to a lower concentration of obstacles such as grain boundaries.

The deformation behavior of ***rolled Mg alloys*** with respect to initial texture was studied during tensile tests with concurrent AE measurements. Rolling conditions result in two different types of texture for Mg-Zn-rare earth alloy sheets, while for both rolled AZ31 Mg alloys a typically basal texture was observed. From AE measurements it was concluded that deformation during the loading along TD of conventionally rolled sheet ZE10 is realized by basal slip and deformation twinning. Massive twin nucleation contributes to the double maximum of the AE count rate near the macroscopic yield strength. Twinning activity was confirmed by *pseudo in-situ* X-ray and EBSD measurements.

Generally, anisotropy of mechanical properties may be easily connected with the texture asymmetry around the ND, which is formed during rolling process. The effect of the rolling conditions on the texture of materials is well seen in the AE response during tensile loading of both Mg alloys. Rolled AZ31 TRC strip exhibits similar AE response during TD and RD loading due to the least pronounced anisotropy of YS. Rolled ZE10 has a characteristic difference in AE response with respect to orientation of crystallographic planes. The higher the angular distribution of the basal planes toward loading axis, the higher AE response is observed.

6.2. Future prospect

Acquired knowledge about deformation mechanisms in wrought Mg alloys may contribute to design novel Mg alloys with specific mechanical properties for specific applications.

The investigation of twinning and twinning – detwinning processes may be useful for development of crystal plasticity-based model of deformation behavior of textured hexagonal alloys. With increasing loading cycles, twin-twin junctions can form, and they have been shown to play a crucial role in increasing strain hardening and controlling microstructure evolution. Therefore, understanding of twinning and

twinning –detwinning mechanisms during repeated loading for several cycles and strain path changes is essential.

Nowadays, a large number of studies have been conducted to understand the interaction between solute atoms and the motion of dislocation at the atomic level [109, 110]. In addition, the pinning effect of solute atoms on twin boundaries has recently attracted considerable attention [39, 40]. However, it is not clear how solute atoms interact with twin boundaries and affect their mobility (propagation). A comprehensive understanding of nucleation and growth of twins and twin-twin interactions on atomic scale in combination with pinning strength of twin boundaries is needed. In another words, such study can help to reveal the influence of solute atoms on twin propagation, and therefore on mechanical properties of hexagonal materials. All can contribute to designing materials with requested properties.

Another important direction of investigation of twinning in hcp materials could be the characterization of three-dimensional shapes of twins. This approach is possible using such advanced electron microscopy techniques as 3D EBSD performed using Focusing ion beam system. It can help to understand propagation of twins as a function of grain orientation with regards to a loading axis or internal stress distribution.

As to the AE technique, it proved useful as an advanced *in-situ* experimental method. This technique has potential for wide applicability in studies of deformation mechanisms in diverse metallic materials.

Bibliography

[1] E. Schmid, G. Wassermann. Über die Textur gezogener Magnesium- und Zinkdrähte, Naturwissenschaften 17 (1929) 312-314.

[2] S. Ando, H. Tonda. Non-basal slips in magnesium and magnesium-lithium alloy single crystals, Mater Sci Forum 350 (2000) 43-48.

[3] A. Staroselsky, L. Anand. A constitutive model for hcp materials deforming by slip and twinning: Application to magnesium alloy AZ31B, Int J Plasticity 19 (2003) 1843-1864.

[4] P. Kratochvíl, P. Lukáč, B. Sprušil. Úvod do fyziky kovů I, SNTL, Praha, 1984.

[5] M. Peach, J.S. Koehler. The Forces Exerted on Dislocations and the Stress Fields Produced by Them, Phys Rev 80 (1950) 436-439.

[6] J.P. Hirth, J. Lothe. Theory of dislocations, McGraw-Hill, New York, 1967.

[7] J. Čapek, K. Máthis, B. Clausen, J. Stráská, P. Beran, P. Lukáš. Study of the loading mode dependence of the twinning in random textured cast magnesium by acoustic emission and neutron diffraction methods, Mat Sci Eng a-Struct 602 (2014) 25-32.

[8] G.S. Kim. Small Volume Investigation of Slip and Twinning in Magnesium Single Crystals. vol. Ph.D.: Universite de Grenoble, Grenoble, 2011. p.132.

[9] B.C. Wonsiewicz, W.A. Backofen. Plasticity of magnesium crystals, Trans AIME 239 (1967) 1422-1431.

[10] P.W. Bakarian, C.H. Mathewson. Slip and twinning of magnesium single crystals at elevated temperatures, Trans AIME 152 (1943) 226-254.

[11] A. Chapuis, J.H. Driver. Temperature dependency of slip and twinning in plane strain compressed magnesium single crystals, Acta Mater 59 (2011) 1986-1994.

[12] S. Kleiner, P.J. Uggowitzer. Mechanical anisotropy of extruded Mg-6% Al-1% Zn alloy, Mat Sci Eng a-Struct 379 (2004) 258-263.

[13] P. Dobroň, J. Bohlen, F. Chmelík, P. Lukáč, D. Letzig, K.U. Kainer. Mechanical anisotropy of AZ31 magnesium alloy sheet investigated by the acoustic emission technique, Kovove Mater 45 (2007) 129-133.

[14] M.R. Barnett, M.D. Nave, C.J. Bettles. Deformation microstructures and textures of some cold rolled Mg alloys, Mat Sci Eng a-Struct 386 (2004) 205-211.

[15] M.H. Yoo. Slip, twinning, and fracture in hexagonal close-packed metals, Metall Trans A 12 (1981) 409-418.

[16] R. von Mises. Mechanik der plastischen Formänderung von Kristallen, Z Angew Math Mech 8 (1928) 161-185.

[17] J.W. Christian, S. Mahajan. Deformation twinning, Prog Mater Sci 39 (1995) 1-157.

[18] J. Wang, I.J. Beyerlein, C.N. Tomé. An atomic and probabilistic perspective on twin nucleation in Mg, Scripta Mater 63 (2010) 741-746.

[19] C.N. Tomé, I.J. Beyerlein, J. Wang, R.J. McCabe. A multi-scale statistical study of twinning in magnesium, JOM-J Min Met Mat S 63 (2011) 19-23.

[20] D. Sarker, D.L. Chen. Dependence of compressive deformation on pre-strain and loading direction in an extruded magnesium alloy: Texture, twinning and de-twinning, Mat Sci Eng a-Struct 596 (2014) 134-144.

[21] Y. Xin, X. Zhou, L. Lv, Q. Liu. The influence of a secondary twin on the detwinning deformation of a primary twin in Mg–3Al–1Zn alloy, Mat Sci Eng a-Struct 606 (2014) 81-91.

[22] Q. Yu, J. Wang, Y. Jiang, R.J. McCabe, N. Li, C.N. Tomé. Twin–twin interactions in magnesium, Acta Mater 77 (2014) 28-42.

[23] X.Y. Lou, M. Li, R.K. Boger, S.R. Agnew, R.H. Wagoner. Hardening evolution of AZ31B Mg sheet, Int J Plasticity 23 (2007) 44-86.

[24] L. Wang, G. Huang, Q. Quan, P. Bassani, E. Mostaed, M. Vedani, F. Pan. The effect of twinning and detwinning on the mechanical property of AZ31 extruded magnesium alloy during strain-path changes, Mater Design 63 (2014) 177-184.

[25] H. Wang, P.D. Wu, J. Wang, C.N. Tomé. A crystal plasticity model for hexagonal close packed (HCP) crystals including twinning and de-twinning mechanisms, Int J Plasticity 49 (2013) 36-52.

[26] D.W. Brown, S.R. Agnew, M.A.M. Bourke, T.M. Holden, S.C. Vogel, C.N. Tome. Internal strain and texture evolution during deformation twinning in magnesium, Mat Sci Eng a-Struct 399 (2005) 1-12.

[27] M.R. Barnett. Twinning and the ductility of magnesium alloys Part I: "Tension" twins, Mat Sci Eng a-Struct 464 (2007) 1-7.

[28] P.G. Partridge. The crystallography and deformation modes of hexagonal close-packed metals, Metall Rev 12 (1967) 169-194.

[29] E.W. Kelley, W.F. Hosford. Plane-strain compression of magnesium and magnesium alloy crystals, Trans AIME 242 (1968) 5-13.

[30] W. Wu, H. Qiao, K. An, X. Guo, P. Wu, P.K. Liaw. Investigation of deformation dynamics in a wrought magnesium alloy, Int J Plasticity 62 (2014) 105-120.

[31] Y.N. Wang, J.C. Huang. The role of twinning and untwinning in yielding behavior in hot-extruded Mg-Al-Zn alloy, Acta Mater 55 (2007) 897-905.

[32] A. Chapuis, Y.C. Xin, X.J. Zhou, Q. Liu. {10-12} Twin variants selection mechanisms during twinning, re-twinning and detwinning, Mat Sci Eng a-Struct 612 (2014) 431-439.

[33] D. Sarker, D.L. Chen. Detwinning and strain hardening of an extruded magnesium alloy during compression, Scripta Mater 67 (2012) 165-168.

[34] M.R. Barnett. Twinning and the ductility of magnesium alloys Part II. "Contraction" twins, Mat Sci Eng a-Struct 464 (2007) 8-16.

[35] E.W. Kelley, W.F. Hosford. The deformation characteristics of textured magnesium, Trans AIME 242 (1968) 654 - 661.

[36] E.O. Hall. The Deformation and Ageing of Mild Steel: III Discussion of Results, Proceedings of the Physical Society. Section B 64 (1951) 747-753.

[37] N.J. Petch. The cleavage strength of polycrystals, J Iron Steel Inst 174 (1953) 25-28.

[38] R.W. Armstrong. 60 Years of Hall-Petch: Past to Present Nano-Scale Connections, Mater Trans 55 (2014) 2-12.

[39] J.F. Nie, Y.M. Zhu, J.Z. Liu, X.Y. Fang. Periodic Segregation of Solute Atoms in Fully Coherent Twin Boundaries, Science 340 (2013) 957-960.

[40] A. Kumar, J. Wang, C.N. Tomé. First-principles study of energy and atomic solubility of twinning-associated boundaries in hexagonal metals, Acta Mater 85 (2015) 144-154.

[41] W.F. Hosford, R.M. Caddell. Metal Forming: Mechanics and Metallurgy, 2nd ed., Prentice-Hall PTR, 1993.

[42] Magnesium Alloys and Technologies, K. U. Kainer (ed.), Wiley-VCH, Weinheim, Cambridge, 2003.

[43] L.W.F. Mackenzie, M.O. Pekguleryuz. The recrystallization and texture of magnesium-zinc-cerium alloys, Scripta Mater 59 (2008) 665-668.

[44] S. Yi, J. Bohlen, F. Heinemann, D. Letzig. Mechanical anisotropy and deep drawing behaviour of AZ31 and ZE10 magnesium alloy sheets, Acta Mater 58 (2010) 592-605.

[45] K. Hantzsche, J. Bohlen, J. Wendt, K.U. Kainer, S.B. Yi, D. Letzig. Effect of rare earth additions on microstructure and texture development of magnesium alloy sheets, Scripta Mater 63 (2010) 725-730.

[46] J. Bohlen, F. Chmelik, P. Dobron, F. Kaiser, D. Letzig, P. Lukac, K.U. Kainer. Orientation effects on acoustic emission during tensile deformation of hot rolled magnesium alloy AZ31, J Alloy Compd 378 (2004) 207-213.

[47] T. Wu, L. Jin, W.X. Wu, L. Gao, J. Wang, Z.Y. Zhang, J. Dong. Improved ductility of Mg-Zn-Ce alloy by hot pack-rolling, Mat Sci Eng a-Struct 584 (2013) 97-102.

[48] J. Sun, L. Jin, S. Dong, Z. Zhang, J. Dong. Asymmetry strain hardening behavior in Mg-3%Al-1%Zn and Mg-8%Gd-3%Y alloy tubes, Mater Lett 107 (2013) 197-201.

[49] H. Kang, D.H. Bae. Deformation behavior of a statically recrystallized Mg-Zn-MM alloy sheet, Mat Sci Eng a-Struct 582 (2013) 203-210.

[50] F.A. Mirza, D.L. Chen, D.J. Li, X.Q. Zeng. Effect of rare earth elements on deformation behavior of an extruded Mg-10Gd-3Y-0.5Zr alloy during compression, Mater Design 46 (2013) 411-418.

[51] B.H. Lee, S.H. Park, S.-G. Hong, K.-T. Park, C.S. Lee. Role of initial texture on the plastic anisotropy of Mg–3Al–1Zn alloy at various temperatures, Mat Sci Eng a-Struct 528 (2011) 1162-1172.

[52] F.A. Mirza, D.L. Chen. Fatigue of rare-earth containing magnesium alloys: A review, Fatigue Fract Eng M 37 (2014) 831-853.

[53] S. Begum, D.L. Chen, S. Xu, A.A. Luo. Low cycle fatigue properties of an extruded AZ31 magnesium alloy, Int J Fatigue 31 (2009) 726-735.

[54] J. Koike, N. Fujiyama, D. Ando, Y. Sutou. Roles of deformation twinning and dislocation slip in the fatigue failure mechanism of AZ31 Mg alloys, Scripta Mater 63 (2010) 747-750.

[55] J. Bohlen, P. Dobron, L. Nascimento, K. Parfenenko, F. Chmelik, D. Letzig. The Effect of Reversed Loading Conditions on the Mechanical Behaviour of Extruded Magnesium Alloy AZ31, Acta Phys Pol A 122 (2012) 444-449.

[56] G. Proust, C.N. Tomé, A. Jain, S.R. Agnew. Modeling the effect of twinning and detwinning during strain-path changes of magnesium alloy AZ31, Int J Plasticity 25 (2009) 861-880.

[57] C.H. Cáceres, T. Sumitomo, M. Veidt. Pseudoelastic behaviour of cast magnesium AZ91 alloy under cyclic loading-unloading, Acta Mater 51 (2003) 6211-6218.

[58] S.H. Park, S.-G. Hong, J.H. Lee, C.S. Lee. Multiple twinning modes in rolled Mg–3Al–1Zn alloy and their selection mechanism, Mat Sci Eng a-Struct 532 (2012) 401-406.

[59] R.A. Lebensohn, C.N. Tomé. A self-consistent anisotropic approach for the simulation of plastic deformation and texture development of polycrystals: Application to zirconium alloys, Acta Metall Mater 41 (1993) 2611-2624.

[60] C.N. Tomé, P.J. Maudlin, R.A. Lebensohn, G.C. Kaschner. Mechanical response of zirconium—I. Derivation of a polycrystal constitutive law and finite element analysis, Acta Mater 49 (2001) 3085-3096.

[61] G.C. Kaschner, J.F. Bingert, C. Liu, M.L. Lovato, P.J. Maudlin, M.G. Stout, C.N. Tomé. Mechanical response of zirconium—II. Experimental and finite element analysis of bent beams, Acta Mater 49 (2001) 3097-3108.

[62] I.J. Beyerlein, C.N. Tomé. A dislocation-based constitutive law for pure Zr including temperature effects, Int J Plasticity 24 (2008) 867-895.

[63] A. Molinari, G.R. Canova, S. Ahzi. A self consistent approach of the large deformation polycrystal viscoplasticity, Acta Metall Mater 35 (1987) 2983-2994.

[64] S. Graff, W. Brocks, D. Steglich. Yielding of magnesium: From single crystal to polycrystalline aggregates, Int J Plasticity 23 (2007) 1957-1978.

[65] F. Hiura, M. Niewczas. Latent hardening effect under self- and coplanar dislocation interactions in Mg single crystals, Scripta Mater 106 (2015) 17-20.

[66] B. Sułkowski. Analysis of crystallographic orientation changes during deformation of magnesium single crystals, Acta Phys Pol A 126 (2014) 768-771.

[67] B. Selvarajou, J.H. Shin, T.K. Ha, I.S. Choi, S.P. Joshi, H.N. Han. Orientation-dependent indentation response of magnesium single crystals: Modeling and experiments, Acta Mater 81 (2014) 358-376.

[68] D. Catoor, Y.F. Gao, J. Geng, M.J.N.V. Prasad, E.G. Herbert, K.S. Kumar, G.M. Pharr, E.P. George. Incipient plasticity and deformation mechanisms in single-crystal Mg during spherical nanoindentation, Acta Mater 61 (2013) 2953-2965.

[69] H. Kitahara, T. Mayama, K. Okumura, Y. Tadano, M. Tsushida, S. Ando. Anisotropic deformation induced by spherical indentation of pure Mg single crystals, Acta Mater 78 (2014) 290-300.

[70] K.D. Molodov, T. Al-Samman, D.A. Molodov, G. Gottstein. Mechanisms of exceptional ductility of magnesium single crystal during deformation at room temperature: Multiple twinning and dynamic recrystallization, Acta Mater 76 (2014) 314-330.

[71] C.R. Heiple, S.H. Carpenter. Acoustic emission produced by deformation of metals and alloys - A review: Part I, J Acoustic Emission 6 (1987) 177-204.

[72] Standard Practice for Acoustic Emission Examination of Fiberglass Reinforced Plastic Resin (FRP) Tanks/vessels (2011).

[73] I. Shashkov. Multiscale study of the intermittency of plastic deformation by acoustic emission method. vol. Ph.D.: Université de Lorraine, Metz, 2012. p.162.

[74] O. Muransky, M.R. Barnett, D.G. Carr, S.C. Vogel, E.C. Oliver. Investigation of deformation twinning in a fine-grained and coarse-grained ZM20 Mg alloy: Combined in situ neutron diffraction and acoustic emission, Acta Mater 58 (2010) 1503-1517.

[75] F. Chmelík, E. Pink, J. Król, J. Balík, J. Pešička, P. Lukáč. Mechanisms of serrated flow in aluminium alloys with precipitates investigated by acoustic emission, Acta Mater 46 (1998) 4435-4442.

[76] D.R. James, S.H. Carpenter. The effect of sample size on the acoustic emission generated during tensile deformation of 7075 aluminum alloy, Scripta Metall Mater 10 (1976) 779-781.

[77] M. Lugo, J.B. Jordon, M.F. Horstemeyer, M.A. Tschopp, J. Harris, A.M. Gokhale. Quantification of damage evolution in a 7075 aluminum alloy using an acoustic emission technique, Mat Sci Eng a-Struct 528 (2011) 6708-6714.

[78] Zs. Kovács, F. Chmelik, J. Lendvai, P. Lukáč. Acoustic emission due to Portevin-Le Châtelier instabilities in load rate controlled experiments, Kovove Mater 40 (2002) 298-306.

[79] E. Meza-Garcia, P. Dobron, J. Bohlen, D. Letzig, F. Chmelik, P. Lukac, K.U. Kainer. Deformation mechanisms in an AZ31 cast magnesium alloy as investigated by the acoustic emission technique, Mat Sci Eng a-Struct 462 (2007) 297-301.

[80] J. Capek, K. Mathis, B. Clausen, J. Straska, P. Beran, P. Lukas. Study of the loading mode dependence of the twinning in random textured cast magnesium by acoustic emission and neutron diffraction methods, Mat Sci Eng a-Struct 602 (2014) 25-32.

[81] P. Dobron, J. Balik, F. Chmelik, K. Illkova, J. Bohlen, D. Letzig, P. Lukac. A study of mechanical anisotropy of Mg-Zn-Rare earth alloy sheet, J Alloy Compd 588 (2014) 628-632.

[82] T. Richeton, P. Dobron, F. Chmelik, J. Weiss, F. Louchet. On the critical character of plasticity in metallic single crystals, Mat Sci Eng a-Struct 424 (2006) 190-195.

[83] C.R. Heiple, S.H. Carpenter. Acoustic emission produced by deformation of metals and alloys - A review: Part II, J Acoustic Emission 6 (1987) 215-237.

[84] R.M. Fisher, J.S. Lally. Microplasticity detected by an acoustic technique, Can J Phys 45 (1967) 1147-1159.

[85] http://www.substech.com/.

[86] F. Bachmann, R. Hielscher, H. Schaeben Texture Analysis with MTEX – Free and Open Source Software Toolbox, Solid State Phenom 160 (2010) 63-68.

[87] H.L. Kim, J.S. Park, Y.W. Chang. Effects of lattice parameter changes on critical resolved shear stress and mechanical properties of magnesium binary single crystals, Mat Sci Eng a-Struct 540 (2012) 198-206.

[88] T. Obara, H. Yoshinga, S. Morozumi. $\{11\bar{2}2\}\langle 1123\rangle$ Slip system in magnesium, Acta Metall Mater 21 (1973) 845-853.

[89] J.F. Stohr, J.P. Poirier. Electronic microscopy study of $\{11\bar{2}2\}\langle 1\bar{1}23\rangle$ pyramidal slip in magnesium, Philos Mag 25 (1972) 1313-1329.

[90] U.F. Kocks, D.G. Westlake. The importance of twinning for the ductility of CPH polycrystals, Trans Metall Soc AIME 239 (1967) 1107-1109.

[91] J.P. Toronchuk. Acoustic emission during twinning of Zinc single crystals, Mater Eval 35 (1977) 51-53.

[92] P. Dobron, J. Bohlen, F. Chmelik, P. Lukac, D. Letzig, K.U. Kainer. Acoustic emission during stress relaxation of pure magnesium and AZ magnesium alloys, Mat Sci Eng a-Struct 462 (2007) 307-310.

[93] K. Mathis, G. Csiszar, J. Capek, J. Gubicza, B. Clausen, P. Lukas, A. Vinogradov, S.R. Agnew. Effect of the loading mode on the evolution of the deformation mechanisms in randomly textured magnesium polycrystals - Comparison of experimental and modeling results, Int J Plasticity 72 (2015) 127-150.

[94] A. Ghaderi, M.R. Barnett. Sensitivity of deformation twinning to grain size in titanium and magnesium, Acta Mater 59 (2011) 7824-7839.

[95] K. Hazeli, J. Cuadra, P.A. Vanniamparambil, A. Kontsos. In situ identification of twin-related bands near yielding in a magnesium alloy, Scripta Mater 68 (2013) 83-86.

[96] K. Mathis, F. Chmelik, M. Janecek, B. Hadzima, Z. Trojanova, P. Lukac. Investigating deformation processes in AM60 magnesium alloy using the acoustic emission technique, Acta Mater 54 (2006) 5361-5366.

[97] J. Balik, P. Lukac, Z. Drozd, R. Kuzel. Strain-hardening behaviour of AZ31 magnesium alloys, Int J Mater Res 100 (2009) 322-325.

[98] J. Balik, P. Dobron, F. Chmelik, R. Kuzel, D. Drozdenko, J. Bohlen, D. Letzig, P. Lukac. Modeling of the work hardening in magnesium alloy sheets, Int J Plasticity 76 (2016) 166-185.

[99] K. Illkova, P. Dobron, F. Chmelik, K.U. Kainer, J. Balik, S. Yi, D. Letzig, J. Bohlen. Effect of aluminium and calcium on the microstructure, texture, plastic deformation and related acoustic emission of extruded magnesium-manganese alloys, J Alloy Compd 617 (2014) 253-264.

[100] J. Bohlen, P. Dobron, E.M. Garcia, F. Chmelik, P. Lukac, D. Letzig, K.U. Kainer. The effect of grain size on the deformation behaviour of magnesium alloys investigated by the acoustic emission technique, Adv Eng Mater 8 (2006) 422-427.

[101] Z.Z. Shi, Y.D. Zhang, F. Wagner, P.A. Juan, S. Berbenni, L. Capolungo, J.S. Lecomte, T. Richeton. On the selection of extension twin variants with low Schmid factors in a deformed Mg alloy, Acta Mater 83 (2015) 17-28.

[102] H. El Kadiri, J. Kapil, A.L. Oppedal, L.G. Hector Jr, S.R. Agnew, M. Cherkaoui, S.C. Vogel. The effect of twin–twin interactions on the nucleation and propagation of twinning in magnesium, Acta Mater 61 (2013) 3549-3563.

[103] R.E. Reed-Hill, R. Abbaschian. Physical metallurgy principles. 3rd ed., PWS-Kent Pub., Boston, 1992.

[104] J. Bohlen, M.R. Nürnberg, J.W. Senn, D. Letzig, S.R. Agnew. The texture and anisotropy of magnesium–zinc–rare earth alloy sheets, Acta Mater 55 (2007) 2101-2112.

[105] C. Xu, S.W. Xu, M.Y. Zheng, K. Wu, E.D. Wang, S. Kamado, G.J. Wang, X.Y. Lv. Microstructures and mechanical properties of high-strength Mg-Gd-Y-Zn-Zr alloy sheets processed by severe hot rolling, J Alloy Compd 524 (2012) 46-52.

[106] T. Itoi, T. Inazawa, M. Yamasaki, Y. Kawamura, M. Hirohashi. Microstructure and mechanical properties of Mg-Zn-Y alloy sheet prepared by hot-rolling, Mat Sci Eng a-Struct 560 (2013) 216-223.

[107] C.J. Bettles, M.A. Gibson. Current wrought magnesium alloys: Strengths and weaknesses, JOM-J Min Met Mat S 57 (2005) 46-49.

[108] S.R. Agnew, O. Duygulu. Plastic anisotropy and the role of non-basal slip in magnesium alloy AZ31B, Int J Plasticity 21 (2005) 1161-1193.

[109] J.A. Yasi, L.G. Hector Jr, D.R. Trinkle. First-principles data for solid-solution strengthening of magnesium: From geometry and chemistry to properties, Acta Mater 58 (2010) 5704-5713.

[110] G.P.M. Leyson, L.G. Hector Jr, W.A. Curtin. First-principles prediction of yield stress for basal slip in Mg–Al alloys, Acta Mater 60 (2012) 5197-5203.